The role of sand in Wave-Supported Gravity Flows over primarily muddy seabeds

Zhuochen Han

A dissertation
submitted in partial fulfillment of the
requirements for the degree of

Doctor of Philosophy

University of Washington

2021

Reading Committee:

Alexander R. Horner-Devine, Chair

Andrea S. Ogston

Tian-Jian Hsu

C. Chris Chickadel

Program Authorized to Offer Degree:
Civil and Environmental Engineering

University of Washington

Abstract

The role of sand in Wave-Supported Gravity Flows over primarily muddy seabeds

Zhuochen Han

Chair of the Supervisory Committee:
Professor Alexander R. Horner-Devine
Civil and Environmental Engineering

Wave-supported gravity flows (WSGF) are one of the most crucial processes contributing to sediment transport across continental shelves with gentle bottom slopes. This dissertation studies the mechanisms of WSGF over primarily muddy shelves through laboratory experiments in an oscillatory water tunnel with a sediment bed of either 1% or 13% sand fraction. Physics behind this includes sand fraction effects on the dynamics of WSGF under equilibrium state, the role of sand in controlling sediment suspensions under equilibrium state, and key factors that affect the dynamics of WSGF during the bed adjustment period before the equilibrium state.

First, sand fraction effects on the dynamics of wave-supported gravity flows in mud-dominant environments are investigated. Low and high energy regimes are differentiated based on a Stokes Reynolds number $Re_\Delta \approx 500$. In the low energy regime, the sand fraction influences flow dynamics primarily through ripple formation; no ripples form in the 1% sand experiments, whereas ripples form in the 13% experiments that increase turbulence and the wave boundary layer thickness, δ_m. In the high energy regime, small ripples form in both the 1% and 13% sand experiments and we observe high near-bed suspended sediment concentrations. The influence of stratification on the boundary layer flow is characterized in terms of the gradient Richardson number Ri_g. The flow is weakly stratified inside the boundary layer for all runs and critically stratified at or above the top of the boundary layer.

In the lower energy regime, the sand content reduces the relative influence of stratification in the boundary layer, shifting the elevation of critical stratification, L_B, from approximately $1.3\delta_m$ to $2.5\delta_m$ in the 1% and 13% experiments, respectively. In both sets of experiments $L_B \approx \delta_m$ at the strongest wave energy, indicating a transition to strongly stratified dynamics.

Second, sand particles control the sediment suspension over mud-dominant environments. High near-bed concentration and concentration gradient happen when the sand fractions suspend from the bed. The suspension of sand fraction in bed sediment mixture leads to the formation of a high suspended-sediment concentration layer. A modified sediment suspension criterion is created based on *Van Rijn* (1984) and using the median particle size of only the sand fraction in the bed and is successful in predicting the necessary suspension that contributes to wave-supported gravity flow formation. This modified sediment suspension criterion provides a limited condition for the formation of wave-supported gravity flows.

Finally, experimental results during bed adjustment periods are presented. The total bed adjustment before the equilibrium can be divided into three stages. Stage I, the initial adjustment stage, occurs in the first 30 - 40 min, where the non-uniformity of the bed introduces sediment redistribution and transient ripples start to form, and the bed elevation might increase or decrease. Stage II, the decreasing erosion stage, occurs during 30 - 90 min for 1% sand experiments or 40 - 105 min for 13% sand experiments, where the bed erosion rate is near a constant value. Stage III, the near-equilibrium stage, occurs in the final 15 min, where the bed erosion rate drops to near zero, upward transport flux is balanced with the settling flux, stratification is induced at the top of the wave boundary layer, and the system reaches an equilibrium state. Two different controlling mechanisms of the bed erosion and deposition are discussed: bed control, and stratification control. In our experiments, bed armoring due to the surface coarsening of the bed is observed, which decreases the bed erodibility. Transient ripples are observed in the total bed adjustment period, which elevates near-bed shear stress. The formation of transient ripples might slightly increase bed erosion.

Stratification plays a limited role in the near-bed sediment system during the bed adjustment period but becomes important when the equilibrium state is reached.

TABLE OF CONTENTS

LIST OF FIGURES

Figure Number Page

LIST OF TABLES

ACKNOWLEDGMENTS

First, I'd like to thank my advisor, Prof. Alexander R. Horner Devine. I have been really fortunate to have such an advisor to provide detailed guidance for the whole doctoral research. He is one of the most optimistic, tenacious, and talented people I have ever met. Alex has great patience and supports me not only from the advice of the scientific problems but discussions on technical details of performing the laboratory experiments. I could always feel great enthusiasm for science from Alex which also inspired me to complete this dissertation. I really could not have possibly imagined having a better advisor and mentor for my doctoral study.

I would also like to thank my committee Andrea Ogston, Tian-Jian Hsu, Chris Chickadel, and Alberto Aliseda. They offered invaluable advice and guidance on this thesis and the experimental progress for which I am extremely grateful. Special thanks to Andrea Ogston, who helps me a lot with the improvement of this research. The weekly meeting with her during Alex was in Chile really helps my research in progress. And this thesis cannot be finished without the generosity of her of letting me use many instruments for my experiments and great help on the scientific writing. I would also like to give special thanks to Tian-Jian (Tom) Hsu for all his help, support, motivation and for sharing his expertise on turbulence and numerical modeling.

I have appreciated the great support from the other graduate students or postdocs from the Environmental Fluid Mechanics (EFM) group at UW throughout the past five years. Great thanks to Jim for providing the expertise on waves, which helps a lot in improving Chapter 2. Many thanks to Ruth, Raul, Sam K, Christine, David, Sam F, Sam B, Shelby, Alexis, Jacob, Maricarmen, Maddie, Roxanne, Brad, and Seth. Special thanks to Ruth

who helped me a lot for adapting to the US life fast when I just arrived in Seattle and the grammar check general exam proposal, which improved it a lot. I really appreciate the help from Raul in discussing the scientific questions about WSGF and sharing his data from the Rhine River mouth which is very important for Chapter 3. Many thanks to my labmate Trevor Harrison in the Harris Hydraulics Lab who provides many great ideas on beautifying figures through Matlab. I will always remember a great time in Harris Lab with everyone as well as the weekly journal club of our EFM.

I am also grateful for the friendships I've made out of the lab. Xiangyu Xie, who is always the first choice to discuss scientific brainstorms, provided great help on mathematical questions, algorithms, and programming. Special thanks to Liangyi Yue, who brought up many good ideas in WSGF and shared his expertise on WSGF-modeling. Many thanks to Wenqi Zhu, Xiangyu Zhang, Yiran Zhang, Mengxin Liu, Xiang Yan, Zelong Bai, Yunen Li, and Jinfu Peng for the happiest life out of Science in Seattle. The memories of Friday cooking night in house 418 will always be remembered.

I would like to thank Abbas Hooshmand, Aaron Fricke, and Hannah Glover for the great technical support of the laboratory experiments. Special thanks to the great help on the experimental setup from Mohammad Jamous, especially on the attempts on natural sediment experiments. Great thanks to Richard P. Hale for providing his field data as verification for Chapter 3.

During the course of my study, I was supported by the National Science Foundation grant OCE-1537435, for which I am very grateful. Special thanks to Steve Burges and Sylvia Burges for providing the fellowship for one year and another quarter.

Finally, the great thanks to my parents, Ying Han and Yan Zhang, who are always my strong backing for completing this dissertation as well as my whole life.

DEDICATION

To my wonderful parents, Ying Han and Yan Zhang

Chapter 1

INTRODUCTION

1.1 Motivation

The transfer of fine sediment from the river mouth to deeper marine environments is an important component of source-to-sink sedimentary systems. Sediment can be deposited along the shoreline, on the continental shelf and ultimately may be deposited in the deep ocean. This process ultimately creates a record of long-term net accumulation (*Wright and Nittrouer*, 1995). Coarse sediments tend to settle near the estuary mouth or in shallow coastal regions; fine sediments can be transported farther and deposited on the continental shelf or may be moved off the shelf and deposited in deeper environments (*Walsh and Nittrouer*, 2009). Therefore, the physical mechanisms that contribute to cross-shelf transport on the continental shelf provide a crucial step in the overall source-to-sink sedimentary processes.

Studies over the past two decades have shown that wave-supported gravity flows (WSGF) contribute substantially to the total cross-shelf sediment transport (*Wright and Friedrichs*, 2006). WSGFs are gravity flows for which external shear stress primarily from waves induces sediment suspension on a gentle slope and a high-concentration layer is formed near the seabed. Sediment is then transported downslope due to the negative buoyancy of the high-concentration layer. Over the past twenty years, many field studies address the importance of WSGF events (e.g. *Ogston et al.*, 2000; *Wright et al.*, 2001; *Scully et al.*, 2002; *Traykovski et al.*, 2007; *Egan et al.*, 2020). However, due to the complexity of shelf environments and the limitation of observation methods, the detailed structure of WSGF is hard to resolve through field observations. Numerical models can resolve the structure of WSGF in great detail through appropriate assumption of the near-bed systems (e.g. *Hsu et al.*, 2009; *Ozdemir et al.*, 2010, 2014; *Zang et al.*, 2020). Recent studies also addressed the importance of grain

size effects on WSGF (e.g. *Flores et al.*, 2018), and sand fraction effects in mud-dominant environments has been suggested to be an important factor in WSGF dynamics (*Hooshmand et al.*, 2015).

Laboratory experiments are bridges between field measurements and numerical modeling, which not only simplifies the condition compared to shelf environments but also includes the potential effects that might control the dynamics of WSGF that numerical modeling might not include. In the past fifteen years, several experimental studies have investigated velocity, suspended sediment concentration, turbulence, and bedforms (*Lamb et al.*, 2004; *Lamb and Parsons*, 2005; *Liang et al.*, 2007; *Hooshmand et al.*, 2015). However, there is neither experimental work on the sand fraction effects on dynamics of WSGF in mud-dominant environments nor any experimental work focusing on the bed adjustment periods before the equilibrium state of the bed. The study of sand fraction effects will further unveil the role of sand in controlling the dynamics of WSGF and sediment suspension in the wave boundary layer. The investigation of bed adjustment from the initial condition to the equilibrium state will further address the key factors that control sediment suspensions, as WSGF is always presenting as an event and the seabed is always dynamical in shelf environments.

1.2 Studies on wave-supported gravity flows

A series of field studies starting in the 1990s have demonstrated the importance of sediment gravity flows on shelves with gentle slopes. Observations offshore of the Amazon River mouth (*Kineke and Sternberg*, 1995; *Kineke et al.*, 1996; *Sternberg et al.*, 1996) first showed that sediment gravity flows do not need steep slopes to support a high-concentration bottom suspension. In the case of the Amazon, strong convergence on the inner shelf and an extreme quantity of sediment supply supported these conditions. Near small rivers, episodic seasonal sediment inputs from rivers provide periods conducive to maintaining the near-bed high-concentration layer and offshore transport. Observations on the Eel River shelf provided further clues that external forces, mainly waves, can resuspend and maintain recently deliv-

ered sediment into high-concentration layers that move under the forces of gravity across the inner shelf. *Ogston et al.* (2000) and *Traykovski et al.* (2000) observed near-bed downslope velocity anomalies during concurrent storm and river flood events and found the thickness of the high-concentration layer to be on the same scale as the wave boundary layer. *Ogston et al.* (2000) suggested that the convergence of transport contributes to a high-concentration layer near the bed during a storm event and showed that short-duration storms were the main contributors to net sediment flux. *Traykovski et al.* (2007) made detailed measurements of the near-bed velocity and concentration profiles and calculated the gravitational sediment flux on both the Eel River shelf and the Po River prodelta. They found that events at both sites could be classified as either high concentration sediment gravity flows or low concentration transport. *Traykovski et al.* (2015) observed high wave energy dissipation and low normalized attenuation rates inside the high-concentration layer on the Louisiana shelf, and estimated kinematic viscosity inside the layer to be 2-3 orders of magnitude greater than the viscosity of clear water.

Field studies from many continental shelf regions have provided insights into the mechanics and importance of WSGF near river mouths, including the Atchafalaya River, Ganges-Brahmaputra River, Mississippi River, Po River, Rhone River, Waiapu River, Waipaoa River, Changjiang River, and Yellow River (*Wright et al.*, 1990; *Friedrichs and Wright*, 2004; *Wright and Friedrichs*, 2006; *Traykovski et al.*, 2007; *Ma et al.*, 2008; *Hale and Ogston*, 2015). In addition, many regional-scale models have also highlighted the importance of the WSGF on cross-shelf sediment transport (*Moriarty et al.*, 2015; *Harris et al.*, 2005; *Traykovski et al.*, 2007; *Harris et al.*, 2008). The ubiquity of wave-supported gravity flows supports the consideration that they can build a bridge between the coastal and offshore sediment transport.

To understand the dynamics of WSGF, detailed information is needed regarding the structure of the velocity and sediment concentration fields within such flows. However, the difficulty of documenting the high-resolution velocity and concentration profiles in the field has limited the complete understanding of the inner structure of WSGF, which are typically less than 10 cm thick. Therefore, a series of high-resolution numerical models and

lab experiments have been used to understand the detailed dynamics. *Hsu et al.* (2009) used a Reynolds-averaged two-equation model for fine sediment transport and found that the bulk Richardson number, which has been used in 1D gravity flow model closure, has a magnitude smaller than 0.25 and is determined by the availability of mud in the seabed. *Ozdemir et al.* (2010) carried out a series of 3D turbulence resolving simulations of fine sediment transport in an oscillatory bottom boundary layer. They showed that the oscillatory boundary layer over a smooth bottom is only transitionally turbulent at the Reynolds number in which WSGFs are typically observed. When sufficient amounts of fine sediments are suspended, the resulting stable density stratification can laminarize the boundary layer and limits the sediment carrying capacity. More recently, Ozdemir (2016) further showed that under the largest sediment carrying capacity at a shelf slope of 0.005, the peak downslope gravity current speed is no more than 1 cm/s. *Yue et al.* (2020) further included a more realistic erosional/depositional bottom and showed that wave direction can further increase downslope gravity flow speed, but only by a factor of 2. These numerical studies adopt the main assumption that the oscillatory boundary layer has a hydraulic smooth bottom, which may limit the sediment carrying capacity and hence the intensity of the resulting downslope gravity current. Laboratory experiments can simulate the near-bed conditions on the shelf and document the high-resolution velocity, turbulence, and concentration structures. For example, *Lamb et al.* (2004) measured the velocity profiles within a high-concentration bottom turbid layer with zero slopes. They found that sediment suspension suppressed the wave boundary layer thickness, but flows were able to support a high-concentration suspension layer that was thicker than the wave boundary layer due to upward transport of turbulent energy.

1.3 The role of sand in mud-dominant environments

The vast majority of continental shelves where WSGFs have been observed are predominantly muddy environments. Recent studies suggest that even when the sand fraction is small, it may exert a dominant control on the dynamics of these systems (*Hooshmand et al.*, 2015).

Another study by *Flores et al.* (2018) describes a WSGF event on the continental shelf offshore of the Rhine River mouth, where the bed sediment is mainly sand. This observation broadens the understanding of WSGF and inspires us to re-think particle size effects on the dynamics of WSGF. Recent laboratory experiments also provide some clues that sediment particle size seems to play an essential role in controlling the dynamics of WSGFs. *Lamb and Parsons* (2005) found that the increase of sand fraction in the high concentration layer. A sandy near-bed transport layer formed with the same initial bed sand content, which helps to form ripples and alters the bottom roughness under oscillatory flow conditions (*Liang et al.*, 2007). *Hooshmand et al.* (2015) described two regimes: a low energy regime, in which the dynamics are controlled by ripple-generated turbulence, and a high energy regime, in which the dynamics are controlled by density stratification. They suggested that the sand fraction of the sediment mixture may set the threshold between these regimes. These observations and laboratory experiments emphasize the significance of the role of sand content in mixed grain-size sediments on WSGF dynamics. However, sediment used in all of these experiments had 10-20% sand, similar to many continental shelf muddy environments. It is still unknown how different sand fractions, especially low sand content, affect the turbulent flow structure as well as the role of density stratification on the initiation and maintenance of WSGF.

1.4 Thesis outline

This thesis aims to answer three questions related to the role of sand in wave-supported gravity flows over primarily mud-dominant seabeds. The questions are answered with the data from laboratory experiments conducted at the University of Washington. The three questions are:

- How do turbulence and sediment concentration change when the sand fraction of the sediment in the wave-supported gravity flows alters?

- How does the particle size distribution, especially sand content, control the sediment suspension in mud-dominant environments?

- In the near-bed sediment suspension system, what are the key factors in bed erosion? What are the temporal characteristics during the bed adjustment periods before the equilibrium state?

In Chapter 2, new laboratory experiment results using bed sediments consisting of 1% sand and 13% sand fractions the equilibrium state are used to determine how the sand fraction affects the turbulence and sediment suspension inside the wave boundary layer on mud-dominant environments. These experiments expand on prior experiments by *Lamb et al.* (2004) and *Hooshmand et al.* (2015), considering, in particular, the very low (1%) sand fraction case for the first time. The velocity, turbulence, and sediment concentration are compared for two sediment mixtures. The dynamical regime transition under varying wave intensity is identified, and the vertical role of sediment-induced density stratification is discussed. This chapter has been reproduced with minor changes from,

> Han, Z., Horner-Devine, A. R., Ogston, A. S., Hsu, T.-J. (2021). The role of sand in wave boundary layers over primarily muddy seabeds: Implications for wave-supported gravity flows. Journal of Geophysical Research: Oceans, 126, e2020JC016621.

In Chapter 3, we identify the sand control of sediment suspension in wave-supported gravity flows. The sediment concentration, ripple structure, suspended sediment grain size are compared. We propose a modified sediment suspension criterion based on the median grain size of only the sand content, reflecting the sand fraction influence in mud-dominant environments. Two data sets from the field are used to verify this criterion. This work will be submitted with the following title and co-authors,

> Han, Z., Horner-Devine, A. R., Ogston, A. S., Hsu, T.-J. Sand control of sediment suspension in wave-supported gravity flows.

In Chapter 4, bed adjustment experiment results before the equilibrium state are presented, which are used to show how the bed and near-bed turbulence respond when the bed

is eroding. The temporal characteristics of Reynolds shear stress, sediment concentration, bed elevation, transient ripple structure are documented. Different stages during the bed adjustment period are classified based on the bed erosion rate. Key factors in bed erosion, including bed erodibility, transient ripples effects on sediment suspension, sediment-induced stratification, and sediment settling, are discussed. Different scenarios that control the equilibrium state are discussed.

Finally, Chapter 5 provides a summary and a discussion of future directions on these topics.

Chapter 2

THE ROLE OF SAND IN WAVE BOUNDARY LAYERS OVER PRIMARILY MUDDY SEABEDS: IMPLICATIONS FOR WAVE-SUPPORTED GRAVITY FLOWS

2.1 Introduction

Terrestrial sediments introduced into coastal regions by rivers are deposited on the seabed, and subsequently may be resuspended by waves and dispersed by shelf processes such as tidal and geostrophic currents (*Gao et al.*, 2016). This process ultimately creates a record of long-term net accumulation (*Wright and Nittrouer*, 1995). Coarse sediments tend to settle near the estuary mouth or in shallow coastal regions; fine sediments can be transported farther and deposited on the continental shelf or may be moved off the shelf and deposited in deeper environments (*Walsh and Nittrouer*, 2009). Therefore, the physical mechanisms that contribute to cross-shelf transport on the continental shelf provide a crucial step in the overall source-to-sink sedimentary processes. One mechanism to move sediment across-isobath is through sediment gravity flows. However, the cross-isobath gradient of most shelf environments is too gentle to support auto-suspension of sediment and downslope transport due to gravity alone (*Wright and Friedrichs*, 2006). External shear, typically driven by waves and tides, is necessary to maintain sufficient sediment suspension and support downslope gravitational transport. This process, which is referred to as a wave-supported gravity flow (WSGF), has been shown to be an important mode of cross-shelf sediment transport on many muddy continental shelves (e.g. *Wright and Friedrichs*, 2006; *Traykovski et al.*, 2007; *Hale and Ogston*, 2015; *Flores et al.*, 2018).

A series of field studies starting in the 1990s have demonstrated the importance of sediment gravity flows on shelves with gentle slopes. Observations offshore of the Amazon River

mouth (*Kineke and Sternberg*, 1995; *Kineke et al.*, 1996; *Sternberg et al.*, 1996) first showed that sediment gravity flows do not need steep slopes to support a high-concentration bottom suspension. In the case of the Amazon, strong convergence on the inner shelf and an extreme quantity of sediment supply supported these conditions. Near small rivers, episodic seasonal sediment inputs from rivers provide periods conducive to maintaining the near-bed high-concentration layer and offshore transport. Observations on the Eel River shelf provided further clues that external forces, mainly waves, can resuspend and maintain recently delivered sediment into high-concentration layers that move under the forces of gravity across the inner shelf. *Ogston et al.* (2000) and *Traykovski et al.* (2000) observed near-bed downslope velocity anomalies during concurrent storm and river flood events and found the thickness of the high-concentration layer to be on the same scale as the wave boundary layer. *Ogston et al.* (2000) suggested that the convergence of transport contributes to a high-concentration layer near the bed during a storm event and showed that short-duration storms were the main contributors to net sediment flux. *Traykovski et al.* (2007) made detailed measurements of the near-bed velocity and concentration profiles and calculated the gravitational sediment flux on both the Eel River shelf and the Po River prodelta. They found that events at both sites could be classified as either high concentration sediment gravity flows or low concentration transport. *Hale and Ogston* (2015) used a simple model to estimate the time for an observed WSGF to reach the shelf edge based on observations on the continental shelf offshore of the Waipaoa River, New Zealand, and found that the flow would take around 2-10 days. *Traykovski et al.* (2015) observed high wave energy dissipation and low normalized attenuation rates inside the high-concentration layer on the Louisiana shelf, and estimated kinematic viscosity inside the layer to be 2-3 orders of magnitude greater than the viscosity of clear water.

Field studies from many continental shelf regions have provided insights into the mechanics and importance of WSGF near river mouths, including the Atchafalaya River, Ganges-Brahmaputra River, Mississippi River, Po River, Rhone River, Waiapu River, Waipaoa River, Changjiang River, and Yellow River (*Wright et al.*, 1990; *Friedrichs and Wright*, 2004; *Wright*

and Friedrichs, 2006; *Traykovski et al.*, 2007; *Ma et al.*, 2008; *Hale and Ogston*, 2015). In addition, many regional-scale models have also highlighted the importance of the WSGF on cross-shelf sediment transport (*Moriarty et al.*, 2015; *Harris et al.*, 2005; *Traykovski et al.*, 2007; *Harris et al.*, 2008). The ubiquity of wave-supported gravity flows supports the consideration that they can build a bridge between the coastal and offshore sediment transport.

To understand the dynamics of WSGF, detailed information is needed regarding the structure of the velocity and sediment concentration fields within such flows. However, the difficulty of documenting the high-resolution velocity and concentration profiles in the field has limited the complete understanding of the inner structure of WSGF, which are typically less than 10 cm thick. Therefore, a series of high-resolution numerical models and lab experiments have been used to understand the detailed dynamics. *Hsu et al.* (2009) used a Reynolds-averaged two-equation model for fine sediment transport and found that the bulk Richardson number, which has been used in 1D gravity flow model closure, has a magnitude smaller than 0.25 and is determined by the availability of mud in the seabed. *Ozdemir et al.* (2010) carried out a series of 3D turbulence resolving simulations of fine sediment transport in an oscillatory bottom boundary layer. They showed that the oscillatory boundary layer over a smooth bottom is only transitionally turbulent at the Reynolds number in which WSGFs are typically observed. When sufficient amounts of fine sediments are suspended, the resulting stable density stratification can laminarize the boundary layer and limits the sediment carrying capacity. More recently, Ozdemir (2016) further showed that under the largest sediment carrying capacity at a shelf slope of 0.005, the peak downslope gravity current speed is no more than 1 cm/s. *Yue et al.* (2020) further included a more realistic erosional/depositional bottom and showed that wave direction can further increase downslope gravity flow speed, but only by a factor 2. These numerical studies adopt the main assumption that the oscillatory boundary layer has a hydraulic smooth bottom, which may limit the sediment carrying capacity and hence the intensity of the resulting downslope gravity current. Laboratory experiments can simulate the near-bed conditions on the shelf and document the high-resolution velocity, turbulence, and concentration structures. For ex-

ample, *Lamb et al.* (2004) measured the velocity profiles within a high-concentration bottom turbid layer with zero slopes. They found that sediment suspension suppressed the wave boundary layer thickness, but flows were able to support a high-concentration suspension layer that was thicker than the wave boundary layer due to upward transport of turbulent energy.

Hooshmand et al. (2015) reported that sediment-induced stratification can be important in WSGFs, reducing turbulence intensity when the sediment concentration is high under strong wave conditions. In addition, stratification played varying roles at different elevations above the sediment bed. *Chen and Chen* (2018) used an analytical model and numerical modeling to investigate the dynamics of turbulence in unidirectional sediment stratified flows. They defined a length scale L_B, based on the Monin-Obukhov length scale multiplied by a factor of 0.1, to divide the water column into two regions. This length scale is also the height above the bed z, where the flux Richardson number $Ri_f = 0.1$. Below $z = L_B$, $Ri_f < 0.1$, stratification is of secondary importance, and velocity and concentration profiles follow logarithmic and Rousean profiles, respectively. Above $z = L_B$, the water column maintains a critically stratified state. The present work will evaluate whether a similar boundary layer structure is observed in oscillatory flows in order to inform future WSGF models.

The vast majority of continental shelves where WSGFs have been observed are dominantly muddy environments, and this has been thought to be one of the prerequisites of WSGF formation (*Wright and Friedrichs*, 2006). However, a recent study by *Flores et al.* (2018) describes a WSGF event on the continental shelf offshore of the Rhine River mouth, where the bed sediment is mainly sand. This observation broadens the understanding of WSGF and inspires us to re-think particle size effects on the dynamics of WSGF. Recent laboratory experiments also provide some clues that sediment particle size seems to play an essential role in controlling the dynamics of WSGFs. *Lamb and Parsons* (2005) found that sand fraction in the high concentration layer increased from 27% to 78% for an initial bed sand content of 20%, and showed that the winnowing of the bed caused the high concentra-

tion layer to coarsen, in turn reducing the thickness of the high concentration layer. *Liang et al.* (2007) found that a sandy near-bed transport layer formed with the same initial bed sand content, which helps to form ripples and alters the bottom roughness under oscillatory flow conditions. *Hooshmand et al.* (2015) described two regimes: a low energy regime, in which the dynamics are controlled by ripple-generated turbulence, and a high energy regime, in which the dynamics are controlled by density stratification. They suggested that the sand fraction of the sediment mixture may set the threshold between these regimes. These observations and laboratory experiments emphasize the significance of the role of sand content in mixed grain-size sediments on WSGF dynamics. However, sediment used in all of these experiments had 10-20% sand, similar to many continental shelf muddy environments. It is still unknown how different sand fractions, especially low sand content, affect the turbulent flow structure as well as the role of density stratification on the initiation and maintenance of WSGF.

The results summarized above suggest that the sand fraction in mud-dominant environments is important in the dynamics of bottom boundary layers and WSGFs. The objective of the present work is to clearly quantify the role that the sand component plays. In this paper, we present new experimental results using bed sediments consisting of 1% sand and 13% sand fractions. These experiments expand on prior experiments by *Lamb et al.* (2004) and *Hooshmand et al.* (2015), considering, in particular, the very low (1%) sand fraction case for the first time. The very low sand component will further help confirm the role of sand in ripple formation and turbulent structure in mud-dominant environments. Comparisons between these two different sediment mixtures are used to investigate the bed response, boundary layer turbulence, and sediment suspension differences in the formation of WSGF. In Section 2.3.1 we show how the bedforms change with reduced sand fractions. Sections 2.3.2, 2.3.3 and 2.3.4 describe the velocity, sediment concentration profiles and turbulence, respectively. In Section 2.4.1 and 2.4.2, we discussed the lutocline formation and dynamical regime transition when the wave intensity changes. In Section 2.4.3, we discuss the role of sediment-induced density stratification in WSGF and the influence of sand fraction on strat-

ification. The main physical parameters measured and analyzed include bed ripple steepness (η/λ), along-channel vertical velocity profiles (u), boundary layer thickness (δ_m), near-bed concentration (C_{NB}), and vertical gradient of sediment concentration ($\partial C/\partial z$), turbulence statistics (TKE, Reynolds stress, shear production P, turbulent dissipation rate ϵ), gradient Richardson number (Ri_g) profiles, and buoyancy length scale (L_B).

2.2 Experimental setup and analysis

The experiments were conducted in an oscillating water tunnel with a sediment bed designed for high-resolution measurements of near-bed velocities, turbulence, and sediment concentrations. The experimental facility is the same facility used by *Hooshmand et al.* (2015) with one major modification. The water balance system was improved to retain the balance of water on the piston side to make the piston movement more sinusoidal. After this improvement, we redid 7 sets of the rough wall (RW) experiments with no sediment, where sand particles of $D_{50} = 750$ μm were glued on an acrylic sheet to serve as the bed at the bottom of the tank (Table 4.2). The velocity structure and turbulence in the wave boundary layer were compared with prior results from *Hooshmand et al.* (2015) and we confirmed that the modifications to the facility did not significantly influence the dynamics.

Table 2.1: Rough wall and sediment bed experiment parameters[a]

Rough wall

Run	R1	R2	R3	R4	R5	R6	R7
U_{orb} (cm s^{-1})	35.3	23.4	44.4	53.7	16.5	24.7	32.1
T (s)	10.1	15.4	7.8	6.2	14.8	10.1	7.8
δ_m (cm)	2.2	2	2.3	2.6	1.8	2.1	2.2
Re_Δ	593.9	480.3	653.5	707.1	340.6	414.7	472.9
u_* (cm s^{-1})	1.10	0.67	1.55	1.79	0.59	0.84	1.04

TKE (cm^2s^{-2})	4.56	1.82	6.22	14.05	0.56	1.85	3.36
P (cm^2s^{-3})	7.83	0.83	18.39	27.71	0.19	2.92	4.22
ϵ (cm^2s^{-3})	6.65	0.58	12.09	21.23	0.17	2.46	2.84

1% sand sediment

Run	S1	S2	S3	S4	S5	S6	S7	S8	S9
U_{orb} (cm s^{-1})	14.8	21.1	29.5	36.8	46.8	14.7	21.2	29.9	35.6
T (s)	15.9	11.3	8.2	6.6	5.2	15.5	11.1	8.1	6.8
Re_Δ	309.6	378.1	444.1	490.5	542.2	300.4	373.4	441.2	478.7
δ_m (cm)	1.5	1.8	1.9	2.3	1.8	1.2	1.6	1.7	1.9
u_* (cm s^{-1})	0.30	0.72	0.92	1.01	2.71	0.42	0.79	0.65	1.10
TKE (cm^2s^{-2})	0.15	0.48	1.74	3.11	7.23	0.33	0.33	0.93	2.21
P (cm^2s^{-3})	0.01	0.19	1.34	2.34	3.29	0.20	0.14	0.45	2.82
ϵ (cm^2s^{-3})	0.01	0.20	1.39	2.02	4.09	0.07	0.07	0.47	1.27
λ (cm)	flat	6.50	4.23	-	5.03	flat	flat	-	-
η (cm)	flat	0.10	0.20	-	0.10	flat	flat	-	-
Run	S10	S11	S12	S13	S14	S15	S16	S17	S18
U_{orb} (cm s^{-1})	43.6	14.2	21.8	30.0	36.2	22.9	31.2	45.7	55.1
T (s)	5.5	16.7	11.1	8.0	6.6	15.5	10.8	8.1	6.4
Re_Δ	528.9	292.9	383.0	445.1	474.5	475.9	541.6	625.6	661.0
δ_m (cm)	1.9	1.1	1.7	1.8	2.3	1.2	2.3	2.3	2.1
u_* (cm s^{-1})	1.54	0.49	0.44	1.06	1.21	0.65	0.90	1.87	1.35
TKE (cm^2s^{-2})	4.14	0.23	0.49	2.33	0.55	0.33	1.78	5.10	3.04
P (cm^2s^{-3})	6.70	0.08	0.18	1.90	2.04	0.35	2.54	5.99	5.39
ϵ (cm^2s^{-3})	3.68	0.07	0.21	1.64	3.06	0.25	1.85	3.77	3.34
λ (cm)	-	flat	flat	7.06	5.91	-	5.05	6.50	8.50
η (cm)	-	flat	flat	0.53	0.10	-	0.33	0.25	0.24

13% sand sediment

Run	S19	S20	S21	S22	S23	S24	S25
U_{orb} (cm s^{-1})	15.9	22.2	29.8	15.8	33.9	46.8	56.1
T (s)	15.6	11.2	8.1	15.6	10.9	7.8	6.3
Re_Δ	310.7	380.4	443.5	461.1	561.9	639.5	686.8
δ_m (cm)	2.2	2.4	3.7	3.3	3.35	2.3	2.2
u_* (cm s^{-1})	1.33	0.99	1.55	1.67	2.68	1.84	1.21
TKE (cm^{2}s^{-2})	0.45	1.26	5.44	5.09	8.83	4.53	3.17
P (cm^{2}s^{-3})	0.26	1.32	5.15	3.25	12.37	3.08	1.73
ϵ (cm^{2}s^{-3})	0.19	0.69	5.93	3.23	5.52	2.41	1.01
λ (cm)	-	3.35	5.64	5.01	5.48	7.57	-
η (cm)	-	0.2	0.59	0.38	0.43	0.3	-

[a] Re_Δ represents the Stokes Reynolds number calculated from equation (2.7). u_*, TKE, P, ϵ represents the averaged shear velocity, turbulent kinetic energy, shear production, and turbulent dissipation rate inside the wave boundary layer. λ represents the ripple wavelength. η represents the ripple height. For the data of ripple parameter, "flat" means the bed is flat; "-" means we are lack of accurate measurements of the corresponding ripple parameter.

2.2.1 Wave apparatus

The oscillating water tunnel has a 5 m long, 1 m high and 0.2 m wide experimental section with a closed top (Figure 2.1). The sidewalls are made of smooth acrylic Plexiglas. The near sinusoidal oscillatory flows in the experimental section are driven by a vertical piston on one end which produces periods of $5-15$ s and wave orbital velocities of $15-60$ cm s^{-1}. The left end tank is open at the top to provide the pressure difference. The wave tunnel

produces horizontal oscillatory motion, which simulates one-dimensional fluid motions driven by surface gravity waves as they are felt on the seabed of continental shelves.

2.2.2 Sediment bed setup

For sediment bed experiments (Table 4.2), sediment was placed in a 10 cm thick layer at the bottom of the tank, replacing the acrylic sheet used in the RW experiments. The 1% sand sediment runs used U.S. Silica Sil-co-Sil 45 crushed silica, with portions of clay:silt:sand grain sizes being 0.27:0.72:0.01, based on the classification by *Wentworth* (1922). The median particle size of this sediment is $D_{50} = 11.79$ μm, and the distribution is poorly sorted with $D_{90}/D_{10} = 26.2$. The 13% sediment bed runs, reported in *Hooshmand et al.* (2015), used U.S. Silica Sil-co-Sil 106 crushed silica with proportions of clay:silt:sand grain sizes being 0.20:0.67:0.13. The corresponding $D_{50} = 22.84$ μm, and the distribution was more poorly sorted with $D_{90}/D_{10} = 40.7$. The sediment we use is crushed silica without any clay minerals. We refer to this as "mud", but it is important to recognize that, while the grain size distribution is consistent with muddy sediments, our mixture is not as cohesive as naturally occurring muds. The sediment we used should be considered weakly cohesive silicious mud. To make sure the updated wave flume has similar results for 13% sand experiments, we redid seven runs using the 13% sand fraction sediment bed (Table 4.2). The particle size distribution of the bed sediment was evaluated using a Beckman Coulter LS13-320 Particle Size Analyzer and is shown in Figure 2.1. Before the start of each run, we raked the sediment bed, making it as level as possible to initialize a plane bed. Sediment was added before the run and allowed to consolidate for two days after filling up the tank with fresh water for all runs to ensure that each run started with a consistent state of bed consolidation.

2.2.3 Velocity and turbulence measurement

Instruments for measuring velocity, turbulence, and sediment concentration were placed in the middle of the experimental section to minimize impacts from vortices generated at the transition between the experimental section and the end tanks. Velocity and turbulent

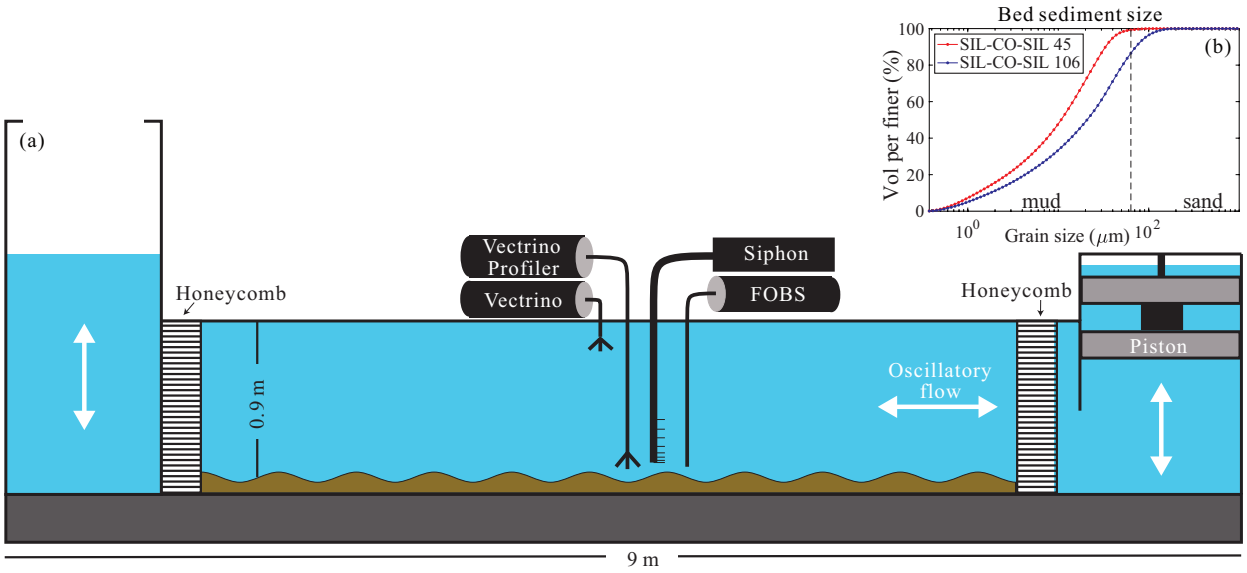

Figure 2.1: (a) Schematic oscillating water tunnel. Oscillatory motion is driven by the piston on the right. The width of the tank in the middle section is 0.2 m. (b) The cumulative bed sediment particle size distribution for 1% sand fraction sediment (SIL-CO-SIL 45) and 13% sand fraction sediment (SIL-CO-SIL 106).

fluctuations were measured using Acoustic Doppler velocimeters (ADV): an ADV profiler and a single-point ADV. The Nortek Vectrino Profiler was placed near the sediment bed to measure the three-dimensional velocities with a vertical resolution of 1 mm and a sampling rate of 100 Hz. The vertical profile range of the Vectrino Profiler is 40 mm. However, we only use the middle 15 bins, which are located where the signal-to-noise ratio (SNR) is maximal; the near-top and near-bottom bins have lower SNR. For each run, the Vectrino Profiler was moved incrementally upwards 8 times to obtain a 12 cm vertical profile. Since sediment needs some time to be dispersed throughout the tank, we powered the piston for each run and operated for 30 min to reach a quasi-steady state before the beginning of data collection. For some high wave orbital velocity runs, however, measurements needed to be made prior to quasi-steady state being reached due to rapid erosion of the bed. The single-point ADV Nortek Vectrino, which also has a sampling rate of 100 Hz, was placed 70 cm above the bed in the free-stream flow. It was synced with the Vectrino Profiler to provide a free stream velocity phase and was used as the reference for the phase difference in the wave boundary layer.

2.2.4 Concentration measurement

Suspended sediment concentrations (SSC) were measured with both an 8-port vertical sediment siphon rake and an array of fiber-optic backscattering sensors (FOBS). The FOBS array has 20 sensors with 10 mm spacing between the lowermost 10 sensors and progressively wider spacing above, which in total provided a 50 cm SSC profile. The FOBS was calibrated with Sil-co-Sil 45 and Sil-co-Sil 106 sediments separately in a mixing tank, and the calibrations showed linear responses for concentrations below 80 g L^{-1}. The sediment siphon rake sampled at eight different elevations with a 2 mm spacing between the lowermost 2 ports and wider spacing above. During the experiments, 50 ml water was siphoned from each port at a relatively constant flow rate. These samples were dried in a 60°C oven and then weighed to determine the SSC, following the procedure of *Lamb et al.* (2004).

Suspended sediment concentration in the tank needed some time to reach equilibrium.

However, the siphon rake could only take limited samples during each run. Calibrated FOBS data provide concentration time series. At the start of each run, we found that suspended sediment concentration in the tank increased in the whole tank, corresponding to continuous erosion of the bed. Sediments diffused upward until the concentration profile became relatively stable. In our experiments, the background concentration (the concentration throughout the profile in the tank) increased as wave energy increased and was influenced by the erosion of the bed as well as limited advection from the end tank. Since sediment-induced stratification affects the dynamics of WSGF and is usually dependent upon the concentration gradient instead of the concentration itself, background concentration is subtracted from each run (Section 2.3.3).

2.2.5 Bedform measurement

Ripple heights (η) and wavelengths (λ) inside the test section were based on observation with a camera through the test section sidewall. These were measured once a quasi-steady state was reached, coincident with the velocity and SSC measurements. Ripple steepness (η/λ) was calculated based upon the averaged η and λ in each run.

2.2.6 Data analysis

Time-series of all three velocity components u, v, and w were measured, representing along-channel, cross-channel, and vertical velocity, respectively. The raw time series velocity data were despiked using a three-dimensional phase-space method, which was developed by *Goring and Nikora* (2002) and updated by *Mori et al.* (2007). To separate wave orbital motion and turbulence, the despiked data were filtered by tenth-order Butterworth filter with a cutoff frequency of 1.25 Hz following *Lamb et al.* (2004) and *Hooshmand et al.* (2015). Similar methods with a 1 Hz (*Foster et al.*, 2000) and a 2 Hz (*Smyth et al.*, 2002) cutoff frequency have been used.

Wave orbital velocity was calculated based on $U_{orb} = \sqrt{2}U_{rms}$ where U_{rms} is the root mean square free stream velocity. We use velocity above $z = 10$ cm as the free stream velocity.

The wave period (T) was calculated as the mean period of zero-crossing in the velocity time series.

The characteristics of the wave boundary layer were estimated based on the velocity profiles. Based on the vertical structure of the oscillatory flows, three distinct zones are observed. From bottom to top these are: the wave boundary layer zone ($\partial U/\partial z > 0$), the overshoot zone ($\partial U/\partial z < 0$), and the free-stream zone ($\partial U/\partial z \approx 0$). The wave boundary layer thickness was defined as the location of the velocity maximum that occurs at the top of the wave boundary layer, below the overshoot zone (*Hooshmand et al.*, 2015). In a half wave period, the thickness of the wave boundary layer increased from the beginning of the wave period until its maximum thickness at flow reversal, and then a new boundary layer formed. We quantify the wave boundary layer thickness based on the maximum thickness (δ_m) observed in the phase-averaged velocity profiles, as this was the most robust measure of the time-varying boundary layer thickness.

The Reynolds stresses per unit mass were calculated as $-\overline{u'w'}$, where the overbar represents the phase average of the measured data. The Vectrino Profiler has the fourth receiver so it makes two separate measurements of vertical velocity w. Turbulent velocity data (u', v', and w') were processed using cospectral analysis to reduce the influences of noise and provide a better estimate of turbulent velocities (*Hurther and Lemmin*, 2001). Normally u_* is estimated based on the law of the wall, and two prerequisites should be satisfied when using the law of the wall: the bed roughness scale z_0 much smaller than the boundary layer thickness (*Grant and Madsen*, 1986) and the stratification is minimal. In our experiments, neither of those conditions were satisfied. Therefore, the shear velocity was estimated based on the averaged Reynolds stress: $u_* = \left(-\overline{u'w'}\right)^{1/2}$ over the wave boundary layer and the wave period.

For turbulent motions, turbulent kinetic energy (TKE) was calculated as

$$TKE = \frac{1}{2}\left(u'^2 + v'^2 + w'^2\right) \tag{2.1}$$

The evolution of TKE is governed by

$$\frac{\mathrm{d}(TKE)}{\mathrm{d}t} = P + T - B - \epsilon \tag{2.2}$$

where P, T, B, and ϵ represent shear production, transport flux, buoyancy flux, and dissipation rate, respectively. For TKE production in equation (2.2), we use

$$P \approx -\overline{u'w'}\frac{\partial U}{\partial z} \tag{2.3}$$

where U is the phase-averaged horizontal mean velocity. We calculate ϵ using the inertial dissipation method (*Tennekes and Lumley*, 1972) based on the turbulent velocity spectrum

$$S_{11}(k) = a\epsilon^{2/3}k^{-5/3} \tag{2.4}$$

where $a = 0.5$ is the universal Kolmogorov constant. Following *Lumley and Terray* (1983) and *Lamb et al.* (2004) and using Taylor's hypothesis of frozen turbulence, we use the vertical velocity spectra to determine ϵ based on

$$S_{11}(\omega) = S_{33}(\omega) \rightarrow \frac{7}{9}2^{1/3}\Gamma(\frac{1}{3})a\epsilon^{2/3}U_{orb}^{2/3}\omega^{-5/3} \tag{2.5}$$

where Γ denotes the Gamma function. Here $\int_{-\infty}^{+\infty} S_{33}(\omega)\mathrm{d}\omega$ is the total vertical velocity variance. Although the derivation from *Lumley and Terray* (1983) was originally for ocean surface wave orbital motions, it has been used in the marine bottom boundary layers as well where wave motions are horizontal oscillations (*Gross et al.*, 1994).

Phase-averaged values of the velocity, Reynolds stress, and turbulence kinetic energy (TKE) were calculated using the free stream reference phase from the single-point ADV. To get phase-averaged values, time-series data were quality-controlled and $20 - 50$ wave periods were averaged with phase in a $2\pi/120$ phase resolution and 1 mm vertical resolution, following the procedure of *Hooshmand et al.* (2015). For TKE evolution terms, including P and ϵ, the boundary layer averaged value is based on the averaged value inside the maximum boundary layer height of the total phase.

We use the Richardson number to understand the role of stratification during the strong wave forcing conditions. The flux Richardson number (Ri_f = B/P), the ratio of B and P, is appropriate for characterizing stratified turbulent environments. However, it is difficult to get an accurate buoyancy flux in our measurements and so we could not obtain an accurate estimate of Ri_f. More often, the gradient Richardson number is defined in the stratified shear flow:

$$Ri_g = -\frac{g(\partial\rho/\partial z)}{\rho(\partial U/\partial z)^2} \approx -\frac{gs(\partial c/\partial z)}{\rho_s(\partial U/\partial z)^2} \tag{2.6}$$

where $s = (\rho_s - \rho_w)/\rho_w$ is submerged weight of siliceous sediment relative to the water, c is mass concentration of sediment, ρ is seawater density and ρ_s is siliceous sediment density. With the limitation of FOBS vertical resolution, the FOBS sediment concentration profile was curve-fit and then the concentration gradient was calculated at 1 cm resolution from the fit to obtain Ri_g. The velocity shear $\overline{|\partial U/\partial z|}$ is computed as the absolute mean of the phase-averaged velocity shear to characterize the strength of velocity shear in the wave orbital motion.

We used the Stokes Reynolds number, Re_Δ, to initially characterize the wave intensity and differentiate between each experimental run, which is defined as

$$Re_\Delta = \frac{U_{orb}\tilde{\Delta}}{\nu} \tag{2.7}$$

where $\tilde{\Delta} = \sqrt{2\nu/\omega}$ is the thickness of the Stokes boundary layer, ν is the kinematic viscosity of water and ω is the radian frequency of the oscillatory motion. This choice follows several recent field, laboratory, and numerical model studies that have used Stokes Reynolds number to represent the wave energy intensity (e.g. *Hino et al.*, 1983; *Cheng et al.*, 2015; *Egan et al.*, 2020; *Yue et al.*, 2020), as well as prior experiments in the same facility (*Hooshmand et al.*, 2015). Because Re_Δ characterizes only the wave intensity, differences in the boundary layer dynamics associated with sediments such as grain roughness, ripple formation, or sediment stratification are evident. The latter processes are characterized in terms of bed roughness Reynolds number as discussed below. The use of Re_Δ introduces a constraint on our experiments resulting from its dependence on both U_{orb} and T, which cannot be changed

independently in our tank due to the mechanics of the piston system. It is possible to generate the same value of Re_Δ by changing the piston stroke length and power to opposite extremes and obtaining different U_{orb} and T combinations. We observe that these cases result in different turbulent dynamics, despite the same Re_Δ and conclude that they lie outside the parameter range that is well-characterized by our tank. These cases have been omitted from our calculations. Case S15 ($Re_\Delta = 476$) is retained on our list as an example, but not used in the analysis.

In addition to the dependence on the intensity of wave forcing, turbulence in the wave boundary layer will depend on the bed roughness, which is characterized in our experiments in terms of the bed roughness Reynolds number Re_*:

$$Re_* = u_* k_s / \nu \tag{2.8}$$

where $u_* = \sqrt{f_w/2} U_{orb}$ (*Grant and Madsen*, 1986), $f_w = \exp[5.213(k_s/a_b)^{0.194} - 5.977]$ is the friction factor (*Swart*, 1974), a_b is the wave orbital semi-excursion amplitude near the bed, and $k_s = 27.7\eta(\eta/\lambda)$ with ripples (*Grant and Madsen*, 1982) and $k_s = D_{50}$ without ripples (*Nikuradse*, 1933). In general, low values of Re_* indicate that the roughness elements due to sediment grains or ripples are smaller than the viscous sublayer thickness and the bed is considered to be hydraulically smooth. High values of Re_* indicate a rough bed in which the roughness elements protrude through the viscous sublayer and contribute to the generation of turbulence and drag.

2.3 Results

2.3.1 Bedforms

In our experiments, a major influence of particle size is the formation of bed ripples. All of the ripples observed in the 1% sand fraction experiments are in the anorbital range based on the classification by *Wiberg and Harris* (1994) (Figure 2.2b). Ripples observed in the 13% sand experiments are also primarily in the anorbital range, except in the lowest Re_Δ experiments, in which ripples are in the suborbital range. In general, our data fits the model from *Wiberg*

and Harris (1994) well. *Nielsen* (1981) used mobility number ($\psi = U_{orb}^2/(s-1)gD_{50}$) or wave Shields parameter ($\theta = u_*^2/(s-1)gD_{50}$, where $u_*^2 = 1/2 f_w U_{orb}^2$) to predict ripple geometry. Based on our data, the ripple steepness decreased as the wave Shields parameter increased (Figure 2.2c), and the model from *Nielsen* (1981) underestimated the ripple steepness in mud-dominant sediment settings.

For anorbital ripples *Wiberg and Harris* (1994) predict that the wavelength scales with the grain size according to $\lambda_{ano} = 535D$. This expression underestimates the ripple wavelength observed in our experiments by almost an order of magnitude, however, based on the median grain size D_{50} (Figure 2.2a). The result suggests that D_{50} is not an appropriate predictor of ripple characteristics in a mud-dominant sediment mixture.

We also compared ripple geometry changes with variations in wave forcing and find that the ripple steepness trends for the two bed sediment settings were different. For 13% sand fraction, the ripple steepness decreases as Re_Δ increases (Figure 2.2d). For 1% sand fraction, however, no ripples formed when $Re_\Delta < 400$. A regime shift was observed for $Re_\Delta > 400$; ripples started to form and ripple steepness decreased as Re_Δ increased. Under high Re_Δ the ripple steepness for 1% sand becomes similar to that of 13% sand experiments. *Hooshmand et al.* (2015) found that for 13% sand the ripple steepness decreased with an increase of wave forcing (Re_Δ), which is consistent with *Wiberg and Harris* (1994) as higher U_{orb} has the capacity to suspend more sediment from the bed and this sediment is associated with the decreasing ripple steepness.

2.3.2 Velocity structure

An important difference in the velocity structure between the 1% and 13% sand fraction experiments is the wave boundary layer (WBL) thickness. Velocity profiles and WBL thicknesses averaged for all runs with low, medium, and high Re_Δ at phase $\phi \approx \pi/2$ are shown in Figure 2.3a - 2.3d. For the velocity profiles, we have normalized the vertical coordinate z by the Stokes boundary layer thickness $\tilde{\Delta}$, which accounts for the variation in WBL thickness due to differences in wave forcing but not bed roughness. The top of the WBL is defined

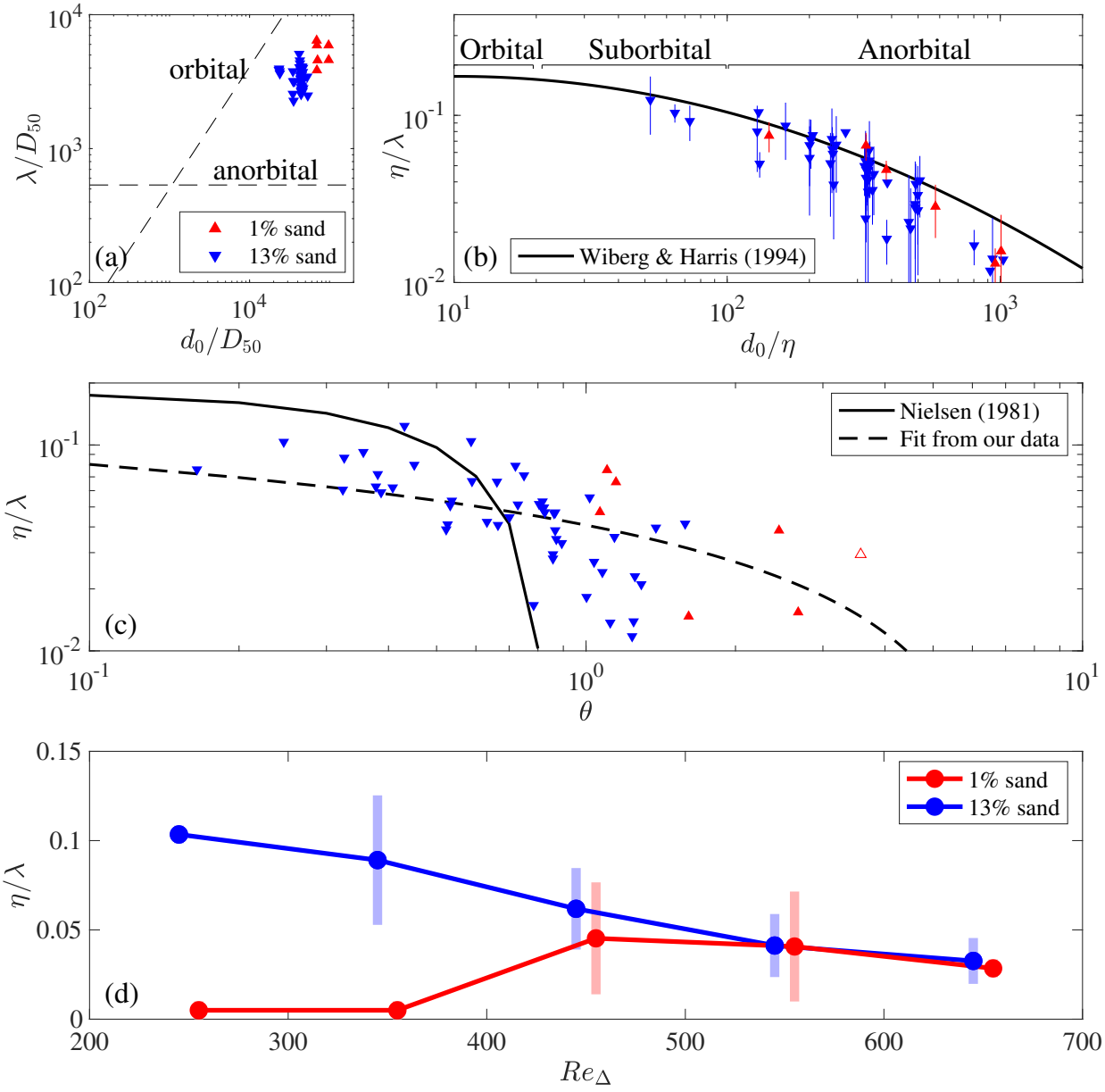

Figure 2.2: (a) Measured ripple wavelength λ, normalized by sediment median grain size D_{50}, as a function of normalized wave orbital diameter d_0; (b) variations of ripple steepness η/λ with d_0 and ripple height η; (c) variations of η/λ with Shields parameter θ; (d) variations of η/λ with Re_Δ. The dashed lines in (a) represent the predicted expressions of λ for orbital and anobital ripples from *Wiberg and Harris* (1994). The black solid line in (b) is the predicted expression from *Wiberg and Harris* (1994). The ranges of orbital, suborbital and anorbital ripples are also classified by *Wiberg and Harris* (1994). The solid lines and vertical shaded bars are the fitted ripples steepness and the corresponding standard deviation for 1% and 13% sand experiments. The black solid line in (c) is the model from *Nielsen* (1981), and black dashed line is the fit from our data, which expresses as $\eta/\lambda = 0.238 - 0.197\theta^{0.098}$, and $R^2 = 0.176$.

as the elevation of the maximum velocity in the corresponding phase. In most of the Re_Δ ranges of our experiments, the averaged velocity profiles in the 1% sand experiments and the rough wall experiments at $\phi \approx \pi/2$ are similar. The WBL thickness in the 13% sand experiments, however, is significantly thicker compared to the 1% sand and rough wall experiments (Figure 2.3a). For example, the WBL thickness in the 13% sand fraction experiments is about 2-3 times that of the 1% sand experiments at the phase $\phi \approx \pi/2$ (Figure 2.3b). This is presumably due to the ripple formation. With the decrease of ripple steepness, the WBL position of 13% sand experiments decreases as Re_Δ increases. For $600 \leq Re_\Delta \leq 700$, the WBL thickness of 13% sand experiments drops to a similar magnitude compared to the 1% sand experiments and the rough wall experiments (Figure 2.3d).

The maximum boundary layer thickness δ_m is used as the characteristic boundary layer thickness in this chapter. δ_m in the 13% sand experiments is greater than that in the 1% sand experiments when Re_Δ is less than ~ 650; but δ_m drops significantly when $Re_\Delta > 700$ (Figure 2.3d). The WBL thickness of the 1% sand experiments increases with Re_Δ until $Re_\Delta > 600$, after which the maximum boundary layer thickness remains relatively constant at ~ 2 cm. This differs from the monotonically increasing boundary layer thickness in the rough wall experiments throughout the Re_Δ range. Despite the fact that ripples do not form in the 1% sand experiments for $Re_\Delta < 400$, a slightly greater WBL thickness is observed in the 1% sand experiments compared to the rough wall experiments, presumably due to the fact that the bed is not perfectly planar initially.

Boundary layer thicknesses for the three different bed settings are mostly greater than the laminar Stokes boundary layer thickness $\tilde{\Delta}$ (Figure 2.3e), confirming that the boundary layers are turbulent in almost all runs. The WBL thickness of the rough wall experiments for $Re_\Delta < 300$ is similar to the Stokes boundary layer thickness, which suggests that the flow might be laminar in this case (Figure 2.3e). The predicted maximum boundary layer thickness based on *Grant and Madsen* (1986), $\delta_{\mathrm{T}} = 2\kappa u_*/\omega$, has a similar trend to that observed in δ_m (Figure 2.3f). For this calculation we used the measured bedform parameters to estimate the bed roughness $k_s = 30\eta^2/\lambda$ (*Wiberg and Harris*, 1994), and $k_s = 3D_{50}$

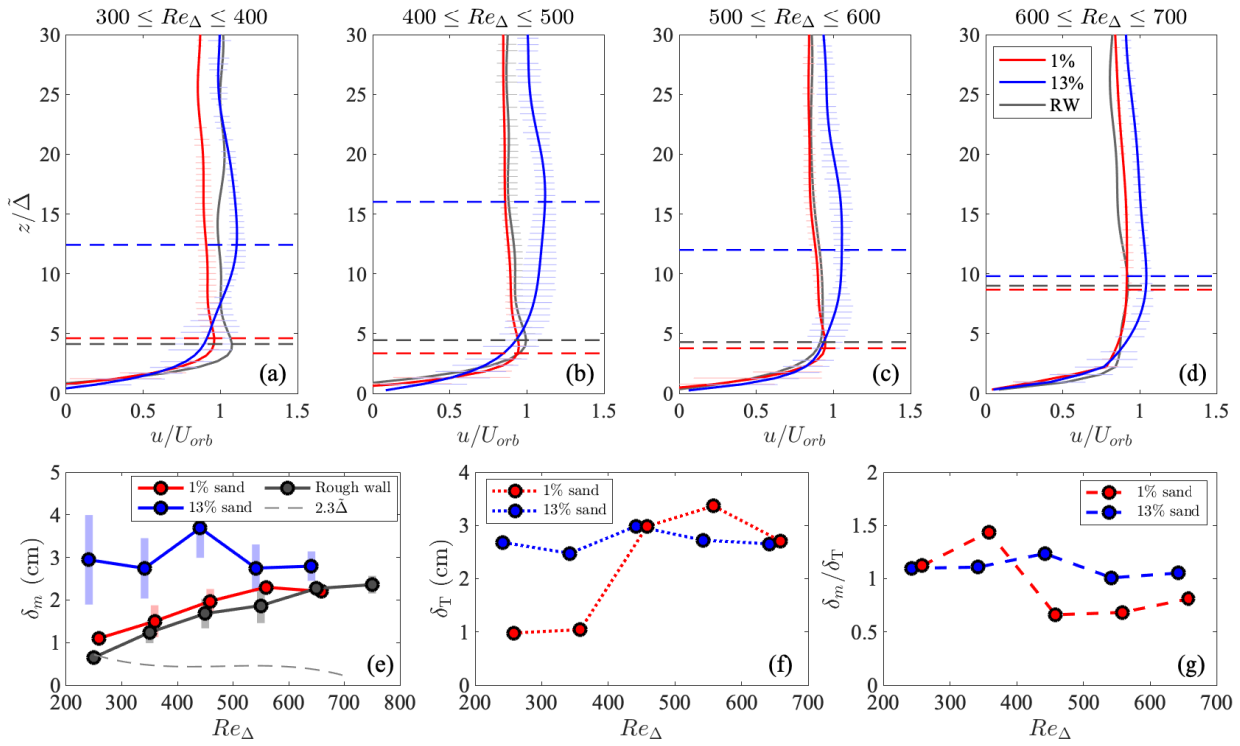

Figure 2.3: (a - d) Averaged velocity profiles at current phase $\phi \approx \pi/2$ within different Re_Δ ranges for rough wall, 1% and 13% sediment bed runs. z is normalized by the Stokes boundary layer thickness $\tilde{\Delta}$. The plotted profiles are fitted from each $0.5\tilde{\Delta}$ vertical bin-averaged data of the corresponding Re_Δ range runs. For 13% sand experiments, we include the data from *Hooshmand et al.* (2015) as well. The red, blue, and gray solid lines represent the 1% sand, the 13% sand,, and the rough wall experiments, respectively. The dash lines represent the corresponding boundary layer positions at $\phi \approx \pi/2$ for the 1% sand, 13% sand and the rough wall experiments. (e) Comparison of maximum wave boundary layer thicknesses. Dots represent the bin-averaged value and shaded bars represent the standard deviation within the corresponding Re_Δ range bins. $2.3\tilde{\Delta}$ represents the maximum Stokes boundary layer thickness, using half of the total Stokes oscillation range from *Schlichting and Gersten* (2016). The maximum wave boundary layer thickness represents the maximum thickness in a total wave phase, which usually appears around the flow reversal phase ($\phi \approx n\pi$, $n = 0, 1, 2, ...$). (f) Predicted maximum turbulent boundary layer thicknesses $\delta_T = 2\kappa u_*/\omega$ considering ripples based on *Grant and Madsen* (1986). (g) The ratio of the measured turbulent boundary layer thickness and predicted boundary layer thickness.

when there were no ripples. The WBL thickness is much lower for runs with no ripples based on 1% sand experiments with $Re_\Delta < 400$. The ratio $\delta_m/\delta_\mathrm{T}$ is around 1 for the 13% experiments (Figure 2.3g), confirming that δ_T is a generally good prediction of the boundary layer thickness, as long as ripples are considered in the calculation. For the 1% sand experiments, however, $\delta_m/\delta_\mathrm{T} > 1$ for runs in which the roughness is based solely on particle size ($Re_\Delta < 400$). This may be because the initial bed condition is not completely planar and there is an effective roughness that exceeds the particle size roughness being used. This is also shown in Figure 2.3e; δ_m for 1% sand is somewhat higher than δ_m for the rough wall experiments for $Re_\Delta < 400$. For $Re_\Delta > 400$ in the 1% sand experiments, $\delta_m/\delta_\mathrm{T} < 1$, which implies that the measured ripples might be more unstable or might have a more three-dimensional structure instead of the assumed two-dimensional ripple structure.

2.3.3 Sediment concentration

Suspended sediment concentration profiles in the 1% sand and 13% sand experiments have different trends as wave energy increases (Figure 2.4a). Under low Re_Δ conditions, the near-bed concentrations in the 13% sand fraction experiments are slightly greater than those in the 1% sand fraction experiments (Figure 2.4b). This is presumably due to ripple formation in the 13% sand bed which introduces more turbulence and leads to relatively more sediment in suspension. As wave forcing increases, however, the near-bed sediment concentration in the 1% sand experiments becomes greater compared to the 13% sand experiments (Figure 2.4b). The initiation of WSGFs requires energetic wave forcing to generate a high concentration layer near the bed. In our experiments, the weakest wave forcing in which a high concentration layer formed was around $Re_\Delta \approx 500 - 600$ in both 1% sand and 13% sand experiments, if we set $C_{NB} = 10$ g L^{-1} as the threshold of a high concentration layer (*Traykovski et al.*, 2007). However, the suspended sediment concentration of 1% sand experiments is much greater than that of 13% sand experiments for $Re_\Delta > 500$. The near-bed concentration gradient, shown in Figure 2.4c, is also higher in the 1% sand experiments when $Re_\Delta > 500$. Plotting the concentration and concentration gradient in terms of the bed

roughness Reynolds number $Re_* = u_* k_s/\nu$ is also instructive. As will be shown in Section 2.3.4, boundary layer turbulence increases dramatically for Re_* greater than a threshold value of approximately 5, suggesting that this demarcates the transition to a hydraulically rough bed. The results in Figure 2.4d and 2.4e show that this transition also results in an increase in near-bed concentration and concentration gradient. The average concentration for runs in the rough regime ($Re_* > 5$) is approximately one order of magnitude higher than those in the smooth regime, although there is a lot of scatter in the concentration values in the rough regime. The 13% runs all fall in the rough regime, whereas the 1% runs fall in both. In both cases, the increase of the bed roughness is primarily due to ripple formation, thus we observe that ripple formation is associated with increased sediment suspension.

In our experiments, the sediment concentration profile is similar to what was observed by *Hooshmand et al.* (2015) (Figure 2.4a), where the near-bed sediment profile does not display the near-uniform concentration observed in some field observations (e.g. *Scully et al.*, 2002). Under the above definition, there is no obvious lutocline capping a high concentration layer in our experiments, though the near-bed concentrations are sufficient to induce downslope flows. From the concentration profiles at high Re_Δ in Figure 2.4a, $6 - 8$ cm seems to be a good estimate of the height at which concentrations are significantly reduced and a more well-mixed profile prevails. If we assume this is the lutocline, then the high concentration layer thickness is about 2 - 3 times the boundary layer thickness, which is consistent with the observations by *Traykovski et al.* (2007).

2.3.4 Turbulence

In Figure 2.5a - 2.5e we compare the near-bed turbulence in the 1%, 13%, and rough wall experiments as a function of Re_Δ. The turbulence is quantified in terms of TKE, RSS, P, and ϵ, which are defined in Section 2.2.6.

Turbulent kinetic energy (Figure 2.5a) displayed varying trends in the different bed setting experiments. For the rough wall experiments, the boundary layer averaged TKE increased monotonically with Re_Δ up to a maximum of 17 cm^2/s^2. For the 13% sand fraction experi-

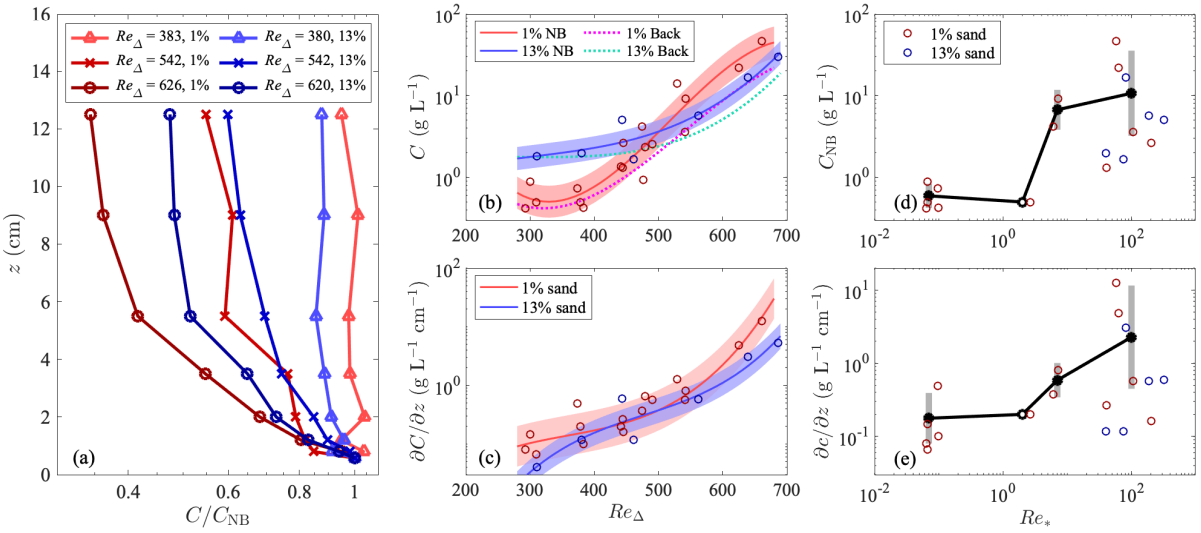

Figure 2.4: (a) Concentration profiles relative to the near-bed concentration C_{NB} for low, medium, and high Re_Δ for 1% and 13% sand fraction experiments. Concentrations were measured with siphon samples. (b) Variations of quasi-steady near-bed concentrations with Re_Δ (solid line, background concentrations not removed) and fitted background concentrations measured at 50 cmab (dotted line). (c) Variations of near-bed concentration gradients with Re_Δ. For (b) and (c), the observed data are shown as open circles, the lines are fit using spline fit and the shaded areas are the standard deviations. (d) and (e) Variations of near-bed concentration and concentration gradient, respectively, with the bed roughness Reynolds number $Re_* = u_* k_s/\nu$. The black line is the bin-averaged value for both 1% and 13% sand fraction, and the gray band is the standard deviation.

ments, TKE remains relatively constant around 5 cm^2/s^2 as Re_Δ increases. For the 1% sand fraction experiments, however, the trend deviates from both the 13% sand fraction runs and the rough wall runs. For $Re_\Delta < 500$, the TKE of the 1% sand runs is low and increases with Re_Δ, approximately matching the values from the rough wall experiments. For $Re_\Delta > 500$, the TKE of the 1% sand runs remains relatively constant, similar to the values in the 13% sand runs. The elevated TKE was observed in the 13% sand runs in the range of $Re_\Delta < 500$ due to the presence of ripples documented in Section 2.3.1, while the 1% sand runs show a similar trend to the rough wall experiments due to the lack of formation of ripples; TKE remains constant for both 1% sand runs and 13% sand runs in the range of $Re_\Delta > 500$, and both are lower than that in the rough wall experiments. Comparison with the elevated TKE observed at high Re_Δ in the rough wall experiments suggests that turbulence is suppressed in both 1% and 13% sand runs.

Similar to the trends observed in TKE, The Reynolds shear stress (RSS) in 13% sand fraction experiments is elevated for $Re_\Delta < 500$, compared with the 1% sand and rough wall runs. RSS is relatively constant at ~ 1.4 cm^2 s^{-2} when $Re_\Delta > 500$. In contrast, a monotonically increasing trend of RSS is observed in the rough wall experiments. In the 1% sand fraction experiments, RSS also increases as Re_Δ increases.

Production (P) is elevated in the 13% sand experiments relative to the 1% sand and the rough wall experiments for $Re_\Delta < 500$, reflecting additional turbulence production from ripples. This difference vanishes as the ripple size decreases for $500 < Re_\Delta < 600$ (Figure 2.5c). The magnitude of P for the 13% and 1% sand fraction experiments is lower than that of rough wall experiments for $Re_\Delta > 600$, indicating that less turbulence is produced under high wave energy.

The turbulent dissipation rate (ϵ) in the rough wall experiments increases monotonically with Re_Δ, coinciding with TKE and P (Figure 2.5d). For both 1% sand and 13% sand experiments, ϵ increases as Re_Δ increases under $Re_\Delta < 500$. ϵ for 1% sand and rough wall experiments is similar, which is lower than ϵ for 13% sand. The ripple-induced turbulence enhancement observed for the 13% sand experiments in TKE, RSS, and P is much less appar-

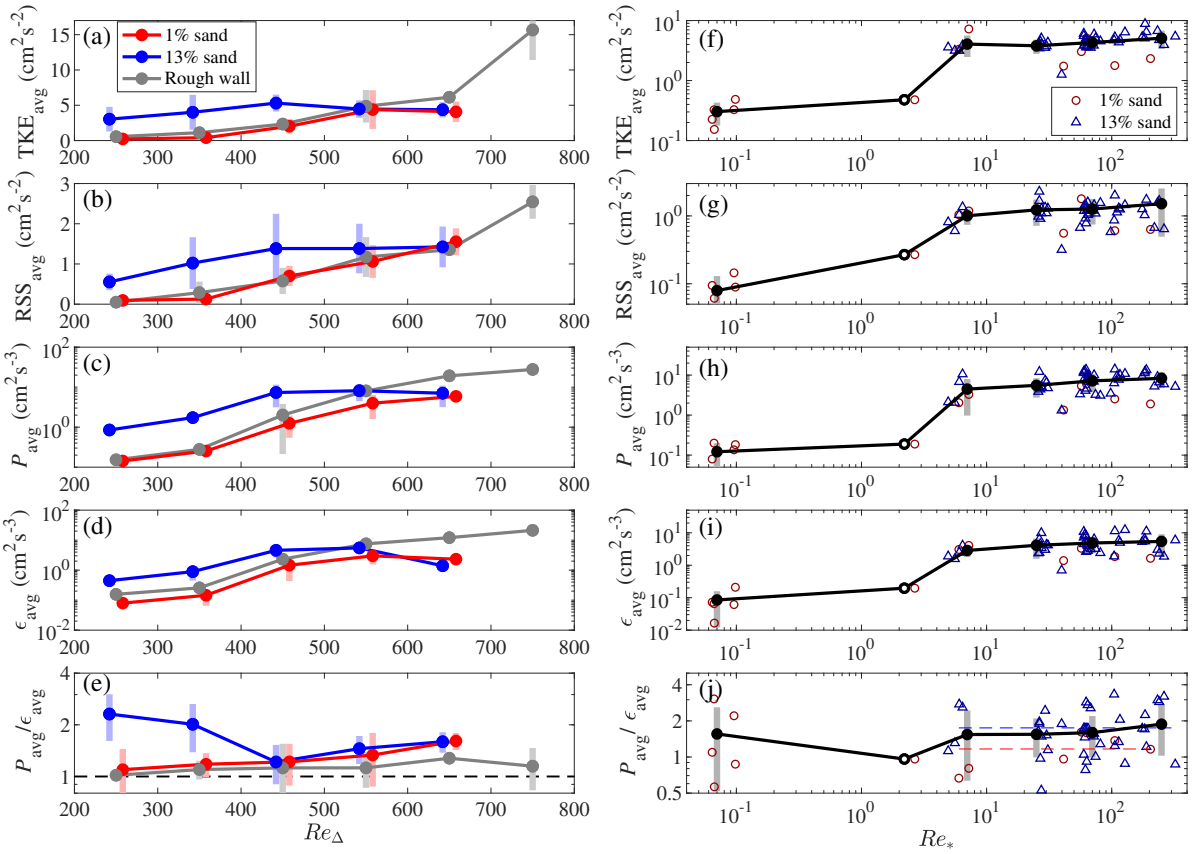

Figure 2.5: Variations of (a, f) turbulent kinetic energy (TKE), (b, g) Reynolds shear stress (RSS), (c, h) TKE production (P), (d, i) TKE dissipation rate (ϵ) and (e, j) ratio of production to dissipation rate with Re_Δ (a-e) and the roughness Reynolds number Re_* (f-j) for the rough wall, 1% sand and 13% sand experiments. Phase-averaged Reynolds stress is defined as the absolute value of the mean Reynolds stress in the wave boundary over the wave period. TKE and RSS are the averaged values inside the wave boundary layer of the total phase-averaged profiles; P and ϵ are the averaged values inside the maximum WBL thickness of the total wave phase. The shaded bar around each point represents the standard deviation of each Re_Δ range bin. In (f-j), the bin-averaged (black) lines are averaged for both 1% and 13% sand experiments. The open black circles indicate that there is only one data point in the bin. Blue and red dashed lines represent the averaged P/ϵ for the 1% and 13% sand experiments when the bed is in rough-smooth transition and fully-rough mode according to *Pedocchi and García* (2009a).

ent for ϵ. For $Re_\Delta > 500$, ϵ remains relatively constant for both sediment bed experiments, in contrast to the increasing trend observed in the rough wall experiments. Under high Re_Δ, ϵ is 3 - 10 times lower for the sediment bed experiments than the rough wall experiments.

The total TKE balance is expressed in equation (2.2). As discussed in Section 2.2.6, it is difficult to accurately calculate transport flux and buoyancy flux. Integrated over the entire water column and in the absence of stratification, the production should be balanced with the dissipation rate (e.g. *Lamb et al.*, 2004). In Figure 2.5e we compare the maximum WBL-averaged ratio of P/ϵ, and interpret deviations from this balance (i.e. P/ϵ not equal to 1) as evidence of the importance of the unresolved terms in the TKE evolution equation: TKE transport and buoyancy flux terms. For the rough wall experiments, P/ϵ maintains a relatively constant value of unity, which suggests a balance of production and dissipation inside the boundary layer in the absence of stratification. In contrast, P/ϵ is more complex in the sediment experiments. For $Re_\Delta < 400$, ripples do not form in the 1% sand experiments, and hence $P/\epsilon \approx 1$, similar to the rough wall experiments. In this Re_Δ range, P/ϵ of is greater than 2 in the 13% sand experiments, much greater than those of the 1% sand and rough wall experiments. This implies that the formation of ripples enhances turbulence production. Numerical simulation results from *Ozdemir et al.* (2010) show that at the top of the boundary layer the TKE transport term becomes first-order important. So at the top of WBL, the transport term might be of the same order as P and ϵ. For $400 < Re_\Delta < 600$, $P/\epsilon \approx 1$ in both the 1% and 13% sand experiments. Since ripple enhancement effects become less important and the high concentration layer forms, the general stratification starts to suppress the upward transport of turbulence. For $500 < Re_\Delta < 700$, P/ϵ of both the 1% sand and 13% sand experiments are both greater than 1. So in general, P/ϵ increases slightly for $Re_\Delta > 500$ to approximately 1.6 ± 0.2. It exceeds P/ϵ for the rough wall experiments, which have a value of ~ 1.2 for $Re_\Delta > 500$. As described in Section 2.3.3, the near-bed concentration gradient increases substantially around $Re = 500$, suggesting that stratification may influence the WBL turbulence in this regime. Although we cannot measure it directly, we expect that the buoyancy flux becomes important in the TKE balance.

The turbulence results indicate a transition from hydraulically smooth to rough when plotted in terms of $Re_* = u_* k_s/\nu$ (Figure 2.5f - 2.5j). We observe a dramatic increase in WBL turbulence for $Re_* > 5$; the values of TKE, RSS, P and ϵ are all approximately on order of magnitude higher for $Re_* > 5$ compared to $Re_* < 5$. In addition, these quantities maintain a relatively constant value as Re_* increases above 5. As noted in Section 2.3.3, all of the 13% sand experiments lie in the hydraulically rough range ($Re_* > 5$), whereas the 1% experiments lie in the smooth and rough regimes. This split can be explained in terms of ripple formation; ripples formed in all of the 13% experiments and $Re_* > 5$ in all of the 1% experiments for which ripple formed.

2.3.5 Gradient Richardson number

Stratification effects in sediment-stratified flows have the potential to damp turbulence in the near-bed regions (*Lamb et al.*, 2004; *Ozdemir et al.*, 2010). In this section we use a gradient Richardson number to evaluate the relative importance of density stratification and shear. We classify the dynamics of the boundary layer flow in terms of a critical value of the gradient Richardson number, $Ri_{gc} = 0.25$; sediment-induced stratification is expected to be important only in regions where $Ri_g > Ri_{gc}$. Note that the use of Ri_g as a stability criterion in sediment-stratified flows is not well-validated, though there is plenty of precedent for its use (e.g. *Ozdemir et al.*, 2010). The aspects of its applicability are discussed in more detail in Section 2.4.3 and Appendix A.

In Figure 2.6 we compare Ri_g profiles for 1% sand and 13% sand experiments over a range of values of Re_Δ. For all of the profiles, Ri_g is lower than Ri_{gc} near the bed, indicating that this region is not critically stratified. Ri_g increases away from the bed and remains approximately constant near a value of Ri_{gc} where the boundary layer shear decreases and stratification becomes important. Stratification is negligible at $z > 3\delta \sim 4\delta$, which is around 10 cm (Figure 2.4a). The fact that the measured profiles approach a similar value of $Ri_g = 0.25$ provides support for our choice of $Ri_g = Ri_{gc}$ and we define a buoyancy length scale L_B as the distance from the bed to the point where this first occurs. The profiles shown

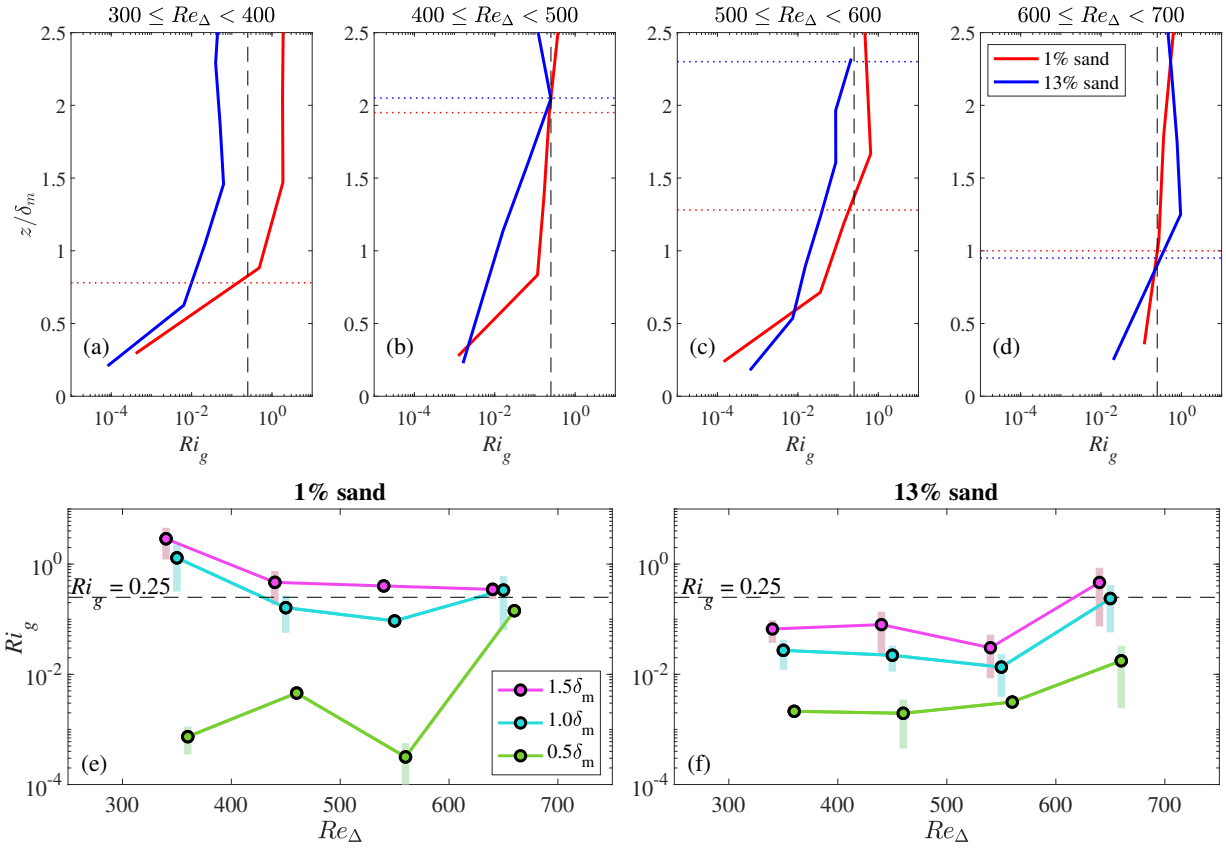

Figure 2.6: (a - d) Characteristic Ri_g profiles of different Re_Δ range bins. The gray dashed lines represent $Ri_g = 0.25$. Dotted lines represent positions where Ri_g reaches a critical value, which is also the height of defined buoyancy length scale L_B (see Section 2.4.3). (e - f) Variations of bin-averaged Ri_g with Re_Δ at different vertical positions relative to the maximum WBL thickness (δ_m) above the bed for 1% and 13% sand fraction experiments. The shaded bar around each point represents the standard deviation of the corresponding Re_Δ bin.

in Figure 2.6 L_B vary with Re_Δ and also depend on the sand fraction.

Stratification varies in its role at different elevations relative to the wave boundary layer thickness (Figure 2.6d-2.6e). Consistent with the profiles in Figure 2.6 we see that Ri_g is lowest close to the bed (at $z = 0.5\delta_m$) and increases away from the bed (at $z = 1.0\delta_m$ and $z = 1.5\delta_m$). In both the 1% and 13% sand experiments the near-bed Ri_g ($z = 0.5\delta_m$) is significantly below Ri_{gc} for all but the highest Re_Δ, indicating that stratification does not significantly affect most of the boundary layer. This is consistent with the results in section 2.3.4, which showed that $P \approx \epsilon$ in the boundary layer except at high Re_Δ. Ri_g is highest in both the 1% and 13% sand experiments at the greatest Re_Δ. This means that stratification becomes important at high Re_Δ, as a large amount of sediment is suspended from the bed (Figure 2.4b). The highest near-bed Ri_g of the 1% sand experiments ($600 \leq Re_\Delta \leq 700$) reaches 0.1, while that of 13% sand experiments reaches only 0.01. In addition, for the 1% sand experiments, Ri_g at $z = 1.0\delta_m$ and $z = 1.5\delta_m$ reaches a relatively constant value of $Ri_{gc} = 0.25$, indicating that the top of the boundary layer is critically stratified. For 13% sand fraction experiments, however, Ri_g at $z = 1.0\delta_m$ and $z = 1.5\delta_m$ does not reach a critical value except under the highest Re_Δ, indicating a larger weakly-stratified region at low Re_Δ with the enhancement of ripples. The weakly-stratified region is larger than δ_m even though δ_m has already been enhanced. For the highest Re_Δ of both sediment bed experiments, $Ri_g \approx Ri_{gc}$ at the top of the boundary layer ($z = 1.0\delta_m$ and $z = 1.5\delta_m$).

2.4 Discussion

The overall purpose of understanding the detailed dynamics of WSGF is to elucidate the key factors that govern the velocity, turbulence, and suspended sediment concentration structure, and therefore to inform the development of accurate across-shelf sediment transport models.

2.4.1 Lutocline formation in mixed mud-sand suspensions

High concentration layers in many field observations exhibit a strong a lutocline, defined as a step-change of suspended sediment concentration above the seabed (e.g. *Traykovski*

et al., 2000; *Hale and Ogston*, 2015). Above the lutocline the concentration is very low and the gravitational sediment flux is minimal; below the lutocline the concentration is high and relatively uniform. The concentration profile with a sharp lutocline structure has been assumed in some models for WSGF transport, where the entire high concentration layer is assumed to be critically stratified, i.e., a bulk Richardson number is used inside the layer $Ri_b = 0.25$ to close the model (e.g. *Wright et al.*, 2001; *Scully et al.*, 2002). However, some field observations have found no sharp lutocline above a high concentration layer, and instead define the lutocline as the location of maximum vertical concentration gradient at some distance above the seabed (*Traykovski et al.*, 2007). When near-bed high concentration layers formed in our experiments ($Re_\Delta > 500$), the concentration profiles were approximately exponential (Figure 2.4) and no obvious lutocline was found, similar to profiles observed in *Hooshmand et al.* (2015). The sediments used in our experiments are made up of crushed silicious particles, and so sediment cohesiveness is low compared to natural silt and clay-sized sediment in shelf environments. Therefore, we hypothesize that fine-grained sediment properties might be controlling factors in lutocline formation. For natural sediment, greater cohesiveness enhances the stability of sediment suspension in addition to enhancing hindered settling effects. Thus, a stronger lutocline or a denser fluid-sediment layer that has a nearly well-mixed concentration occurs in nature (e.g. *Scully et al.*, 2002).

In suspensions that include a significant amount of sand, near-bed concentration gradients may also form without a clear lutocline. By using the data from *Lamb and Parsons* (2005), *Hooshmand et al.* (2015) discussed the increase in near-bed sand fraction at high Re_Δ. From Figure 2.4, 1% sand fraction experiments have higher near-bed concentrations and concentration gradients than the 13% experiments under the same wave forcing conditions, implying that the near-bed concentration is a function of the bed sand fraction. The finer sediment mixture in the bed presumably leads to a higher bed erodibility, where more sediment is suspended. Together these results suggest that the suspension of sand from the bed in mixed grain-size sediment is critical to the formation of high concentration layers.

2.4.2 Dynamical regime transition

The dominant factors influencing the structure of the WSGF layer in our experiments include bedform influences and density stratification, both of which vary across our parameter space. Trends in these factors are consistent with the regime transition presented in *Hooshmand et al.* (2015), who found that $Re_\Delta \approx 450$ divides low and high energy regimes. In our experiments, which include sand fraction variation, these two regimes can also be differentiated based on Re_Δ and the transitional zone is found to lie between 450-550 (Figure 2.7). In the low energy regime ($Re_\Delta < 500$, which corresponds to $U_{orb} < 30$ cm s^{-1}), the sand fraction influences the dynamics primarily through the evolution of bedforms; the formation of ripples in the 13% sand experiments enhances the turbulence, resulting in significantly higher TKE than in the 1% sand experiments (Figure 2.7a). No ripples are observed in the 1% sand experiments in the low energy regime. For all of the experiments in the low energy regime, the near-bed sediment concentration and concentration gradient are relatively low and near-constant with respect to Re_Δ, suggesting that sediment-induced stratification is negligible (Figure 2.7b). In the transitional zone ($450 < Re_\Delta < 550$), both the onset of ripple formation in the 1% sand experiments and the onset of significant near-bed suspension contribute to the dynamics.

In the high energy regime, TKE is relatively constant with respect to Re_Δ in both the 1% and 13% sand experiments and is lower than in the rough wall experiments (Figure 2.5a). At these settings, we also observe that a high concentration layer forms near the bed and the vertical sediment concentration gradient increases dramatically relative to the low energy regime (Figure 2.4). In the 13% sand fraction case we continue to observe bed ripples but their amplitude and steepness decrease. The fact that TKE remains relatively constant at high Re_Δ in the 13% case is likely explained by a joint decrease in bed roughness and an increase in sediment-induced stratification. In the 1% experiments, the near-bed sediment concentration gradient is approximately twice as large as in the 13% experiments (Figure 2.4c). Lacking significant sand, the finer sediment mixture does not generate an armor layer

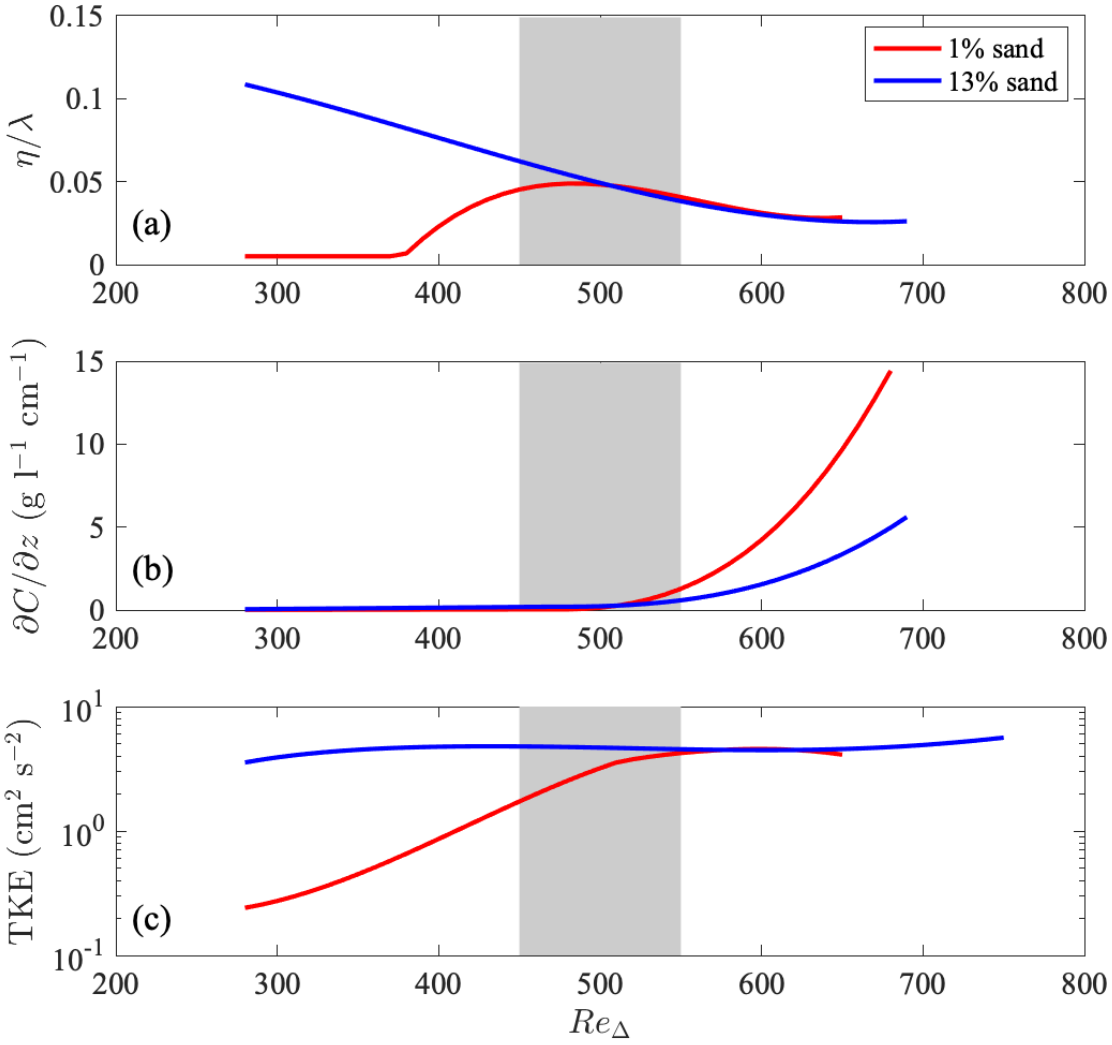

Figure 2.7: Summarized comparison of key parameters influencing the dynamics of wave-supported gravity flows for 1% and 13% sand experiments. Each panel presents the fit to the data shown previously: (a) Ripple steepness (η/λ); (b) near-bed sediment concentration gradient ($\partial C/\partial z$); (c) turbulent kinetic energy (TKE). The gray region indicates the transitional zone between two regimes.

like the 13% sand bed and erosion rates are much higher. This is corroborated by the rate of bed erosion (not shown), which is higher in the 1% sand experiments. Although small ripples are still observed in the 1% sand experiments at high Re_Δ, the high concentration gradient (Figure 2.4c) and Ri_g (Figure 2.6d-2.6e) suggest that stratification plays a greater role in suppressing TKE.

We observe transitions in the WBL thickness in the transitional zone; δ_m in the 13% experiments is reduced in the high energy regime, and the increasing trend in δ_m for the 1% experiments is arrested (Figure 2.3e). *Lamb et al.* (2004), *Ozdemir et al.* (2010) and *Hooshmand et al.* (2015) all observed similar reductions in WBL thickness and suggest that the reduction is due to sediment-induced stratification.

The boundary layer thicknesses of the 1% sand, 13% sand, and the rough wall experiments are almost all greater than the laminar boundary layer thickness ($\tilde{\Delta}$) (Figure 2.3e), reflecting that an intermittently to fully turbulent boundary layer formed in our experiments. δ_m was approximately equal to $\tilde{\Delta}$ for $Re_\Delta \approx 250$ in the rough wall experiments, suggesting that the flow may be laminar in this case. *Ozdemir et al.* (2014) used a numerical model to investigate turbulence in oscillatory boundary layer flow. They described the flow in four regimes: laminar, disturbed laminar, intermittently turbulent, and fully turbulent regimes. It is informative to consider here whether those regimes are observed in our experiments. When no ripples formed, the bed in the 1% sand experiments is expected to behave as a hydraulically smooth bed since $d_{50} << 500$ μm, which is the threshold for a rough bed (*Pedocchi and García*, 2009b). However, as noted in Section 2.3.2, small non-uniformities in the initial bed resulted in an effective bed roughness and our observations suggest that this was sufficient to preclude laminar flow even when no ripples were present. According to the definitions in *Ozdemir et al.* (2014), there is some possibility of disturbed laminar flow in the 1% sand experiment under the low energy regime. However, we observe that the WBL thickness is thicker than the rough wall experiments for $Re_\Delta < 400$ (Figure 2.3d), and therefore it is more likely to be an intermittently turbulent boundary layer than a disturbed laminar boundary layer. *Ozdemir et al.* (2010) reached a fully laminarized boundary layer

with a strong stratification in their numerical simulations with $Re_\Delta = 1000$. We did not observe a fully laminarized boundary layer in our parameter space under strong stratification. Since stratification is important in the high Re_Δ regime, in the following section we will discuss the detailed role of vertical stratification.

Our results document a clear threshold dependence on Re_* for boundary layer turbulence parameters (TKE, RSS, P, and ϵ; Figure 2.5f - 2.5i), and the near-bed concentration (Figure 2.4e). Both the turbulence and concentration increase by approximately one order of magnitude when $Re_* > 5$ relative to lower Re_* runs. *Pedocchi and García* (2009a) define three regimes for bed roughness under waves: the flow is hydraulically smooth for $Re_* < 10$, rough turbulent for $Re_* > 200$, and rough-smooth transitional for $10 < Re_* < 200$. Our turbulence results are generally consistent with this characterization, with two possible exceptions. First, we observed a transition to smooth conditions at a slightly lower value of $Re_* \approx 5$. Second, TKE and other turbulence parameters are relatively constant above $Re_* \approx 5$. Although this is in the rough-smooth transition regime according to *Pedocchi and García* (2009a), we observe no change in behavior above $Re_* \approx 5$. Our results are consistent with a fully turbulent regime. The near-bed sediment concentration is also higher on average when the bed is rough ($Re_* > 5$). Since the bed is only in the hydraulically rough regime when ripples are present, we observe that ripple formation and high near-bed sediment concentrations and concentration gradients co-occur when $Re_* > 5$. The average ratio of P/ϵ is 1 - 1.5 (Figure 2.5j), which means the shear production and dissipation are balanced inside the wave boundary layer. However, as the bed becomes rough, averaged P/ϵ for 13% sand experiments is higher than that of 1% sand experiments. Since the 13% sand experiments also have larger ripples, this imbalance is likely the result of excess production over ripples that must be transported out of the boundary layer.

2.4.3 Role of stratification

We observed that vertical stratification reached a critical value ($Ri_g = Ri_{gc}$) in both the 1% and 13% sand experiments, but that the flow was only critically stratified at or above the

top of the wave boundary layer (Section 2.3.5). Additionally, the thickness of the weakly stratified region ($Ri_g < Ri_{gc}$) decreased relative to the boundary layer height for higher Re_Δ (Figure 2.8a). Accordingly, the near-bed region can be divided vertically into two regions: a weakly stratified region with $Ri_g < Ri_{gc}$ and a critically stratified region with $Ri_g \approx Ri_{gc}$. Although we could not accurately determine Ri_f in our experiments, we define a buoyancy length scale L_B similar in concept to the $0.1Ri_f$ scale used by *Chen and Chen* (2018) based on our Ri_g profiles. L_B is the height from the bed to where Ri_g first equals Ri_{gc} (shown as dotted lines in Figure 2.6).

For the 1% sand experiments, the ratio of the maximum WBL thickness to the buoyancy length scale δ_m/L_B is relatively constant at a value between 0.75 to 1 (Figure 2.8a), which indicates that the role of stratification inside the boundary layer is of secondary importance for most wave forcing conditions. However, at and above the boundary layer, stratification is critically important. Therefore, without an apparent ripple-induced enhancement of turbulence, the wave boundary layer thickness becomes a dynamical boundary: inside the boundary layer, though suspended sediment concentration is high, the velocity shear is also very high. Within a few centimeters above the boundary layer, the velocity shear is reduced but the concentration gradient still exists, and a critically stratified region forms.

For the 13% sand experiments, δ_m/L_B is between 0.25 and 0.5 under low Re_Δ, indicating that stratification does not significantly influence the boundary layer dynamics. Analysis in Section 2.3.2 showed that the boundary layer is thick in the low energy 13% sand experiments due to ripple-induced turbulence enhancement and we expect that this also explains why δ_m/L_B is much lower than in the 1% sand experiments. δ_m/L_B increases with increasing Re_Δ for the 13% sand experiments meaning that the thickness of the weakly stratified region decreases, presumably due to the decrease of ripple steepness. In both the 1% and 13% sand experiments, $\delta_m/L_B \approx 1$ under the highest wave forcing, which means that the weakly stratified region is totally contained within the wave boundary layer and the boundary layer has transitioned to strongly stratified dynamics.

The framework of stratification effects discussed above is based on a definition of critical

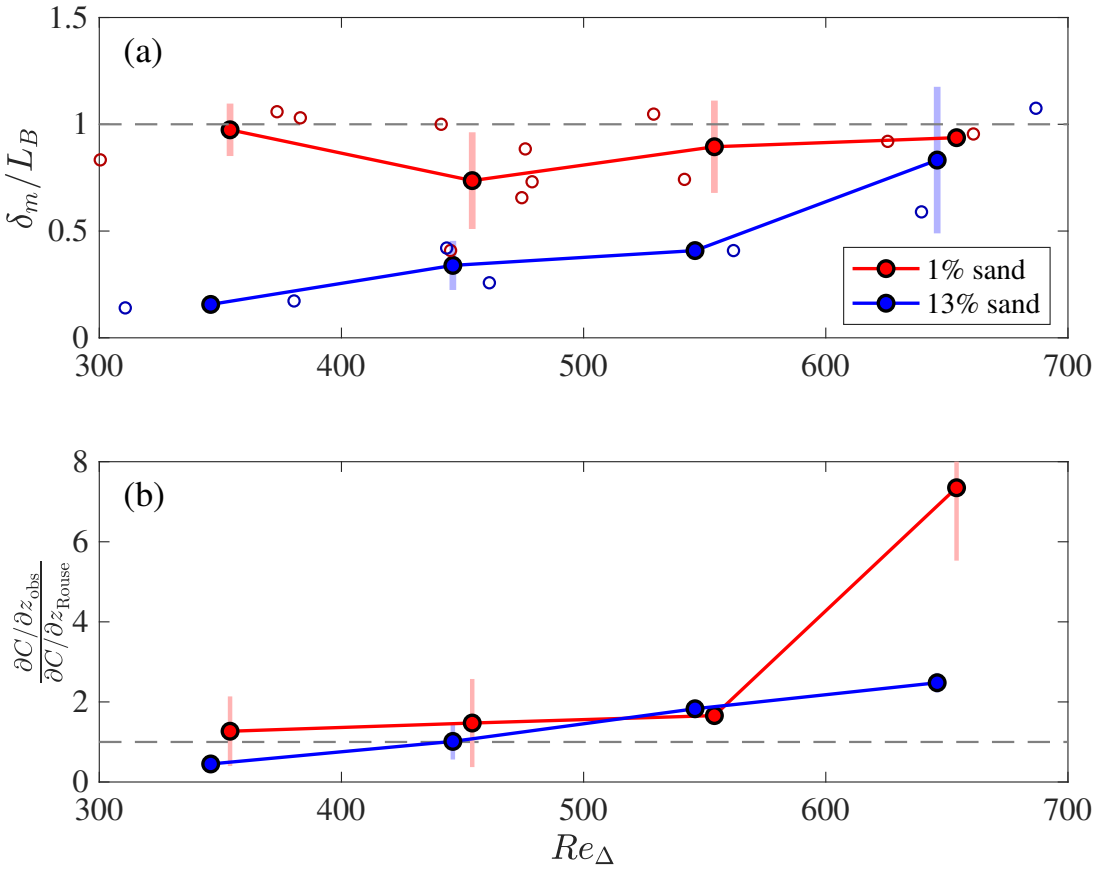

Figure 2.8: (a) Ratio of the maximum wave boundary layer thickness δ_m to the buoyancy length scale L_B. Filled dots represent the averaged data within each Re_Δ range bin. Circles represent the original data. (b) The ratio of the observed concentration gradient and predicted concentration gradient from Rouse profiles at 1 cmab. In each panel, the black dashed line represents the ratio equal to one. The shaded bar around each filled dot represents the standard deviation of the corresponding bin.

gradient Richardson number (Ri_{gc}). The definition of Ri_g is developed from stability analysis, so we need to make sure the instability at the interface of the strongly sheared area has enough time to grow when using Ri_g. A commonly discussed instability in the ocean is the shear-induced Kelvin-Helmholtz (KH) instability (*Gregg*, 1987; *MacDonald and Chen*, 2012; *Thorpe*, 2005). In Appendix A we estimate KH instability timescales and compare them with the wave period. Our estimates show that wave periods in our experiments (and characteristic of field conditions) are sufficiently long for the growth of KH instabilities, implying that Ri_g is an appropriate metric for describing the onset of turbulence in wave-driven shear flows such as the ones described here. This is also supported by an overall agreement between the Ri_g-based length scale analysis above and the turbulence results in Section 2.3.5, both of which show that the boundary layer is only weakly stratified for $Re_\Delta < 550$.

Our results suggest that the wave boundary layer is often weakly stratified, except in high wave energy conditions. In the absence of stratification, the suspended sediment concentration is expected to follow the Rouse profile, which can be approximated near the bed as $C_z = C_r(z_r/z)^{Ro}$. The Rouse number is defined as $Ro = w_s/\beta\kappa u_*$. To test this, we calculated the near-bed suspended sediment concentration gradient ($\partial C/\partial z_{\text{Rouse}} = C_r Ro/z_r$) at a reference height. The reference height (z_r) and reference concentration (C_r) were evaluated from the most near-bed siphon data. Then $\partial C/\partial z_{\text{Rouse}}$ was compared with the observed concentration gradient ($\partial C/\partial z_{\text{obs}}$) at 1 cmab (Figure 2.8b). Settling velocities w_s, calculated based on the Stokes law using D_{50}, and observed shear velocity were obtained to calculate Ro. Based on our comparison, the ratio of $\partial C/\partial z_{\text{obs}}$ to $\partial C/\partial z_{\text{Rouse}}$ increases as Re_Δ increases, i.e., the observed concentration gradient deviates more from Rouse profiles with increasing Re_Δ. For the 13% sand experiments, concentrations are closer to Rouse profiles than the 1% sand experiments at low Re_Δ. For $Re_\Delta > 600$, the observed gradient in the 1% sand experiments is more than seven times greater than the gradient predicted based on the Rouse profile, suggesting that stratification influences the profile shape. In addition, w_s would also increase as Re_Δ increases, due to the increased sand fraction in suspension with higher wave

energy, and this might also account for the increase of the ratio.

The role of stratification in developing and maintaining a high concentration layer for different sediment bed grain size mixtures is illustrated in Figure 2.9. Overall, the vertically unstratified layer is influenced most by the wave boundary layer thickness and ripple enhancement. Under low wave energy, the formation of bedforms not only enhances the boundary layer thickness but also limits the concentration gradient and causes almost all of the water column to be nearly unstratified; the lack of bedforms results in the boundary layer thickness being a controlling factor on the weakly stratified layer. Under high wave energy, the reduction of ripple steepness minimizes the turbulent enhancement by ripples, but increases sediment suspension and enhances stratification effects, which results in the confinement of the weakly stratified layer within the wave boundary layer. Thus, during a storm event when the wave forcing is strong, the buoyancy length scale L_B should be similar to or thinner than the wave boundary layer thickness.

2.4.4 Implications for modeling WSGF

Analytical models have been developed to predict the cross-shelf sediment transport flux of WSGFs, by balancing the downslope gravitational force with bottom stress due to wave motion. The balance is expressed in the linearized Chezy equation (*Trowbridge and Kineke*, 1994) with revision of the stress term by *Wright et al.* (2001) and *Scully et al.* (2002)

$$B \sin \alpha \approx C_d |u_{max}| u_g \tag{2.9}$$

Here $B = gs \int_0^H c(z)dz$ is the integrated buoyancy, which represents the reduced gravity of WSGF under the water, H is the thickness of the high concentration layer, and $u_{max} = \sqrt{u_{orb}^2 + v_{cur}^2 + u_g^2}$, where v_{cur} and u_g are the ambient current and gravitational velocities, separately. Model closure can be achieved by assuming a critical bulk Richardson number $Ri_{b,cr} = B/u_{max}^2 = 0.25$ inside the WSGF. However, several previous studies have found that values of Ri_{bc} can be between $0.01 - 0.03$, which are much smaller than 0.25 (*Lamb and Parsons*, 2005; *Traykovski et al.*, 2007; *Hsu et al.*, 2009; *Flores et al.*, 2018). Low values of

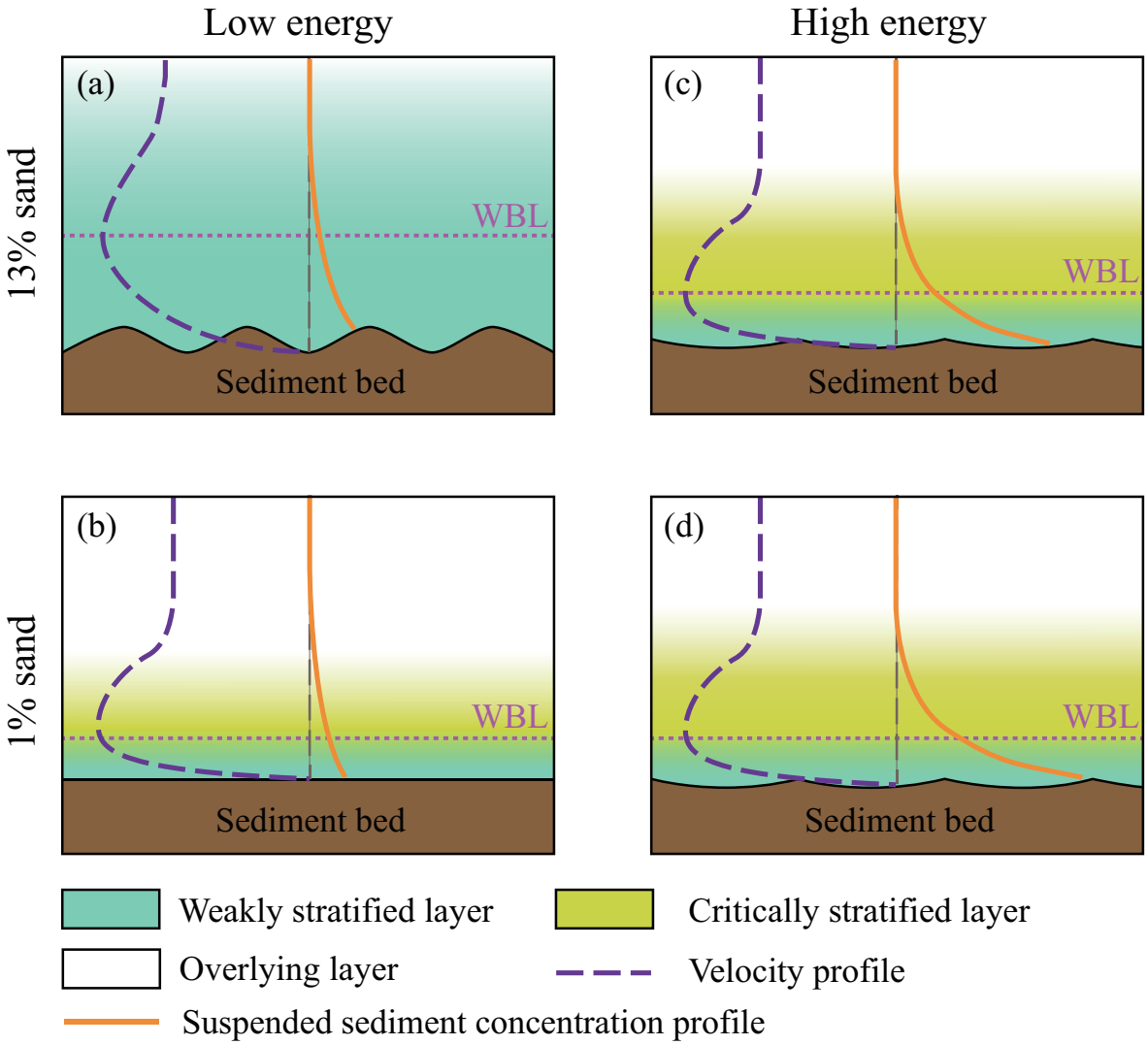

Figure 2.9: Schematic diagrams of critically stratified and weakly stratified layers for 1% and 13% sand fraction experiments. Panel (a) and (b) represents the near-bed conditions for 13% sand and 1% sand fraction experiments under low wave energy; panel (c) and (d) represents the near-bed conditions for 13% sand and 1% sand fraction experiments under high wave energy. The overlying layer represents the region that has both near-zero velocity gradient and near-zero concentration gradient, which can be defined as the free-stream zone.

Ri_{bc} have been attributed to low bed erodibility (*Hsu et al.*, 2009), or transitionally turbulent wave boundary layer flow (*Yue et al.*, 2020).

If the concentration profile is known and thus B can be computed, equation (2.9) can be solved directly for the gravitational velocity without relying on the Ri_{bc} closure: $u_g = gs\int_0^H c(z)dz \cdot \sin\alpha/(C_d u_{max})$. We use this formulation to predict u_g based on measured concentration profiles in our experiments. This approach has an important qualification, however, since our experiments were done with a zero bed slope; the slope α is prescribed in the calculation. The main assumption for this calculation is that suspended sediment concentration profiles in zero-slope conditions are similar to those in gentle slopes, which is expected to be valid as long as wave orbital motion is the dominant driver of the sediment suspension. *Hooshmand* (2016) has shown that the concentration profiles are similar with or without a gentle slope using flume experiments. Recent turbulence-resolving simulations for WSGF also confirm this assumption to be appropriate (*Yue et al.*, 2020). The concentration profiles used in this calculation have had a background concentration removed. We estimate gravitational flux from these concentration profiles as follows. The layer thickness H is approximated as 3 times the wave boundary layer thickness, similar to the discussion in Section 2.3.3. The maximum velocity has been reduced to $u_{max} = \sqrt{u_{orb}^2 + u_g^2}$ since there are no ambient currents. The slope is set as 0.005, which is representative of where WSGF has been observed and continental shelf slopes are typical $0.002 - 0.008$ (*Scully et al.*, 2002; *Traykovski et al.*, 2007; *Hale and Ogston*, 2015; *Flores et al.*, 2018)). C_d is initially set as 0.003 (*Scully et al.*, 2002; *Hale and Ogston*, 2015; *Flores et al.*, 2018), and then changed between 0.002-0.005.

The predicted gravitational velocity u_g increases as Re_Δ increases because the suspended load increased (Figure 2.10a). In the low Re_Δ regime, u_g is slightly greater for the 13% than the 1% sand experiments, which is mainly due to the slightly greater sediment suspension due to ripple formation. Under the strongest wave energy conditions, u_g is faster in the 1% than the 13% sand experiments, presumably due to higher bed erodibility in the fine sediment mixture. Based on our experiments, the estimated values of u_g under strong wave conditions

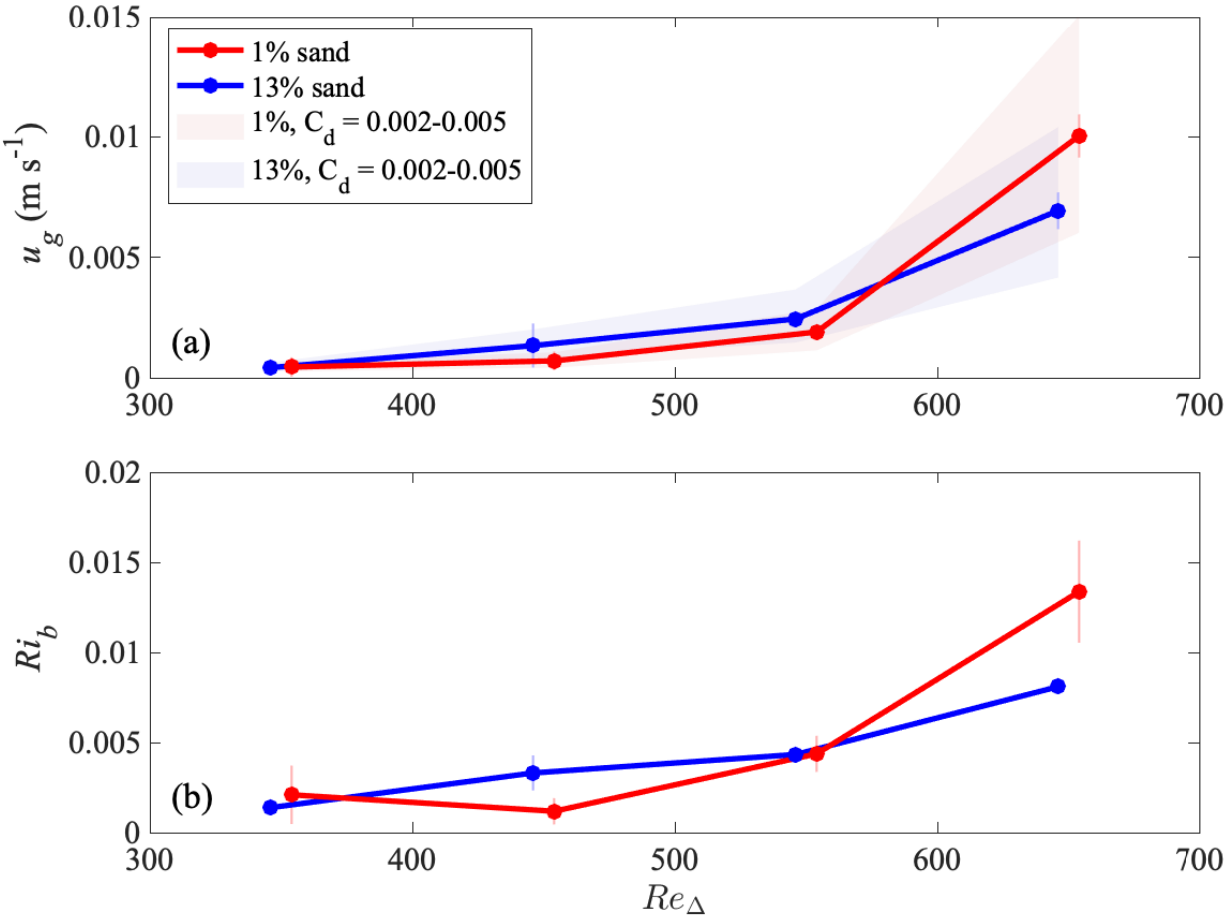

Figure 2.10: (a) Predicted gravitational velocity u_g for 1% sand and 13% sand experiments, with $\sin\alpha = 0.005$ and $C_d = 0.003$. The light red and blue shaded bands represent the range of u_g for $C_d = 0.002 - 0.005$. (b) Estimated bulk Richardson number Ri_b. The lutocline elevation is set as three times the WBL thickness. In each panel, vertical bars around each point represent the standard deviation.

is $\sim$ 1 cm s^{-1}, similar to those observed in the same facility with a sloped bottom from *Hooshmand* (2016). We can also estimate Ri_b from our measured values of B and u^2_{max}; the highest Ri_b is ~ 0.012 and occurs when Re_Δ is high (Figure 2.10b). This value is in the same range as the values of Ri_b observed in the field over a relatively sandy bed by *Flores et al.* (2018). Under similar bed conditions, u_g might be faster than our estimated values since we have used concentration profiles that have removed background concentrations. In natural settings, suspended sediment in the overlying water column may be advected away from the formation zone of a WSGF, resulting in a clearer lutocline and greater density contrast. We have tested the u_g calculation using the concentration without removing background levels, which results in the highest $u_g \approx 3$ cm s^{-1} in the case of $C_d = 0.002$ and $\sin\alpha = 0.005$. The corresponding $Ri_b \approx 0.03$. Thus, the estimates of u_g of order 1 cm s^{-1} are still appropriate.

For large-scale models, it is often difficult to get detailed predictions of suspended sediment concentration as an input to estimate Ri_{bc}. A series of studies parameterize erosion and deposition of the bed as a function of bed stress and concentration, where the suspended sediment concentration profile is estimated using an "active layer" concept to consider the sediment availability. These model results compare well with observations of bed erosion for some storm events (*Harris et al.*, 2005; *Traykovski et al.*, 2007; *Harris et al.*, 2008; *Flores et al.*, 2018). Based on our study, the modes of behavior discussed in Section 2.4.3 might provide an alternative method for estimating the concentration profiles. In particular, modeling may take advantage of the fact that the concentration is expected to follow a Rouse profile within the WBL. Using this concept the concentration profile can be estimated using a near-bed reference concentration C_a. If $a = z_0$, where z_0 is the roughness length, C_a can then be estimated using the expression $C_a = C(z_0) = C_b\gamma_0 S/(1 + \gamma_0 S)$ (*Wiberg and Smith*, 1983). Here $C_b = 1 - \phi$ is the concentration of sediment in the bed, where ϕ is the bed surface porosity. γ_0 is a constant set to represent the bed erodibility, which is usually between 0.002 - 0.003 (*Wiberg and Smith*, 1983; *Traykovski et al.*, 2007). For our measurements, $C(z_0) \approx 1.2 \sim 1.5C_{\mathrm{NB}}$. For the very fine sediment and weak cohesiveness of the crushed silicious sediment used in this study, this value might be higher. $S = \tau/\tau_{cr} - 1$ is the

excess shear stress. Predicted concentration profiles would still need to be adjusted at the top of the WBL, however, where stratification is observed to be important. The approach presented by *Chen and Chen* (2018), which addresses the structure of concentration profiles in unidirectional boundary layers, may be applicable in this case.

The structure of the wave-supported high concentration layers generated in our laboratory experiments differs from that observed from field data collected within and above the wave boundary layer, and this has implications for the modeling of WSGF. Although the sediment used for the flume experiments does not display all the attributes of natural sediment (e.g., flocculation, hindered settling and other particle interactions are limited), in many ways the data from the flume experiments are consistent with observations in sand-rich shelf environments (e.g. *Traykovski et al.*, 2007; *Flores et al.*, 2018). In other previous evaluations of field data (e.g. *Scully et al.*, 2002), Ri is assumed to be vertically uniform and at a critical value throughout the wave boundary layer in these natural sedimentary environments, which is not the case in our flume experiments. The key dynamical difference between the structure observed in our experiments and that inferred when using limited resolution field observations is in the importance of stratification in the near-bed region of the wave boundary layer; this region is only weakly stratified in our experiments, instead of critically stratified. Moreover, the formation of ripples observed in our measurements also provides additional control on the stratification within the wave boundary layer.

2.5 Conclusions

We conducted a series of laboratory experiments in an oscillatory water tunnel using bed sediment mixtures with two different sand fractions (1% and 13%). We compared velocity, turbulence, and suspended sediment concentration in order to understand how the sand fraction on predominantly muddy shelves affects the physical processes in wave-supported gravity flows. The bed sediment sand fraction changes the boundary layer velocity and turbulence structure primarily through the formation of ripples. For 13% sand fraction ripples exist throughout the entire range of the experiments ($250 \leq Re_{\Delta} \leq 700$) and the

ripple steepness decreases as the wave energy increases. For the 1% sand fraction ripples do not form in low wave energy conditions. Ripples begin to form when $Re_\Delta \geq 400$, and have a similar steepness to those in the 13% experiments.

The change of ripple steepness and the influence of sediment-induced stratification divide the flow into two regimes distinguished by Re_Δ, where the transitional zone lies between $450 < Re_\Delta < 550$. In the low energy regime, the presence or absence of ripples is the key factor that influences boundary layer dynamics. Stable ripples formed in the 13% sand experiments that enhanced the near-bed turbulence and increased the wave boundary layer thickness. No ripples formed in 1% sand experiments and as a result, the turbulence intensity was similar to that observed in the rough wall experiments. In the high energy regime, ripples were less steep and sediment-induced density stratification was much greater than in the low energy regime. As a result, stratification is dominant in the dynamics at the highest wave energy. Turbulence intensity does not increase with higher wave energy, presumably because stratification damps the turbulence. The near-bed concentration and concentration gradient are higher in the 1% sand experiments, compared to the 13% sand experiments under similar wave conditions due to greater bed erodibility.

For all Re_Δ the flow is observed to be weakly stratified very near the bed; stratification only becomes important in a region at or above the top of the wave boundary layer. We differentiate between these regions based on a buoyancy length scale L_B, defined as the length from the bed to the height where Ri_g reaches 0.25. For $z < L_B$ the flow is weakly stratified ($Ri_g < 0.25$), and stratification is of secondary importance in the dynamics. For $L_B < z < 2 \sim 3\delta_m$, the flow is critically stratified ($Ri_g \approx 0.25$). Here δ_m represents the maximum wave boundary layer thickness. The sand fraction of the bed modifies these dynamics; higher sand fraction results in ripples in low to moderate wave energy that increase the near-bed turbulence and L_B. In the 1% sand experiments, L_B is similar to the wave boundary layer thickness. For our most energetic runs, the ratio of the boundary layer thickness to the buoyancy length scale $\delta_m/L_{Ri_g} \approx 1$ for both 1% and 13% sand experiments, indicating the transition to strongly stratified dynamics. In general, our results show that

the sand fraction of the bed sediment mixture influences both the turbulence and sediment stratification in the wave boundary layer.

Chapter 3

SAND CONTROL OF SEDIMENT SUSPENSION IN WAVE-SUPPORTED GRAVITY FLOWS

3.1 Introduction

In coastal-shelf systems, some terrestrial fine sediment introduced from rivers is ultimately transported across the continental shelf into the deep ocean. In general, cross-shelf sediment transport is complex and may involve multiple physical processes such as wind-driven flows, internal waves, infragravity phenomena, and buoyant plumes (*Nittrouer and Wright*, 1994), depending on the local weather conditions, hydrodynamics, geographic conditions, and shelf morphologies. Studies over the past two decades have shown that wave-supported gravity flows (WSGF) contribute substantially to the total cross-shelf sediment transport (e.g. *Ogston et al.*, 2000; *Wright et al.*, 2001; *Scully et al.*, 2002; *Traykovski et al.*, 2007). WSGFs are gravity flows for which external shear stress primarily from waves induces sediment suspension on a gentle slope and a high-concentration layer is formed near the seabed. Sediment is then transported downslope due to the negative buoyancy of the high-concentration layer.

The formation of a high-concentration layer (HCL) near the bed is a critical condition for WSGFs. A generally accepted threshold of the near-bed suspended sediment suspension for WSGF formation is $\sim$ 10 g L^{-1} (*Traykovski et al.*, 2007). Based on this threshold, most WSGFs occur during storm events (e.g. *Ogston et al.*, 2000; *Hale and Ogston*, 2015). Therefore, we might predict the initiation and transport of WSGF under certain study areas through the prediction of high sediment suspension if the relationship between the storm intensity and storm frequency is known.

Several existing WSGF models predict sediment concentrations based on the assumption that sediment supply from the bed is unlimited and the sediment concentration is uniform

inside the high-concentration layer (*Trowbridge and Kineke*, 1994; *Scully et al.*, 2002). However, recent observations and laboratory experiments have shown that in some cases vertical concentration profile is exponential and that the sediment suspension is limited by bed erodibility (*Traykovski et al.*, 2007; *Hooshmand et al.*, 2015). To understand the dynamics of WSGFs, control factors on sediment suspension are essential to unravel, and this will allow the improvement of future models on WSGF.

Sediment suspension has a high correlation with flow conditions. *Bagnold* (1954) stated that sediment particles remain in suspension when turbulent eddies have vertical components (w') that exceed the particle settling velocity (w_0). Assuming the vertical velocity component is represented by the vertical turbulence intensity ($\tilde{w}$), the critical value for initiation of suspension can be expressed as $\tilde{w} = [\overline{(w')^2}]^{0.5} \geq w_0$. Bagnold then suggested that the maximum $\tilde{w}$ is of the same order as the bed shear velocity (u_*) based on boundary layer turbulence studies. Therefore, the critical bed shear velocity (u_{*c}) for initiation of suspension is $u_{*c}/w_0 = 1$. Since u_*/w_0 represents the relationship between the sediment property and flow condition, the following studies then tend to use u_*/w_0 as the non-dimensional number to define the criterion for the initiation of suspension. For example, *Engelund* (1965) derived the criterion $u_{*c}/w_0 = 0.25$ based upon a crude stability analysis, where he did not consider the influence of particle size. The most widely used criterion for initiation of suspension is from *Van Rijn* (1984) and can be expressed as:

$$\begin{aligned} u_{*c}/w_0 &= 4/d_* \qquad \text{for } 1 < \mathrm{d}_* < 10 \\ u_{*c}/w_0 &= 0.4 \qquad \text{for } \mathrm{d}_* > 10 \end{aligned} \tag{3.1}$$

where $d_* = [sgd^3/\nu^2]^{1/3}$ is the non-dimensional particle size, d is the actual particle size, g is the gravitational acceleration, ν is the kinematic viscosity, and $s = (\rho_s - \rho_w)/\rho$ is submerged weight of siliceous sediment relative to the water. The formulation of Van Rijn accounts for the influence of particle size on the sediment suspension criterion, especially on fine sediments. Most prior studies, including (*Van Rijn*, 1984), use the mean or median grain size to characterize the initiation of suspension for non-cohesive sediment. Different

suspended sediment grain size characteristics from sand fraction and mud fraction have not been discussed.

Most of the existing literature on WSGF events is based on observations from predominantly muddy environments. But one recent observational study measured WSGF in a predominantly sandy environment and addressed the importance of particle size effects on the dynamics of WSGF (*Flores et al.*, 2018). *Hooshmand et al.* (2015) performed laboratory experiments and stated the potential importance of sand fraction in controlling the dynamics of WSGF. Continuing with this work, *Han et al.* (2021) compared lab experiment results with two different sand fraction sediments and concluded that sand fractions altered the dynamics of WSGF primarily through the formation of ripples. *Lamb and Parsons* (2005) reported that sand fraction in a high-concentration layer increased, and stated that bed winnowing caused the coarser bed surface and thus depressed the thickness of the high-concentration layer. In addition, due to the particle size distribution, some fraction of the sediment distribution will be suspended under certain wave energy, while the coarser fractions have no motion or move as bedload. For example, laboratory experiments by *Liang et al.* (2007) showed fine sediments suspended in plume-like shapes, and the suspension stopped after ripples formed, i.e., when the surface of the bed is coarsened by sands. In natural muddy shelf environments, however, sediment characteristics are more complex than these lab studies and include sediment aggregation and/or biogenic processes, both of which will affect sediment suspension. For the present study, the first step is to understand the role of sand in controlling the suspension, which is an important step towards understanding the dynamics of the wave-supported gravity flows on mud-dominant shelves.

In this chapter, we present experimental results using bed sediment consisting of 1% and 13% sand fractions. Those experiments are used to investigate how the sand component controls sediment suspension. We propose a modified sediment suspension criterion reflecting the role of sand in mud-dominant environments.

3.2 Experimental setup

Sediment bed experiments were performed in an oscillating water tunnel, which has a 5 m long, 1 m high, and 0.2 m wide experimental section (Figure 3.1a). The near sinusoidal oscillatory flows in the experimental section are driven by a vertical piston on one side which produces oscillatory motions with periods of $5 - 15$ s and wave orbital velocities of $15 - 55$ cm s^{-1} in the test section. The horizontal oscillatory motions in the water tunnel were designed to simulate one-dimension fluid motions driven by surface gravity waves as they are typically felt on the seabed of continental shelves.

The sediment we used is U.S. Silica Sil-co-Sil 45 and SIL-CO-SIL 106 crushed silica, which consist of 1% sand fraction and 13% sand fraction, respectively. The detailed grain size distribution is shown in Figure 3.1b. The sediment is weakly cohesive compared to natural sediment in the field of similar grain size, so properties, such as sediment aggregation, are different from natural sediment.

Suspended sediment concentrations (SSC) were measured with an 8-port vertical sediment siphon rake and fiber-optic backscattering sensors (FOBS). The FOBS has 20 bins with 10 mm spacing between the lowermost 10 sensors and progressively wider spacing above, which in total provided a 50 cm SSC profile. The FOBS was calibrated in a mixing tank, and the calibrations showed linear responses for concentrations below 80 g L^{-1}. The sediment siphon rake was placed at eight different vertical locations with a 2 mm spacing of the two lowermost ports and wider spacing above. During the experiments, 50 ml water was siphoned from each port at a relatively constant flow rate. These samples were dried out in a 60°C oven and then weighed to determine the SSC, following the procedure of *Lamb et al.* (2004). Particle sizes were sampled at different vertical positions during each run through the 8-channel siphon rakes and evaluated using a Beckman Coulter LS13-320 Particle Size Analyzer.

X-radiography of the bed and suspension was performed for certain runs just after the run. Scans were collected from the sidewall of the test section using an Ecotron EPX-

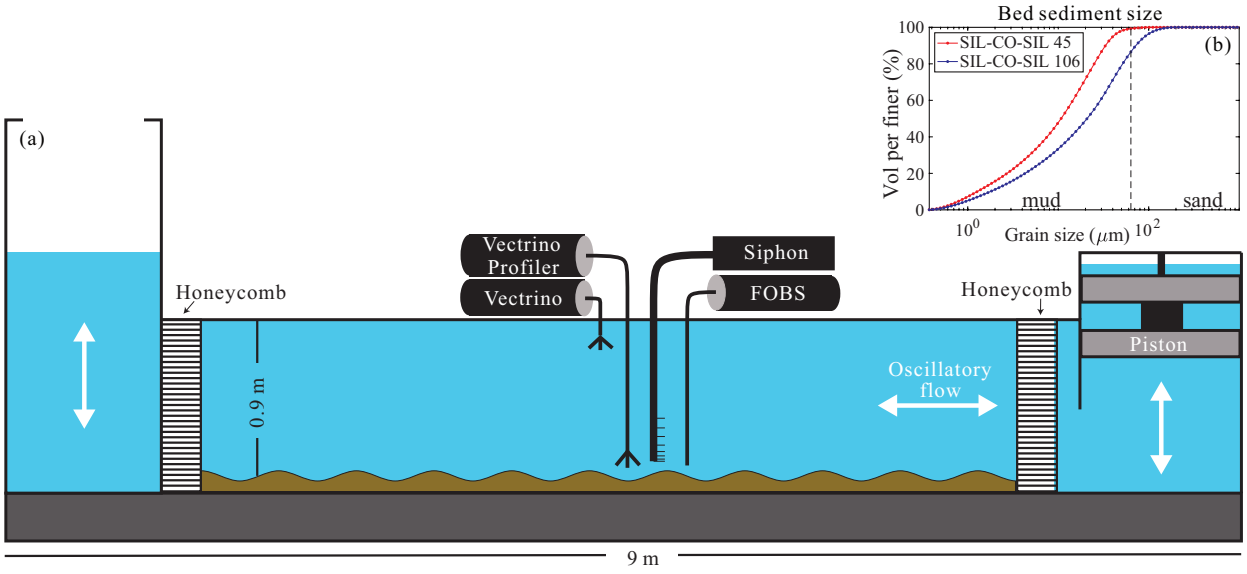

Figure 3.1: (a) Schematic oscillating water tunnel. Oscillatory motion is driven by the piston on the right. The width of the tank in the middle section is 0.2 m. (b) The cumulative bed sediment particle size distribution for 1% sand fraction sediment (SIL-CO-SIL 45) and 13% sand fraction sediment (SIL-CO-SIL 106). The vertical dotted line in panel (b) represents the classification between sand and mud.

F2800 portable veterinary x-ray generator emitting towards waterproofed x-ray film on a thin stainless plate inserted into the sediment bed, approximately 2.5 cm from and parallel to the sidewall.

Velocity and turbulence measurements were performed using a Nortek Vectrino Profiler near the bottom, with a single point Nortek Vectrino sampling at 70 cm above the bed (cmab) to provide a reference phase for velocities. The measured shear velocity was estimated based on the averaged Reynolds stress: $u_* = \left(-\overline{u'w'}\right)^{1/2}$ over the wave boundary layer and the wave period. The predicted shear velocity $u_{*,pred} = \sqrt{f_w/2}U_{orb}$ was calculated based on the wave friction factor f_w, where $f_w = \exp[5.213(k_s/a_b)^{0.194} - 5.977]$ (*Swart*, 1974), a_b is the wave orbital semi-excursion amplitude near the bed, and $k_s = D_{50}$ without considering ripples (*Nikuradse*, 1933). We also estimated of $u_{*,pred}$ considering ripple effects, where $k_s = 27.7\eta(\eta/\lambda)$ (*Grant and Madsen*, 1982). Here η and λ are the measured ripple height and ripple wavelength. The comparison between different estimation of $u_{*,pred}$ will be discussed in Section 3.4.2. Settling velocity was estimated through $w_0 = \sqrt{4(s-1)gd/3C_D}$, where $s = (\rho_s - \rho_w)/\rho_w$ represents the submerged weight of siliceous sediment relative to the water, and C_D represents the drag coefficient. For very fine sediment the law of Stokes was used as $C_D = 24/Re_d$; for the coarser sediment, $C_D = 24/Re_d + 1.5$ (*Engelund and Hansen*, 1967), where $Re_d = w_0 d/\nu$ is the particle Reynolds number. In our paper, the Stokes Reynolds number ($Re_\Delta = U_{orb}\tilde{\Delta}/\nu$) was used to represent the wave intensity, similar to what has been presented in *Hooshmand et al.* (2015) and *Han et al.* (2021).

We define a suspension parameter based on the definition from *Van Rijn* (1984):

$$E^* = \frac{u_*/w_0}{4/d_*} \tag{3.2}$$

where $E^* = 1$ is the threshold of sediment suspension. In the following text, E^*_{50} and E^*_{sand} represent E^* calculated using bed sediment median grain size D_{50} and the bed sediment median grain size of only the sand fraction D_{sand}, respectively.

3.3 Results

3.3.1 Velocity, boundary layer, and Reynolds stress

The velocity and Reynolds stress of four characteristic cases are shown in Figure 3.2. The pseudo-color plots represent the phase-averaged Reynolds stress over a wave period. High Reynolds stress occurs at the near-bed region. The wave boundary layer grows from the start of a wave period and reaches a maximum at flow reversal (phase $\approx \pi$), and then a new boundary layer forms. For $Re_\Delta \approx 380$, the boundary layer thickness for 13% sand experiments is higher than that of 1% sand experiments. The maximum wave boundary layer thickness δ_m for 1% sand experiments is around 1.7 cm, while δ_m for the 13% sand experiments is around 2.4 cm. For $Re_\Delta \approx 630$, the structure of the wave boundary layers in both 1% and 13% sand cases is similar.

The measured shear velocity (u_*) for 13% sand experiments is about $1.5 - 2.5$ times the u_* for 1% sand experiments when $Re_\Delta < 600$ (Figure 3.3). For $Re_\Delta > 600$, u_* for 1% sand and 13% sand experiments are both approximately $1.2 - 1.8$ cm s^{-1}. Similarly, the maximum wave boundary layer thickness δ_m for 13% sand experiments is about $1.5 - 3$ times the δ_m for 13% sand experiments when $Re_\Delta < 600$. When $Re_\Delta > 600$, δ_m for 1% sand and 13% sand experiments are both approximately 2 cm.

3.3.2 Ripple formation

Ripples formed in both 13% sand and 1% sand fraction experiments, and the ripple steepness we observed fit reasonably well with the model from *Wiberg and Harris* (1994), which has been shown in *Han et al.* (2021). All of the ripples observed in the 1% sand fraction experiments are in the anorbital range based on the classification by *Wiberg and Harris* (1994). Ripples observed in the 13% sand experiments are also primarily in the anorbital range, except for the lowest Re_Δ experiments, in which ripples are in the suborbital range. We observed ripple geometry changes with variations in wave forcing, and the ripple steepness trends for the two bed sediment settings were different (Figure 3.4c). For 13% sand fraction,

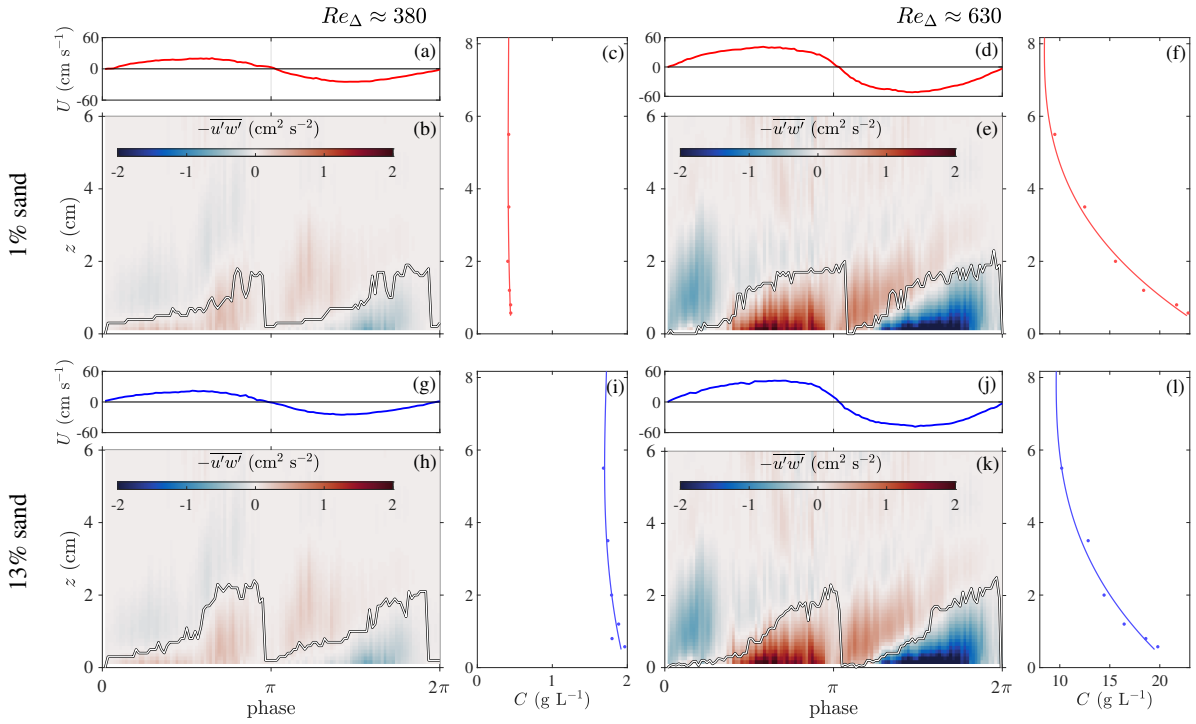

Figure 3.2: Characteristic free-stream velocity phase (U, panel a, d, g, j), phase-averaged Reynolds stress ($-\overline{u'w'}$, panel b e, h ,k), and concentration profiles (C, panel c, f, j, l) for 1% sand and 13% sand fraction experiments under low and high wave energies. The black-white lines in (b, e, h, k) represent the growth of the wave boundary layer inside a wave period.

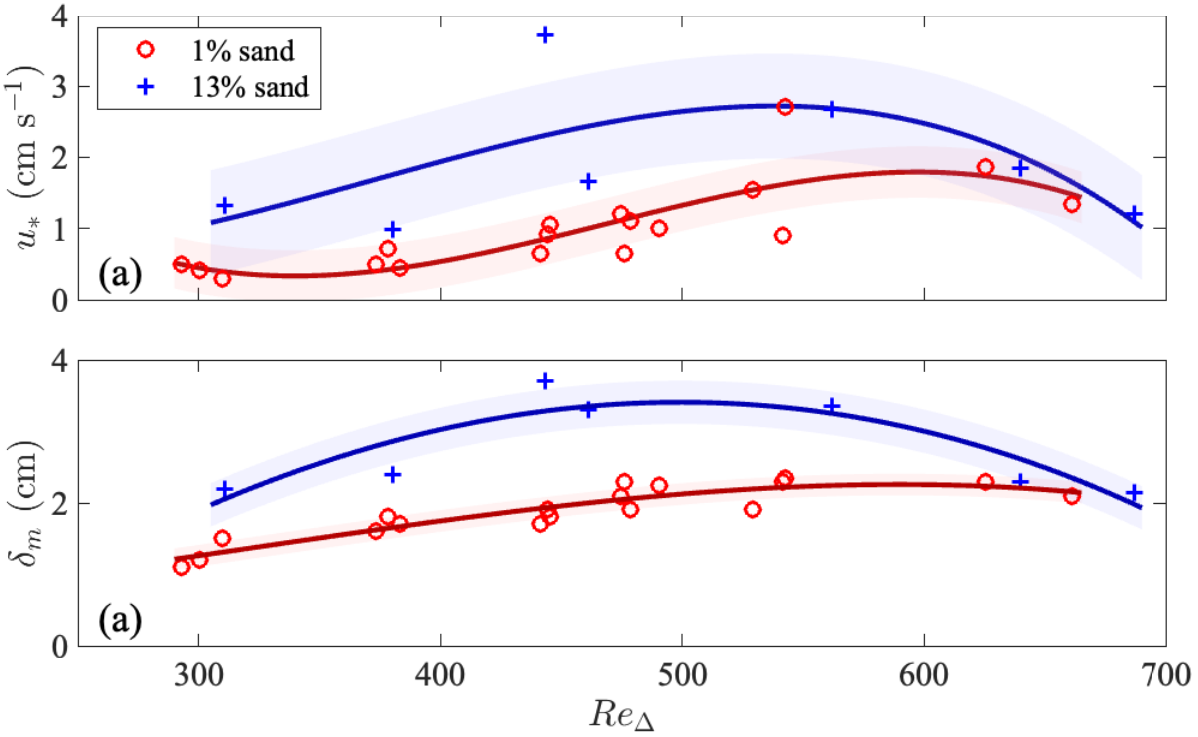

Figure 3.3: Variations of (a) shear velocity (u_*) and (b) maximum wave boundary layer thickness (δ_m) with Stokey Reynolds number (Re_Δ).

ripples form across all of our parameter space and the ripple steepness slightly increases for $380 < Re_\Delta < 480$ and then decreases as Re_Δ increases. From *Hooshmand et al.* (2015), ripples also form when $Re_\Delta < 380$. For 1% sand fraction, ripples start to form only when $Re_\Delta > 380$ and ripple steepness decreases as Re_Δ increases. Under high Re_Δ the ripple steepness for 1% sand becomes statistically similar to that of 13% sand experiments, suggesting a similar condition when most of the sand fraction is suspended or collected at the near-bed region.

3.3.3 Sediment concentration

The near-bed suspended sediment concentration and concentration gradient are shown in Figure 3.4a-3.4b. The initiation of WSGFs needs strong wave forcing to meet the requirement of a high-concentration layer near the bed. In our experiments, the weakest wave forcing in which a high-concentration layer formed was $Re_\Delta \approx 500 - 600$ in both 1% sand and 13% sand experiments, and the Re_Δ for the formation of high-concentration layer for 1% sand is lower than that of 13% sand. In addition, the suspended sediment concentration of 1% sand experiments is much greater than that of 13% sand experiments for high Re_Δ. For example, near-bed concentration of the 1% sand experiment $C \approx 20$ g L^{-1} for $Re_\Delta \approx 600$, where $C \approx 10$ g L^{-1} for the 13% sand experiment. The near-bed concentration gradient (Figure 3.4b), shows a similar trend as the near-bed concentration, which is presumably due to higher bed erodibility with the finer sediment mixture. This result implies that the sediment suspension criteria are different for different sand fractions.

3.3.4 Suspended sediment grain size

Grain size of the suspended sediment can be used to estimate how much of the coarser sediment fraction is in suspension. Figure 3.4d-3.4e show the median particle size (D_{50}) and the volume fraction of sand 1 cm above the bed. Under low wave conditions ($Re_\Delta < 400$), D_{50} is relatively constant; D_{50} of 1% sand experiments is ~ 3.5 μm, and D_{50} of 13% sand is ~ 5.4 μm. Under high wave conditions ($Re_\Delta > 400$), D_{50} for both the 1% and 13% sand

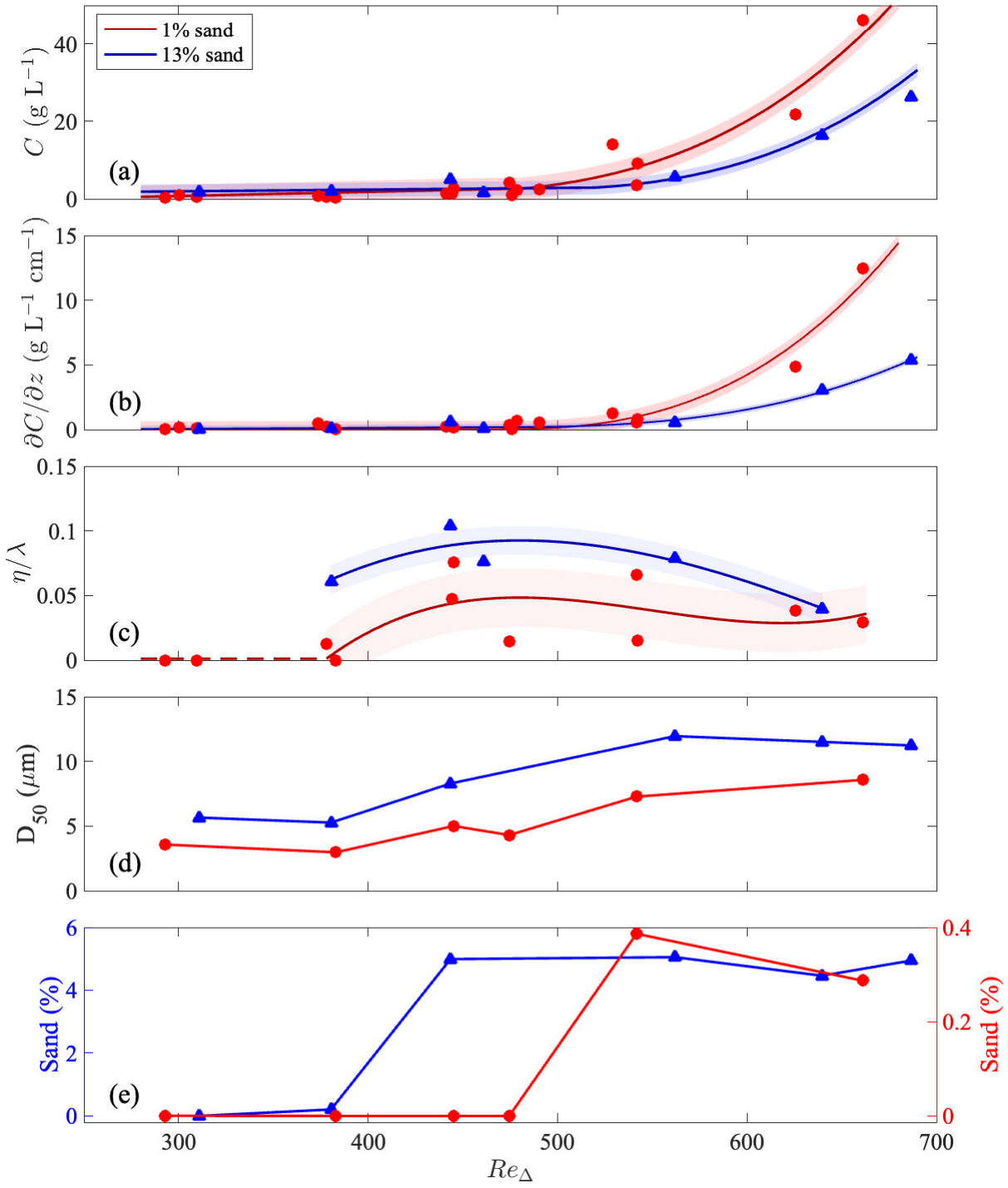

Figure 3.4: Variations of (a) near-bed concentration, (b) near-bed concentration gradient, (c) ripple steepness η/λ, (d) suspended D_{50} at 1 cmab and (e) volumetric fraction of sand at 1 cmab with Re_Δ. In (a-c), the lines represent the fitted value based on the measurements, and the shaded band around each point represents standard deviation. The red dashed line in (c) represents no ripples form for 1% sand experiments when $Re_\Delta < 380$.

experiments increases with Re_Δ until $Re_\Delta \approx 550$ that D_{50}. For $Re_\Delta > 550$, D_{50} remains relatively constant.

There is no sand in suspension when the wave intensity is low; both 1% and 13% sand experiments have 0% sand fraction at 1 cmab (Figure 3.4e). For 13% sand experiments, the 1 cmab sand fraction maintains a relatively constant value of $\sim 4.8\%$ for $Re_\Delta > 450$. For 1% sand experiments, the sand fraction is constant and $\sim 0.35\%$ for $Re_\Delta > 550$. Under the transitional regime, $400 < Re_\Delta < 500$, ripples start to form in 1% sand experiments. The 13% sand experiments, started to form ripples even under low Re_Δ (*Han et al.*, 2021). The trend of the suspended sand fraction is similar to the result from *Lamb and Parsons* (2005), plotted by *Hooshmand et al.* (2015). However, the difference is that in the experiment of *Lamb and Parsons* (2005), the sand fraction reached 20% at the 10 cmab on average, which is consistent with the bed sediment used. We did not observe that high of sand fraction in suspension. It is possible that in our study, the siphon rake did not reach as close to the bed. Due to the design, siphoning the very near-bed water might suck some of the bed surface sediment into the samples, which would overestimate the sand fraction in suspension. Therefore, the missing sand fraction compared to *Lamb and Parsons* (2005) and *Hooshmand et al.* (2015) is presumably inside the 1 cm near-bed water column, moving as either the suspended load or bedload. The other possibility is the different grain size measurement method. *Lamb and Parsons* (2005) used sieve analysis to evaluate the sand fraction, but we use Beckman Coulter LS13-320 Particle Size Analyzer for all grain size ranges of our sediment. *Konert and Vandenberghe* (1997) suggested the difference between those two methods might be due to the sphericity of particles.

3.4 Discussion

3.4.1 Modified suspension criterion

The transition from a low suspended sand fraction ($\sim 0\%$ percent sand in Figure 3.4e) to a high suspended sand fraction occurs at a similar Re_Δ range at the transition of sediment

concentration and concentration gradient in the range of $450 < Re_{\Delta} < 550$, as discussed in Section 3.3.3. Therefore, we hypothesize that the suspension of the sand fraction allows the formation of a near-bed high-concentration layer. Based on the equation 3.2, we use the sediment suspension criterion from *Van Rijn* (1984) to quantify the particle size effect on the sediment suspension. Near-bed concentration and concentration gradient can be used as the criteria of wave-supported gravity flows, where *Traykovski et al.* (2000) used 10 g L^{-1} as the threshold of WSGF suspended sediment concentration and *Traykovski et al.* (2007) used 2 g $L^{-1}cm^{-1}$ as the definition of an effective WSGF concentration gradient. Though this is an assumption, the high near-bed concentration and concentration gradient are important characteristics of WSGF. In order to form and maintain suspended sediment concentrations and concentration gradients of these magnitudes, a suspension criterion must be exceeded, and here we explore the role of sand on that suspension criterion, which is one factor in the creation of WSGF. Figure 3.5a-3.5b compares the initiation of suspension criterion with calculations of the suspension parameter E^* based on the median grain size of the total sediment (D_{50}) and the median grain size of only the sand fraction (D_{sand}).

Our results suggest that the modified criterion $E^*_{\text{sand}} > 1$ predicts the initiation of a high-concentration layer in both the low (1%) and the high (13%) sand fraction experiments. In both cases suspension is very small when $E^*_{\text{sand}} < 1$. We hypothesize that this is because sand particles in these low energy conditions do not reach initiation of motion, some of which might move only as bedload, therefore coarsening the bed and forming an armor layer that inhibits suspensions of fine particles. This is consistent with the suspended sand fraction trend 1 cmab (Figure 3.4e), since the sediment in suspension is mainly from direct suspension from the bed.

We also compared the total bed erosion Δz_b, which was measured through the sidewalls with a fixed ruler at the start to the end of each experiment. Similar to the trends observed for the concentration gradient, we find that E^*_{sand} is a suitable estimator for net bed erosion in these sediment types; net erosion is small until $E^*_{\text{sand}} > 1$. This result supports the conclusion that the sand component in the sediment limits the rate of bed erosion and thus places control

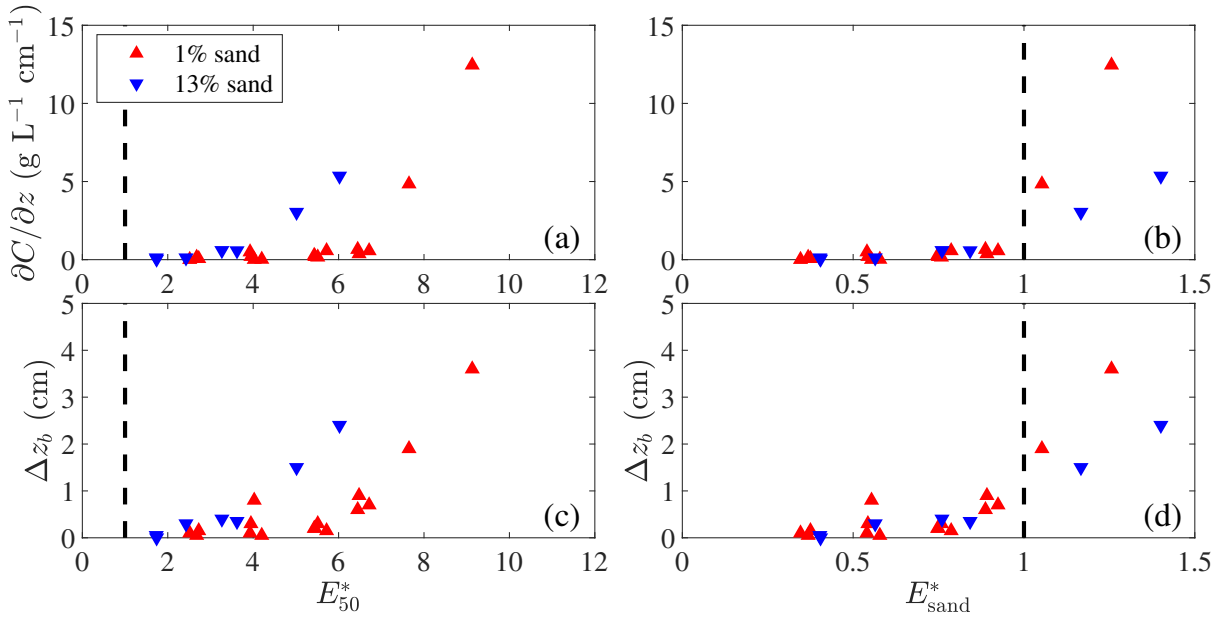

Figure 3.5: Variations of concentration gradient at 1 cmab ($\partial C/\partial z$, panel a and b) and total erosion of the bed (Δz_b, panel c and d) with different suspension parameter ($E^* = u_{*,pred}D_*/4w_o$) estimate. In (a, c), E^*_{50} represents using the median grain size D_{50} to calculate fall velocity (w_0) and non-dimensional particle size (D_*); in (b, d), E^*_{sand} represents using the median grain size of only the sand fraction (D_{sand}) in the sediment to calculate w_0 and D_*. The dashed line means $E^* = 1$ by *Van Rijn* (1984). $u_{*,pred}$ means the predicted u_* estimated using the Nikuradse roughness (*Nikuradse*, 1933).

on the formation of the high-concentration layer. The suspension criterion expressed in terms of the median grain size (E^*_{50}) is not suitable to predict initiation of suspension or the net erosion in these sediment mixtures due to the dominant role that even a small sand fraction has on the erodibility of the bed. The modified suspension criterion based on D_{sand} accounts for this and provides an improved estimator for predicting conditions when high sediment suspension is possible, which is one of the necessary conditions for WSGF formation.

To test whether our results also apply in shelf environments, we used two different data sets from field observations (*Flores et al.*, 2018; *Hale and Ogston*, 2015). In both data sets, high concentration layers are observed to form and generate wave-supported gravity flows. However, the bed grain size is very different in each. Here we test our modified suspension criterion using data during slack velocity periods when WSGF were being formed and maintained (i.e. the bed was erosional). To compare differences between periods of bed erosion and deposition, see Appendix B. We also calculated a confidence interval around the criteria using a sand fraction grain size ± 20 μm around the field measurements to account for the uncertainty in the estimates of the bed sediment grain size.

Figure 3.6 shows that the data for the field measurements fit well with the criterion based on the sand fraction; high sediment suspension is not observed when $E^*_{\text{sand}} < 1$. In contrast, the criterion based on the entire grain size distribution E^*_{50} does not correctly capture the initiation of suspension (green dashed lines in Figure 3.6). Although the field data show considerably more scatter than the lab, they are also in good agreement with the proposed suspension criterion. The main difference between the two field sites is the sediment particle size; sediment on the continental shelf offshore of the Rhine River is mainly sand (sand fraction $> 80\%$) (*Flores et al.*, 2018), whereas sediment on the shelf offshore of the Waipaoa River is mainly mud (sand fraction $\sim 5\%$). Both low and high concentration events were observed under high E^*_{sand} in the Waipaoa data (*Hale and Ogston*, 2015). We expect that this variability reflects the fact that there are many other criteria necessary to create WSGF, two of which are sediment cohesion and aggregation, and these are more likely to be evident in the muddier Waipaoa shelf environment.

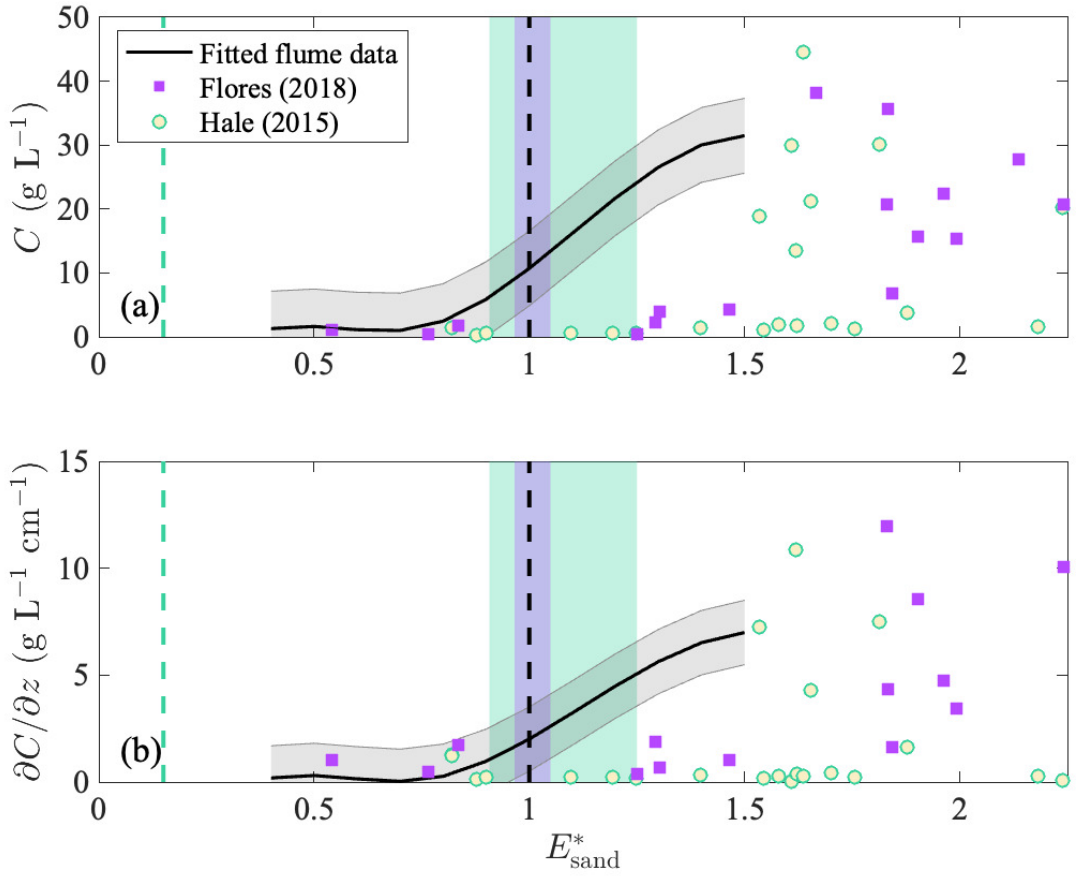

Figure 3.6: Predicted E^*_{sand} vs. (a) concentration at 1 cmab and (b) concentration gradient at 1 cmab. The dashed line represent $E^*_{\text{sand}} = 1$. The purple and green bands represent the modified sediment suspension criterion range with the calculation of sand fraction size of ± 20 μm. The green dashed lines represent the suspension criterion calculated by D_{50} for *Hale and Ogston* (2015). For *Flores et al.* (2018), D_{50} and D_{sand} are similar. The solid black lines and the gray bands represent the fitted flume data for both 1% sand and 13% sand experiments. For the data from *Flores et al.* (2018) and *Hale and Ogston* (2015), we use the data during the erosion period with the slack tide. See Appendix B for more details.

Mud-dominant environments are common in many shelf environments, which usually consist of 5% - 20% sand fraction (e.g. *Ogston et al.*, 2000; *Traykovski et al.*, 2007; *Hale and Ogston*, 2015), with some special cases as on the shelf offshore of the Rhine River with a sand fraction of $\sim 80\%$ (*Flores et al.*, 2018). Even these small components of sand in the seabed appear to be important because they control both the formation of bedforms (*Han et al.*, 2021), as well as sediment suspension. The sand fraction in predominantly muddy environments helps armor the bed since the suspension of sand requires higher shear stress. Thus, under normal weather conditions with moderate wave energy, the sand fraction is less likely to result in suspension and hence sand collects at the surface of the bed and helps form ripples. During storm events or high energy conditions, strong wave-induced shear stress can place the sand fraction in suspension, which planes out the ripples and reduces the bed-armoring effect. Therefore, a great amount of sediment from the bed is suspended into the water with the potential to form a high-concentration layer.

Our results suggest that the sand grains play an important role in the dynamics of suspension in mixed grain size mixtures, even when the sand fraction is very low; $E^*_{\text{sand}} = 1$ was a better predictor of the initiation of suspension than E^*_{50} for our 1% sand experiments and the field observations from the muddy Waiapaoa River margin. This control depends upon the time the bed exposed to certain shear stress since bed armoring and ripple formation need a longer time to come into equilibrium with the shear stress. The sediment is mostly sandy in the Rhine River study *Flores et al.* (2018), thus, using D_{50} also works well for predicting the formation of the high-concentration layer (Figure 3.6), since $D_{50} \approx D_{\text{sand}}$. This implies that the E^*_{sand} threshold works well for non-cohesive sediment, but needs modification when working with cohesive fine-grained sediment.

The modified suspension criterion for the field data seems to fall between $E^* = 1 - 1.5$ (Figure 3.6), where the most obvious suspension happens at $E^* > 1.5$. As mentioned before, sediment cohesion and aggregation effects are observed in the field, and flocculation and cohesive forces may play a similar role as sand particles by armoring the bed and prevent further erosion.

3.4.2 Estimation of shear velocity

Most suspension criteria are based on the shear velocity (e.g. *Engelund*, 1965; *Van Rijn*, 1984). For many of these suspension criteria, the predicted shear velocity is used, and the formulation may need to be different under different coastal seabed conditions. Two different predicted shear velocities ($u_{*,pred}$) using the Nikuradse grain roughness (Figure 3.7a) and using actual ripple measurements (Figure 3.7b) are compared to the measured shear velocity ($u_{*,mea}$). In Figure 3.7a we set $k_s = D_{\text{sand}}$. Note that we have also estimated $u_{*,pred}$ using $k_s = D_{50}$ and $k_s = D_{90}$ as well, however, their results are very similar to those in Figure 3.7a, as D_{50}, D_{90}, and D_{sand} are in the same order of magnitude, and therefore has limited impact on the wave friction parameter f_w. For the two different sand fraction experiments, $u_{*,pred}$ values of 13% sand experiments are more scattered compared to those of 1% sand experiments. Using Nikuradse roughness somewhat underestimates $u_{*,pred}$ for 13% sand experiments (Figure 3.7a), and those underestimates are generally eliminated when considering the actual ripple structure (Figure 3.7b). For 1% sand experiments, $u_{*,pred}$ fits $u_{*,mea}$ linearly for both of the two estimates, especially when $u_{*,pred} < 1.5$. Under higher $u_{*,mea}$, the measured shear velocity is greater than those predicted shear velocity, suggesting a more complicated bed roughness than the measured two-dimensional ripple-induced bed roughness. However, due to our limited ripple structure measurements, $u_{*,pred}$ can be assumed to provide a good statistical estimate of $u_{*,mea}$.

We use the Nikuradse roughness ($k_s = D_{50}$) to estimate this modified suspension criterion, instead of the actual roughness considering ripples, to create a pre-measurement parameter to guide future field measurements. For many field sites, the bed grain size can be estimated based on past studies or the general geological context, while the ripple structure is often more complex and time-varying. Using the Nikuradse roughness we can easily estimate E^* based on bed grain size estimates, which can be used to assess whether there is a possibility of high-concentration suspension events.

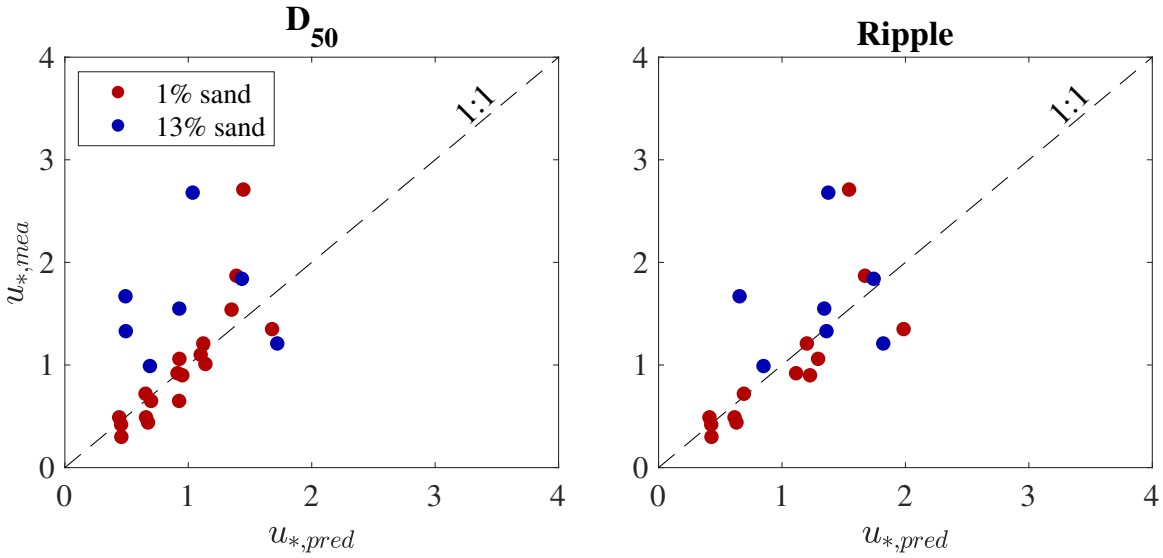

Figure 3.7: Comparison between the measured near-bed shear stress ($u_{*,mea}$) and (a) predicted near-bed shear stress ($u_{*,pred}$) using Nikuradse roughness $k_s = D_{\text{sand}}$ (*Nikuradse*, 1933) to estimate and (b) predicted near-bed shear stress ($u_{*,pred}$) using the actual measured ripple structure $k_s = 27.7\eta(\eta/\lambda)$ (*Grant and Madsen*, 1982) to estimate.

3.4.3 Sand control on the bed surface

The criterion developed here is based on the hypothesis that a thin sandy layer forms at the surface of the sediment bed in mixed sediments, which helps to form stable ripples and provides a control on the suspension of fine-grained sediments. With the increase of wave forces, the sandy layer also starts to suspend, and therefore the bed-armoring effects become less and less important, and a high-concentration layer forms. Our observations from X-radiography also provide some qualitative evidence for the sand-riched surface layer. From Figure 3.8, a thin sandier layer was formed at the surface of the bed as indicated by the bright surface on the X-radiograph negative, and a near-bed high-concentration layer was also formed, compared with the overlying water column. Throughout much the run for 13% sand fraction, the sandy layer is clear. For the run in Figure 3.8, the coarsest sediment in the grain size distribution (up to 200 μm) can form a sandy layer, so even under high wave

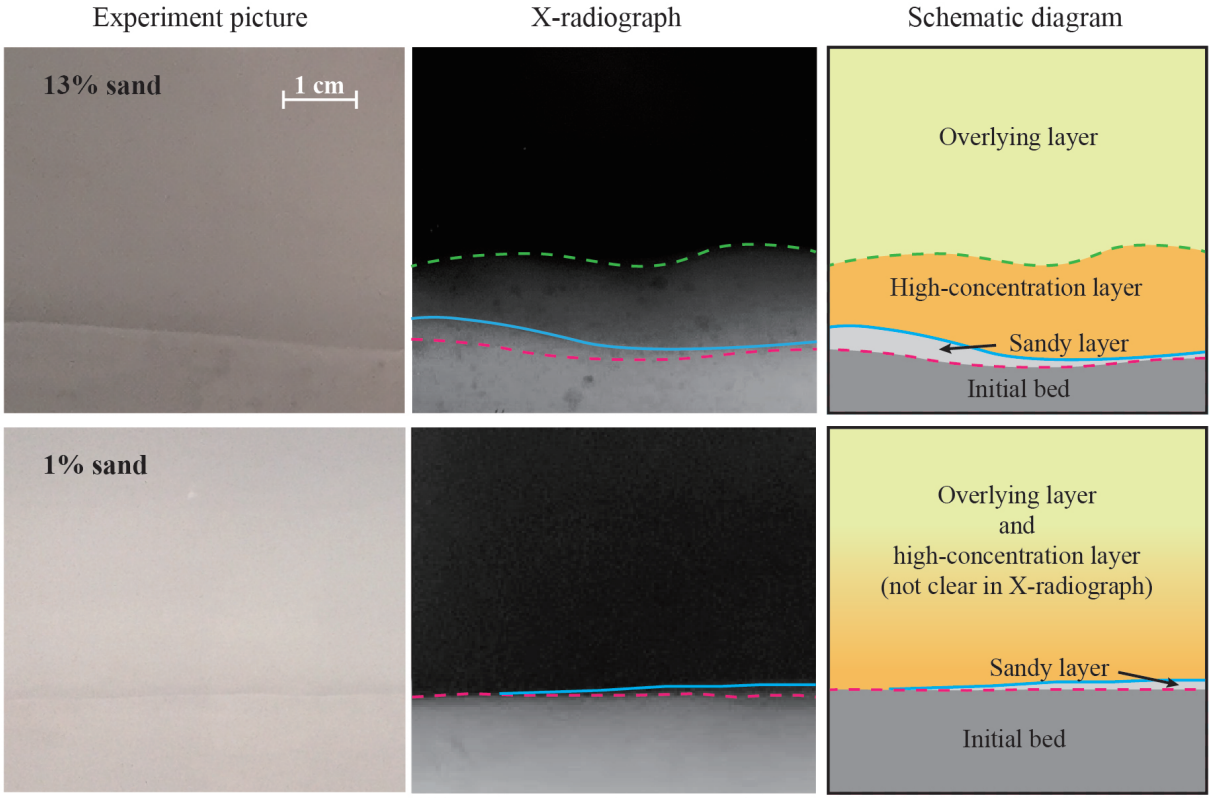

Figure 3.8: Experimental picture from the side wall, X-radiograph and schematic diagram for: 13% sand fraction experiment with $Re_{\Delta} = 640$ ($U_{orb} = 47$ cm/s); 1% sand fraction experiment with $Re_{\Delta} = 661$ ($U_{orb} = 55$ cm/s). For 1% sand experiment, the high-concentration is not clear in the X-radiograph. The X-radiograph was digitally enhanced for presentation purposes.

forcing, there is some very coarse sediment that has not reached the criterion of initiation of suspension. This sandy layer, though, has limited ability to armor the bed at the low fraction within the grain size distribution. So fine sediment could be suspended as plumes between the gaps in coarse sediment, which is clearly reported from *Liang et al.* (2007).

In addition, to predict the ripple wavelength, *Wiberg and Harris* (1994) proposed an empirical expression $\lambda_{ano} = 535D$ for anorbital ripples. For this expression, only grain size affects the ripple wavelength. In our study, the estimate of λ using D_{50} underestimates the ripple wavelength by almost an order of magnitude (Figure 3.9, triangular symbols). However, the estimate of λ is better predicted when using D_{sand} (Figure 3.9, square symbols). *Lamb and Parsons* (2005) and *Liang et al.* (2007) both observed the surface coarsening of the ripples, where more sand collects at the surface which helps stabilize the ripples. Our X-radiography shows the sandy layer forms on the surface of the bed as well. The improved prediction of λ using D_{sand} further suggests that using D_{50} might not be appropriate for predicting ripple wavelength and that the sand fraction in mud-dominant environments places control on the formation of ripples.

3.4.4 Indication of initiation of WSGF

The sediment suspension criterion is an important factor for the initiation and maintenance of wave-supported gravity flows. A necessary condition for WSGF is the formation of a high-concentration layer of suspended sediment, which our modified suspension criterion addresses. Based on our criterion, it is possible to estimate whether there is a possibility for WSGF. Recent studies have reported WSGF signals in multiple environments (e.g. *Wright and Friedrichs*, 2006; *Traykovski et al.*, 2007; *Hale and Ogston*, 2015; *Flores et al.*, 2018). In these environments, our criterion is always met. This estimation based upon our modified suspension criterion can therefore be used as a prerequisite of WSGF, and applied prior to implementing large-scale models to determine whether to include WSGF modules. If WSGF is indicated as being possible using our modified suspension criteria, we can also extend this possibility to the potential for substantial cross-shelf fluxes in these environments due to the

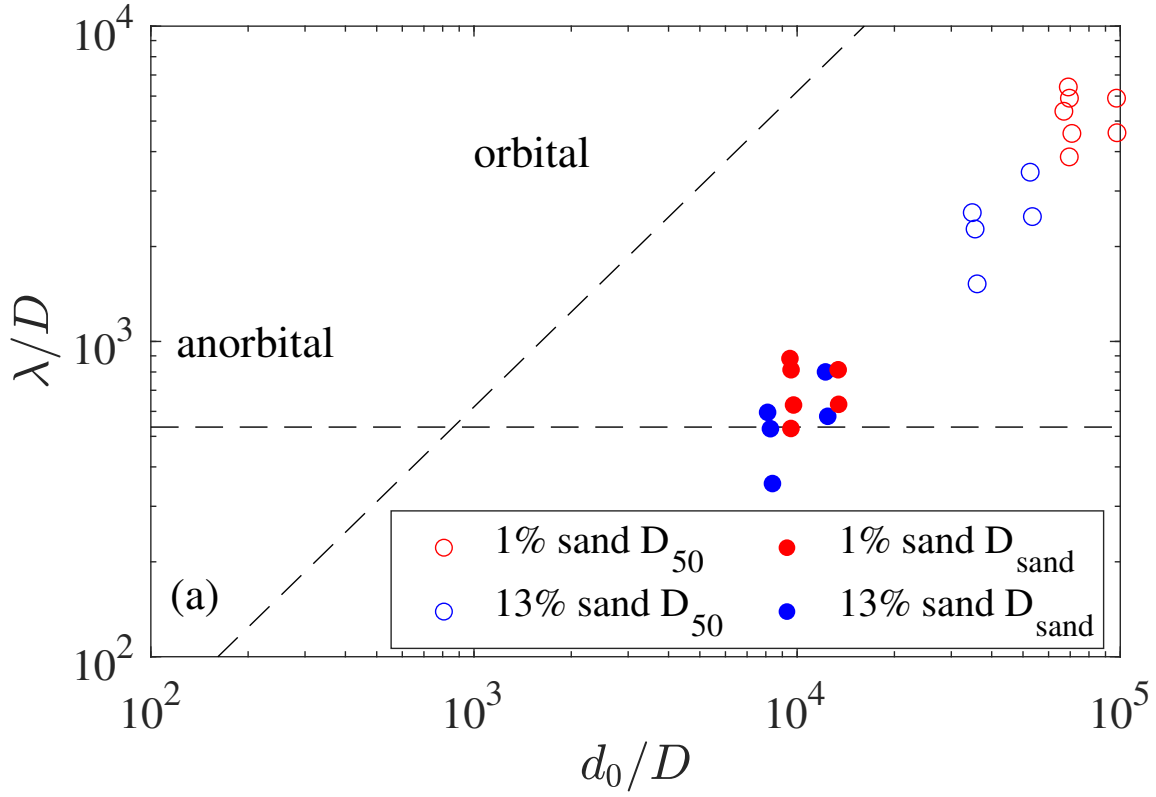

Figure 3.9: Dimensionless measured ripple wavelength (λ/D) with dimensionless orbital motion diameter (d_0/D), normalized by D_{50} and D_{sand}, respectively. Horizontal dashed line represents the anorbital estimation of ripple wavelength $\lambda = 535D$, and the diagonal dashed line represents the orbital estimation of ripple wavelength $\lambda = 0.62d_0$ (*Wiberg and Harris*, 1994).

gravitational downslope transport of the suspension.

3.5 Conclusion

We performed a series of laboratory experiments using two different muddy bed sediment mixtures: 1% sand and 13% sand fraction. High near-bed suspended sediment concentration and concentration gradient corresponds to constant near-bed suspended sand fraction when $Re_{\Delta} > 450$. The suspension of sand from the bed sediment mixture leads to the formation of a high suspended-sediment concentration layer. X-radiographs of the bed and water column shows a thin sandy layer at the surface of the bed. Using the grain size of only the sand fraction better predicted the ripple wavelength than using the median grain size of the distribution. This supports the conclusion that the sand fraction places control on the near-bed dynamics. A modified sediment suspension criterion ($E^{*}_{\text{sand}} = 1$) based on *Van Rijn* (1984) and using the median particle size of only the sand fraction in the bed is successful in predicting the necessary suspension that contributes to WSGF formation. This criterion is verified using two field measurement data sets. The modified sediment suspension criterion can be used to predict the potential for initiation of wave-supported gravity flows and is a necessary but not sufficient condition of WSGF.

Chapter 4

TEMPORAL DEVELOPMENT OF A FINE-GRAINED SEDIMENT-LADEN WAVE BOUNDARY LAYER IN A SAND-MUD SYSTEM

4.1 Introduction

Rivers deliver terrestrial sediments into coastal-shelf systems, where coarse sediment usually deposits near the coasts or on the continental shelves, while fine sediment is ultimately transported farther across the continental shelf, and possibly into the deep through multiple physical processes. In general, those physical processes that account for cross-shelf sediment transport include wind-driven flows, internal waves, infragravity phenomena, and buoyant plumes (*Nittrouer and Wright*, 1994), depending on the local weather conditions, hydrodynamics, geographic conditions, and shelf morphologies. For the past twenty years, many studies have shown that wave-supported gravity flows (WSGF) can contribute substantially to the total cross-shelf sediment transport (e.g. *Ogston et al.*, 2000; *Wright et al.*, 2001; *Scully et al.*, 2002; *Traykovski et al.*, 2007; *Flores et al.*, 2018). WSGF is a certain type of gravity flow for which external shear stress primarily from waves induces sediment suspension on a gentle slope and a high-concentration layer is formed near the seabed. Sediment is then transported downslope due to the negative buoyancy of the high-concentration layer.

The wave boundary layer (WBL) plays an important role in WSGF-driven offshore transport between the overlying water and the seabed, which is usually observed during storm events (*Harris et al.*, 2005; *Wright and Friedrichs*, 2006). The wave boundary layer is usually $1 - 3$ cm. High velocity shear, high suspended sediment concentration gradient, and direct sediment input from bed erosion all occur in this thin layer (e.g. *Ozdemir et al.*, 2010; *Hooshmand et al.*, 2015; *Han et al.*, 2021). Therefore, understanding the turbulence structure and

sediment concentration profiles inside the wave boundary layer is important for revealing the dynamics of WSGF. *Han et al.* (2021) suggested that the sediment concentration profile inside the WBL can present as a Rouse profile where stratification inside the WBL is weak, while stratification is strong at the top of the WBL. The shear stress inside the WBL directly impacts the sediment suspension from the bed. Recent WSGF models have added a new layer to represent the WBL layer between the water column layer and sediment bed layer (*Harris et al.*, 2004; *Zang et al.*, 2020). Since WBL is not only a bridge between and the bed and the upward water column but also a crucial zone of sediment transport when WSGF are formed, the sediment flux budget inside the WBL can then bed used to test the relative importance of the key factors that affect sediment suspension (*Yue et al.*, 2020).

Ripples are formed by surface gravity waves in water shallow enough for the oscillatory motion to be felt by the seabed of appropriate grain size. The formation of ripples will affect the near-bed turbulence through modification of bed friction (*Grant and Madsen*, 1986) and will enhance wave attenuation (*Ardhuin et al.*, 2002). In addition, a vortex forms on the lee side of the ripple that traps sediment eroded from the ripple surface, which will bring the sediment into the upper water column and increase the sediment suspension (*Bagnold*, 1946). Ripple geometries under equilibrium states are well studied, including the measurements and prediction equations of ripple wavelength, ripple height, and ripple steepness (e.g. *Nielsen*, 1981; *Wiberg and Harris*, 1994; *Nelson et al.*, 2013). However, near-shore benthic processes are often driven by time varying changes of various physical forces. As the bed response will often need time to reach an equilibrium state, ripples may undergo significant changes before stable conditions. Currently, there are very limited studies considering ripple adjustment. *Testik et al.* (2005) investigated the adjustment of sand ripples under changing wave intensity and reported that three main adjustment processes were identified: ripple splitting, ripple regrowth, and ripple flattening. Considering ripples formed in fine sediment, which are usually in the range of suborbital or anorbital ripples based on the classification by *Wiberg and Harris* (1994), no detailed direct measurements have been made as the ripple height is much smaller than sand ripples. The adjustment of ripples might affect the near-bed

turbulence, formation processes for high concentration layers as well as the bed reworking and redistribution of the bed-surface sand-mud mixture.

Bed erodibility is defined in different ways in the literature. It is often expressed as a threshold for erosion or as an erosion rate (*Sanford and Maa*, 2001). The erosion threshold is the critical shear stress (τ_{cr}) that initiates sediment, while erosion rate (E) is the mass of sediment eroded per unit time once the threshold is exceeded, which means the erosion rate is a function of the excess shear stress. A linear stress-flux equation for cohesive sediment erosion is widely used (*Hanson and Simon*, 2001; *Sanford and Maa*, 2001; *Son and Hsu*, 2011):

$$E = M(\tau_b - \tau_{cr})^n \tag{4.1}$$

where M is the erosion parameter. Erodibility is the propensity of sediment to be eroded, which is typically represented as an erosion threshold or erosion rate. For cohesive sediments, erodibility is affected by sediment physical properties, geochemical properties, and biological properties (*Grabowski et al.*, 2011). Physical properties affecting the erodibility include the mean particle size, particle size distribution, bulk density, water content, and temperature.

In recent WSGF models, the amount of suspended sediment in the wave boundary layer has been determined by the sediment continuity equation, which balances erosion (E) and deposition (D) at the bed and convergence of cross-shelf flux (*Traykovski et al.*, 2007):

$$\frac{\mathrm{d}C}{\mathrm{d}t} = -\frac{\mathrm{d}u_{grav}C}{\mathrm{d}x} - D + E \tag{4.2}$$

where $C = \delta_w c = \delta_w \int_o^{\delta_w} c(z)dz$ is the depth-integrated wave boundary layer sediment concentration, and c is the depth-averaged concentration. To simplify the model, most of the sediment flux is inside the wave boundary layer and the amount of sediment intrusion out of the boundary layer is assumed minimal. Assuming the gradient in horizontal flux is minimal at small spatial scales, bed elevation change can be calculated through the balance of erosion and deposition

$$c_b \frac{\mathrm{d}z_b}{\mathrm{d}t} = D - E \tag{4.3}$$

Here z_b is the bed elevation, $c_b = 1 - \phi$ is the bed volumetric concentration, ϕ is the porosity on the surface of the bed, D and E are the deposition and erosion of the bed. In this equation, $\mathrm{d}z_b/\mathrm{d}t$ is the net bed erosion rate, and deposition can be estimated $D = w_0 C_a$. Here C_a is the reference concentration at $z = z_0$ and z_0 is the roughness height. So we use $\mathrm{d}z_b/\mathrm{d}t$ to roughly represent the net bed erodibility.

Several direct wave boundary layer studies have been performed in the sediment-water system under equilibrium conditions (*Lamb et al.*, 2004; *Lamb and Parsons*, 2005; *Hooshmand et al.*, 2015; *Han et al.*, 2021). However, direct measurements during the period of bed adjustment are meager. Bed erosion, near-bed turbulence, suspended sediment concentration, and bedforms are all changing overtime during the bed adjustment period. In addition, sediment properties, such as particle size, sediment cohesiveness, flocculations will also affect these processes (*Son and Hsu*, 2011; *Han et al.*, 2021). As WSGF is usually reported under strong wave events (e.g. *Traykovski et al.*, 2007; *Hale and Ogston*, 2015; *Flores et al.*, 2018), the temporal change of wave event might also be crucial for the WSGF transport. Time-varying wave intensity, sediment suspension, and the bed behavior might affect the WSGF transport processes inside the wave boundary layer. Therefore, the first step is to understand the bed adjustment process at a specific wave intensity, as it will unravel the formation process of a high concentration layer and WGSF transport, and the corresponding processes that affect the transport. So it is important to directly measure temporal changes in the wave boundary layer - sediment bed exchange systems.

In this paper, we present four sets of bed adjustment experimental results using bed sediment consisting of 1% and 13% sand fractions. Those experiments are used to investigate how the bed and near-bed turbulence respond during the bed erosion before the equilibrium state. Different stages of bed-boundary layer evolution are classified during the temporal development period. Different controlling mechanisms of the bed erosion and deposition will be discussed. The bed behavior over time is reported, including ripples and grain size of the bed surface.

Table 4.1: Time series experiment parameters[a]

Run	Sediment	U_{orb} (cm s^{-1})	T (s)	Re_Δ
TS-1-631	1% sand	40.5	8.7	631.1
TS-1-617	1% sand	37.8	9.6	617.3
TS-13-682	13% sand	45.9	8.2	682.0
TS-13-633	13% sand	39.7	9.1	632.7

[a] $Re_\Delta = U_{orb}\tilde{\Delta}/\nu$ represents the Stokes Reynolds number, where $\Delta = \sqrt{2\nu/\omega}$ is the Stoke boundary layer thickness (*Hooshmand et al.*, 2015; *Han et al.*, 2021).

4.2 Experimental setup

Time-series experiments were performed in an oscillating water tunnel, which has a 5 m long, 1 m high, and 0.2 m wide experimental section (Figure 4.1a). The near sinusoidal oscillatory flows in the experimental section are driven by an up-and-down moving piston on one side which produces oscillatory motions. The horizontal oscillatory motions were aimed to simulate one-dimension fluid motions driven by surface gravity waves as they are felt on the seabed of continental shelves. We performed two 1% sand cases and two 13% cases to compare the dynamical differences under variant wave intensity and different sand-mud mixture (Table 1). We started measuring the data from the start of each run, and the time we ended each run was when the bed stopped from eroding. The total run time was around two hours.

The sediment we used is US Silica SIL-CO-SIL 45 (clay:silt:sand = 0.27:0.72:0.01) and SIL-CO-SIL 106 (clay:silt:sand = 0.20:0.67:0.13) crushed silica, which consists of 1% sand fraction and 13% sand fraction, respectively, similar to the experiments from *Han et al.* (2021) which is performed under the equilibrium state. The detailed grain size distribution is shown in Figure 4.1b. The sediment is weakly cohesive compared to the sediment in the

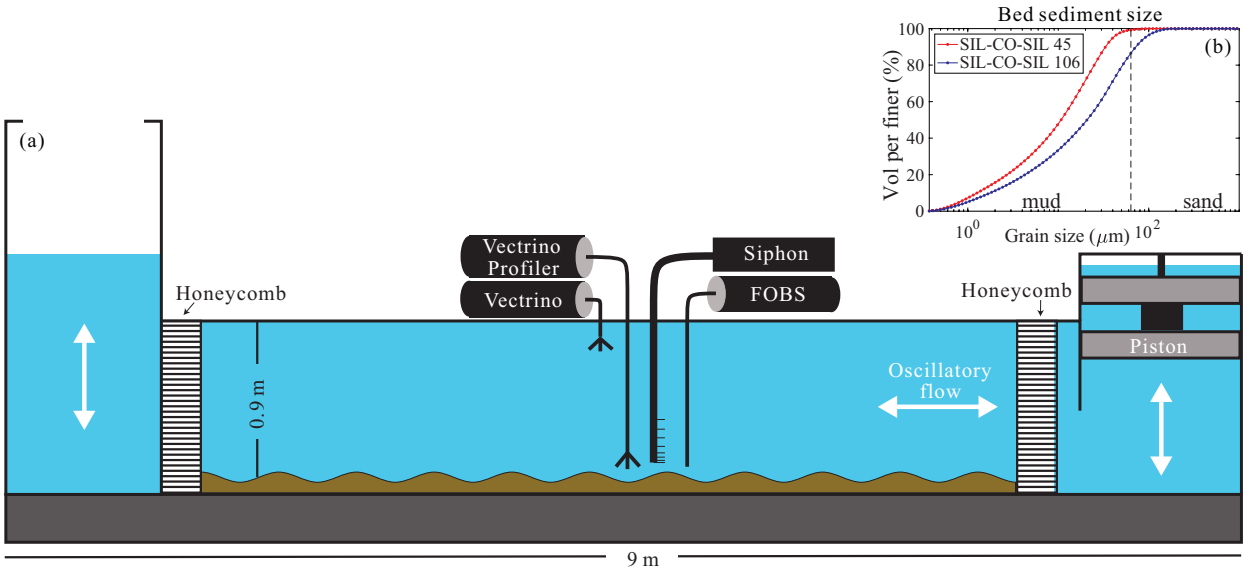

Figure 4.1: (a) Schematic oscillating water tunnel. Oscillatory motion is driven by the piston on the right. The width of the tank in the middle section is 0.2 m. (b) The cumulative bed sediment particle size distribution for 1% sand fraction sediment (SIL-CO-SIL 45) and 13% sand fraction sediment (SIL-CO-SIL 106).

natural field of similar grain size, so sediment aggregation property is different from the natural sediment.

Velocity and turbulence measurements were performed using the Nortek Vectrino Profiler near the bottom. The Nortek Vectrino Profiler sensor is updated compared to (*Han et al.*, 2021) and has a good measurement of 3 cm in total with a vertical resolution of 1 mm. Based on our past experiments, the bed erosion is around 1.3 - 1.7 cm. So initially we set the bed in the middle of this measurement zone, and with the bed erosion, the measurement zone can still capture the very near-bed information. Therefore the measurement of velocity and turbulence profiles increases as the bed elevation goes down. An exception is a case TS-13-682, where the total bed erosion is greater due to higher Re_{Δ}, so we have to move the Nortek Vectrino Profiler down once in the middle of the run. A single point Nortek Vectrino was set at 70 cm above the bed (cmab) to provide a reference phase for velocities.

Suspended sediment concentrations (SSC) were measured with 20-bin fiber-optic backscattering sensors (FOBS) with 10 mm spacing between the lowermost 10 sensors and progressively wider spacing above, which in total provided a 50 cm SSC profile. The FOBS was calibrated with Sil-co-Sil 45 and Sil-co-Sil 106 sediments separately in a mixing tank, and the calibrations showed linear responses for concentrations below 80 g L^{-1}. The sediment siphon rake was placed at eight different vertical locations with a 2 mm spacing of lowermost 2 ports and wider spacing above. During the experiments, FOBS is moving down every 5 min to keep a relatively constant distance with the bed surface as the bed elevation goes down.

The bed elevation over time was estimated based on the Nortek Vectrino profiler, where the zero velocity represents the bed. This was also calibrated by a fixed camera on the side of the flume, which recorded a near-bed zone of 9 cm width and 5 cm height. The bed elevation from the camera was estimated based on the image processing using the boundary detection algorithm (*Boreczky and Rowe*, 1996) to get the bed surface structure and averaged 1 cm around the Nortek Vectrino Profiler measured point. Ripple heights (η) and wavelengths (λ) inside the test section were based on observation with the same fixed camera through

the test section sidewall. Before the quasi-steady state has been reached, transient ripples formed in each case where the structure kept changing and sometimes seems non-periodic. Therefore, η and λ of the transient ripples were then defined basically around the turbulence measurement location through fixed camera videos. Due to the non-periodicity of transient ripples, identified through the visual decision. Ripple steepness (η/λ) was calculated based upon η and λ. Bed activity a_b is defined based on the five-minute root mean square of fluctuations of the local bed elevation from the mean bed elevation change.

The bed particle size was sampled using a vertical cylindrical sampler, which sampled around 3 - 5 cm bed cylindrical core after each case. Sediment cores were then cut every two 2 mm and evaluated using Beckman Coulter LS13-320 Particle Size Analyzer. The bed volumetric concentration is $c_b = 1 - \phi$, where ϕ is the bed porosity. We estimated c_b based on a separate sediment core sampled after each run. The top 2 cm core was cut and dried in a 60°C oven and then weighed to get the mass m. c_b is then estimated based on $c_b = m/\rho_s V_c$ where V_c is the volume of the 2 cm cylindrical core.

Most of our measurement parameters, including turbulent kinetic energy (TKE), Reynolds shear stress (RSS), suspended sediment concentration (C) and concentration gradient ($\partial C/\partial z$), were averaged every five minutes to compare the temporal changes. To non-dimensionalize the bed erosion rate, we calculated a near-bed 5 mm averaged square root of Reynolds shear stress $\sqrt{-\overline{u'w'}_{5\mathrm{mm}}}$ to represent very near-bed shear stress intensity, which directly impacts the erosion of the sediment. We also tried the 10 mm averaged and WBL-averaged square root of Reynolds shear stress, which shows similar trends. The pseudo-color plots used the one-minute-average data to provide more basic information over time (see Figure 4.2). The Reynolds stresses per unit mass were calculated as $-\overline{u'w'}$, where the overbar represents the phase average of the measured data. The eddy viscosity ν_e is estimated based on

$$\nu_e = \frac{|-\overline{u'w'}|}{\partial U/\partial z} \tag{4.4}$$

Eddy diffusivity is estimated based on $K_t = Sc_t \nu_e$, where $Sc_t = 1$ is the turbulent Schmidt

number which we set as one. Gradient Richardson number Ri_g is estimated as

$$Ri_g = -\frac{g(\partial\rho/\partial z)}{\rho(\partial U/\partial z)^2} \approx -\frac{gs(\partial c/\partial z)}{\rho_s(\partial U/\partial z)^2} \tag{4.5}$$

Settling velocity was estimated through $w_0 = \sqrt{4(s-1)gd/3C_D}$, where $s = (\rho_s - \rho_w)/\rho_w$ represents the submerged weight of siliceous sediment relative to the water, and C_D represents the drag coefficient. For very fine sediment the law of Stokes was used as $C_D = 24/Re_d$; for the coarser sediment, $C_D = 24/Re_d + 1.5$ (*Engelund and Hansen*, 1967), where $Re_d = w_0 d/\nu$ is the particle Reynolds number. Here for the suspended sediment settling velocity used in Section 4.4.5, the grain size is estimated based on a siphon sampler siphoning the water in 1 cmab using the same gran size analyzer as the bed grain size.

4.3 Results

4.3.1 Temporal adjustment of the boundary layer and sediment bed

The Reynolds shear stress (RSS) of two characteristic cases are shown in Figure 4.2a and 4.2d. The pseudo-color plots are the one-minute-average RSS over time. For both 1% sand and 13% sand fraction experiments, a high near-bed RSS zone occurred in the first $30-40$ min (RSS $>$ 1 cm^2 s^{-2}), suggesting the bed adjustment from the initial condition. This adjustment time is around 30 min for the case TS-1-631 and 40 min for the case TS-13-633. However, for 13% sand experiments, the thickness of a high turbulence zone is greater than 1% sand experiment. After the initial adjustment, the high RSS occurred at around 5 mm above the bed. Some extremely high RSS happened in the middle of the case. For example, at 45 min and 75 min of TS-1-631 and 50 min of TS-13-633, RSS is high and the thickness of this high turbulence zone is expanded vertically. For 13% sand experiments, a thickened RSS zone occurred in the near-bed 10 mm after 90 min, which we did not observe in the 1% sand experiment.

Characteristic suspended sediment concentration profiles for every 10 min are shown in Figure 4.3. The near-bed concentration reaches a relatively stable concentration ($C = 15-20$ g L^{-1}) in 10 min, and then the following suspended sediments are transported upward

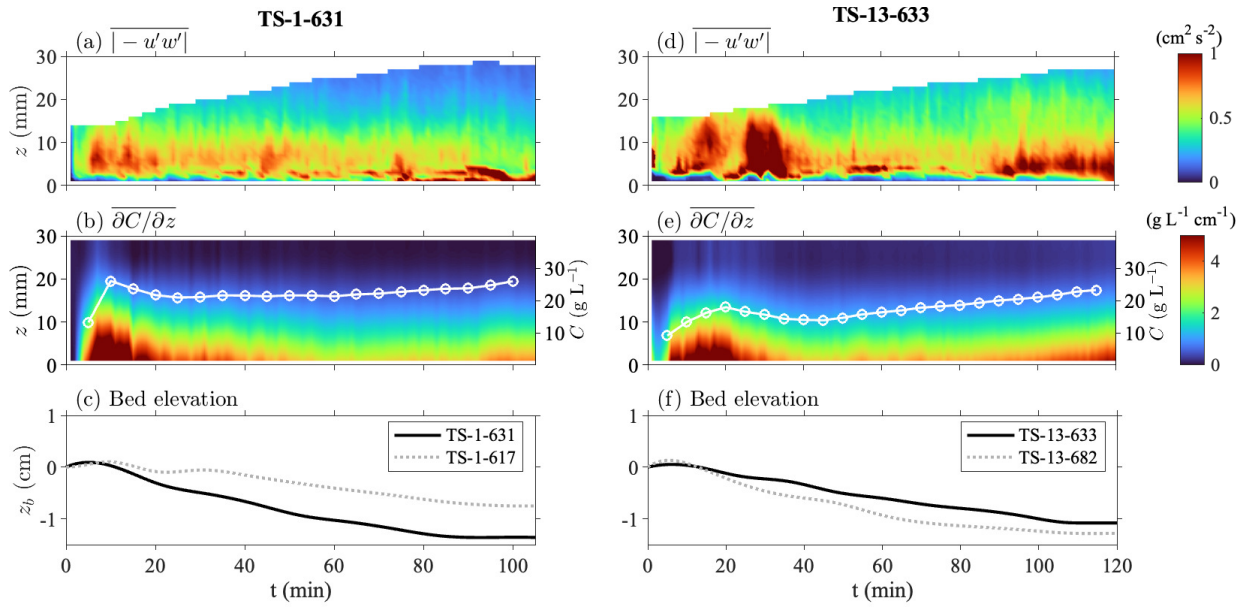

Figure 4.2: Characteristic Reynolds shear stress ($-\overline{u'w'}$, panel a and d), concentration gradient ($\partial C/\partial z$, panel b and e), and bed elevation (z_b, panel c and f) for 1% sand fraction experiment (TS-1-631, 1% sand, $Re_\Delta = 631$) on the left and 13% sand fraction experiment (TS-13-633, 13% sand, $Re_\Delta = 633$) on the right. For panel a, b, d and e, the data plotted are one-minute-average data and the bed elevation changes over time have been removed from this figure to easily compare the dynamical changes in a similar position relative to the bed. In panel b and e, the white lines represent five-minute-average near-bed concentrations. In panel c and f, bed elevations for another two cases are plotted as dotted lines.

out of the wave boundary layer until the equilibrium sediment concentration profiles are reached. A high suspended concentration gradient appears in the near-bed 5 cm region. To focus on the near-bed region, Figure 4.2b and 4.2d show the suspended concentration gradient in the near-bed 3 cm zone. The fast suspended sediment will be transported upward out of the wave boundary layer and the suspended sediment concentration remains at a relatively constant value. In our past experiments under the equilibrium state (*Han et al.*, 2021), suspended sediment concentrations for 1% sand are higher than 13% sand experiments. In the present two cases, however, sediment concentration for the 13% sand experiment is similar to the 1% sand experiment (Figure 4.2b and 4.2e). One possible reason is that the introduced residual sediment from the end tank leads to the greater near-bed sediment concentration of 13% sand (Figure 4.2b and 4.2e). However, this introduced residual sediment will be eliminated when calculating the suspended sediment concentration gradient. The second possible reason is that we put the sediment settle down for 1 day to make a similar bed consolidation rate, which might still be different. Another possible reason is the absolute position of the FOBS, as the FOBS is fixed and the bed is eroding. To keep the FOBS in a fixed position relative to the bed, we have to move FOBS down with the bed erosion. As the control of that is hard, it is possible that the sensors of FOBS for TS-13-633 might be closer to that of TS-1-631.

The bed elevation changes over time are shown in Figure 4.2d and 4.2h. Comparing TS-1-631 and TS-1-617 (Figure 4.2d), the total bed elevation changes increased with Re_{Δ}, as higher wave intensity tends to make more sediment in suspension. Similarly, the comparison between TS-13-633 and TS-13-682 shows a similar trend. Temporally, the bed elevation decrease or increase in the first 20-40 min, where residual sediment introduced from the end tank and non-uniform of initial bed makes the bed reworks and sediment redistributes during this time, and the transient ripples start to form, which might increase the bed elevation as well. Between 30 - 90 min for 1% sand and 40 - 105 min for 13% sand, the bed elevation decreases at a nearly constant rate. The total adjustment time before the bed is stable for the 1% sand experiment is faster than that of 13% sand. After the bed adjustment, the bed

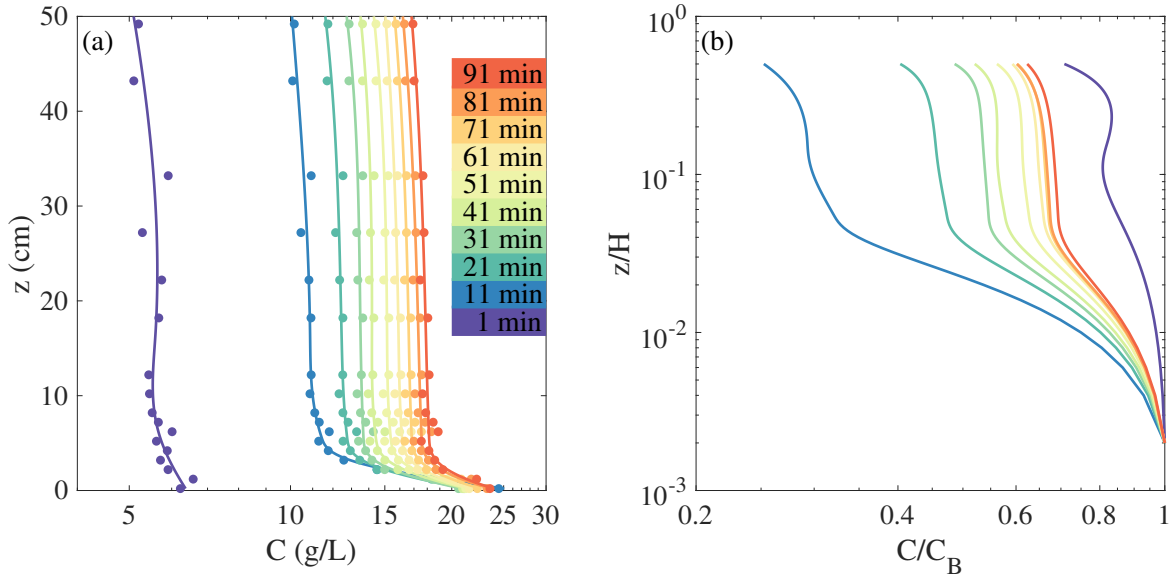

Figure 4.3: Characteristic (a) suspended sediment concentration (C) profiles and (b) dimensionless concentration profiles relative to the near-bed concentration (C_B) for the case TS-1-631 every 10 min. $H = 1$ m is the tunnel depth.

is dynamically stable and the system reaches an equilibrium state.

For both 1% sand and 13% sand fraction experiments, three different stages can be divided: the initial bed adjustment (first 30-40 min), the decreasing erosion(30 - 90 min for 1% sand, and 40 - 105 for 13% sand), and near-equilibrium (after 90 min for 1% sand and after 105 min for 13% sand). In the initial bed adjustment stage, bed elevation might either increase or decrease and a strong sediment concentration gradient forms. In the decreasing erosion stage, bed elevation keeps decreasing, and the near-bed concentration slightly increases over time. In the near-equilibrium stage, the bed becomes dynamically stable. The detailed three-stage regime will be discussed in Section 4.4.5.

4.3.2 Ripples

Unlike stable ripples presented from *Han et al.* (2021), we observed transient ripples formed during the bed adjustment period of the system before the equilibrium state was reached.

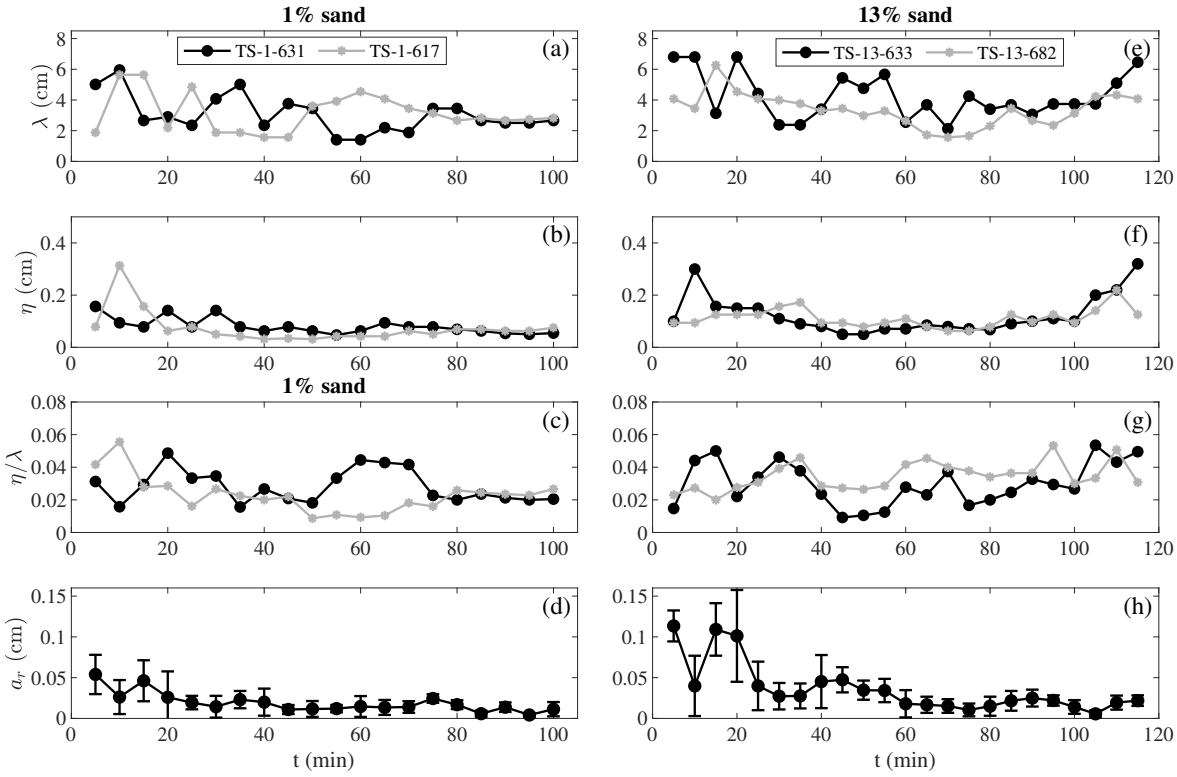

Figure 4.4: Variations of (a, e) ripple wavelength λ, (b, f) ripple height η, (c, g) ripple steepness η/λ, and (d, h) bed activity a_b over time for 1% sand experiments on the left and 13% sand experiments one the right. In panel d and h, we only plotted the case TS-1-631 and TS-13-633, where the trend for the rest case is similar.

The structure of transient ripples is unstable; both the ripple wavelength (λ) and ripple height (η) vary over time (Figure 4.4a, 4.4b, 4.4e, 4.4f). From Figure 4.4b and 4.4d, the observed transient ripple heights are between 0.8 to 3.5 mm. The value of η alters rapidly in the first 40 min. For example, for the cases TS-1-617 and TS-13-633, the greatest η forms at t = 10 min. For 1% sand experiments, η remains at a nearly constant value of $\sim$ 1 mm when $t > 40$ min. For 13% sand experiments, η remains at a nearly constant value of $\sim$ 1 mm when $40 < t < 100$ min. However, η increases significantly when $t > 100$ min, where we observe the stable ripples start to form and those ripples do not migrate anymore.

The range of transient ripple wavelength λ for all cases is 1.5 - 7.5 cm. Unlike η, λ changes significantly over time. For 1% sand experiments, stable ripples start to form with $\lambda \approx 3$ when $t > 85$ min; for 13% sand experiments, however, λ of stable ripples reaches 6.5 cm at last, similar to what has been observed before (*Han et al.*, 2021). For transient ripples, ripple wavelength variations control the shape of ripple evolution, as new ripples might form under the old ripples and some local disturbance of the bed might help create a new solitary ripple. A more detailed discussion of transient ripples will be discussed in Section 4.4.3.

4.3.3 Bed grain size

Bed grain size profiles can be used to estimate whether the bed is coarsened. For 1% sand experiments, sediment under 0.2 cm is similar to the initial bed settings (Figure 4.5a-4.5b). For the measured data, grain size is scattered below the surface. The surface of the bed is slightly coarsened compared to the lower sediment: D_{50} of the bed surface is $\sim$ 15.2 μm compared to the averaged grain size 11.1 μm below the surface, which is similar to the initial sediment 11.7 μm (Figure 4.5a); the sand fraction on the surface increased to 1.5% compared to the averaged sand fraction 1.13 below the surface, which is similar to the initial sediment 1.1% (Figure 4.5b). For 13% sand experiments, the surface of the bed is coarsened significantly: D_{50} of the bed surface is $\sim$ 28 μm compared to the averaged grain size 23.4 μm below the surface, which is similar to the initial sediment 22.8 μm (Figure 4.5c); the sand fraction on the surface increased to $\sim$ 17.5% compared to the averaged sand fraction 13.9%,

which is slightly greater than the initial sediment 13.3% (Figure 4.5d). As the sediment core is cut every 2 mm, the measured bed surface grain size is the averaged value for the surface 2 mm sediment bed. The real bed surface might be more coarsened than our measured value.

4.4 Discussion

The objective of this work is to understand the temporal development of the wave boundary layer in order to elucidate the key factors that control sediment suspension, including bed erodibility, ripple formation during the adjustment period, and sediment-induced stratification. The bed is observed to evolve in three stages based on the bed elevation: an initial adjustment period (Stage I), where elevation might increase or decrease; a decreasing erosion rate period (Stage II), where bed elevation decreases over time; and a near-equilibrium period (Stage III), where the bed elevation is near-constant.

For bed erosion, several definitions are necessary: bed erosion, bed erodibility and net erosion. As described in the equation 4.1, bed erosion $E = M(\tau - \tau_{cr})^n$ is a function of the excess shear stress, where M is the erosion parameter. Bed erodibility, which is usually the bed condition that limits the sediment in the bed from erosion, affects M, critical shear stress τ_{cr} and the index n. Mathematically and conceptually, E is used to represent bed erodibility as well. Net erosion is quantified as the bed elevation change rate $\mathrm{d}z_b/\mathrm{d}t$,and $\mathrm{d}z_b/\mathrm{d}t = 0$ represents bed elevation becomes constant for which we usually define an equilibrium state, i.e., the balance between the deposition and erosion rates ($D = E$).

In this discussion section, we first propose three potential controlling mechanisms of the sediment suspension in the wave boundary layer: pure settling control, bed control, and stratification control. Then we describe separately the roles of bed erodibility, transient ripples, and stratification. Finally, we summarize three stages during the total bed adjustment period, where the role of different factors will be clarified in those three stages.

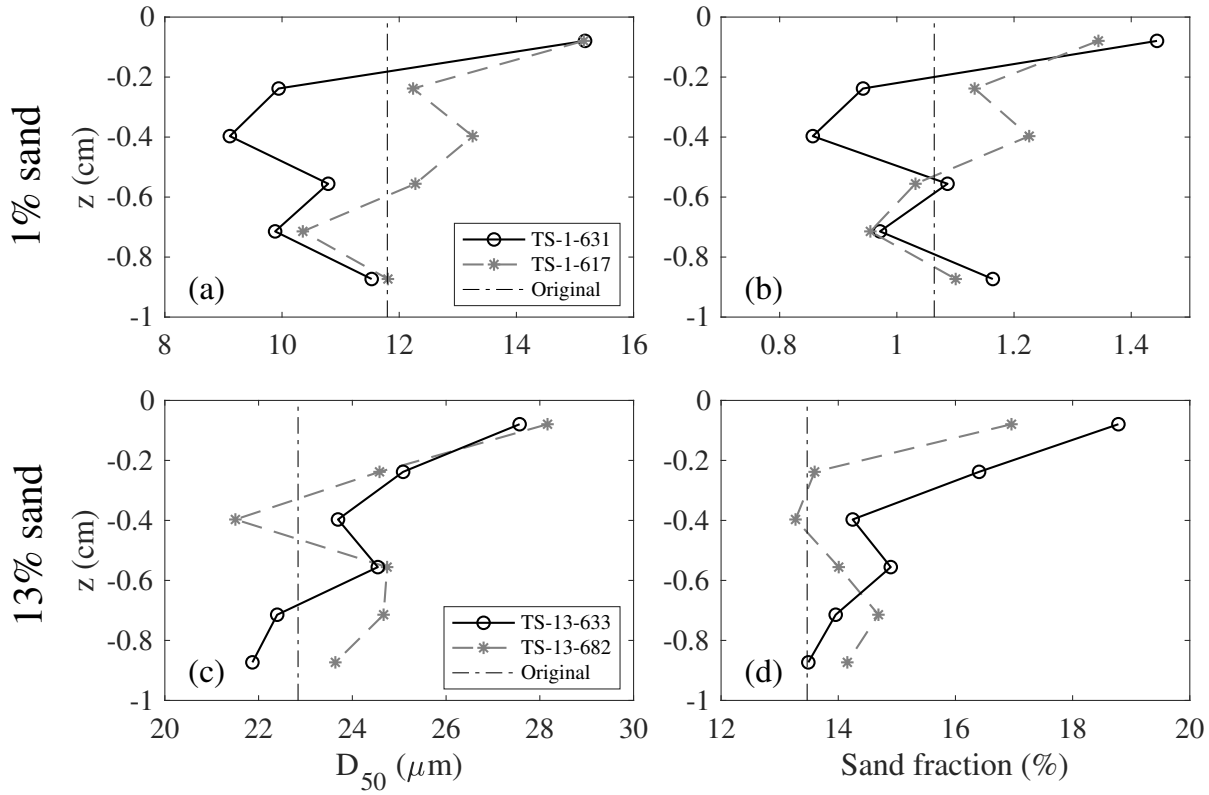

Figure 4.5: Bed grain size profile of (a, c) D_{50} and (b, d) sand fraction percentage for 1% sand and 13% sand experiments. Here $z = 0$ represents the surface of the bed. The vertical dashed lines represent the original sediment grain size before putting into the tunnel.

4.4.1 Controlling mechanisms of the erosion and deposition

Generally, the equilibrium state is defined based on the balance between the erosion and deposition at the bed. The variance of deposition and erosion during the bed adjustment period significantly affects the near-bed sediment-laden system. Deposition $D = w_0 C$ is due to sediment settling at the bed; it is low at the beginning of the total bed adjustment period (Stage I), and increases over time as suspended sediment concentration increases as more sediments are suspended. Meanwhile, erosion might either remain constant or decrease over time due to the variation of bed erodibility. In the laboratory experiments, sediment settling always deposits the sediment as long as there is sediment in suspension, while surface coarsening effects and formation of transient ripples account for the variation of bed erodibility, which leads to the variation of the erosion rate; stratification, on the other hand, can cause the variation in the deposition rate. So in a fine-grained sediment-laden wave boundary layer, two different mechanisms exist that might limit the concentration in the wave boundary layer: bed control, and stratification control. The actual control in the sediment-laden wave boundary layer is undoubtedly the combination of all of those factors.

In the absence of stratification or variations in bed erodibility, a simple balance exists between sediment settling and resuspension. This has been widely accepted as the description of the concentration profile for dilute suspended sediment in steady flow over a sediment bed *Rouse* (1937). In this control, deposition $D = w_0 C$ is low at the beginning, as only a shore amount of sediment is suspended. Over time, D increases over time as more sediment is mobilized from the bed into suspension. The erosion rate of the bed remains at a relatively constant value, which means the sediment bed is well-sorted and well-mixed, and bed erodibility does not increase or decrease over time. The concentration within the entire boundary layer increases to bring the profile in compliance with the Rouse profile. As D increases, the equilibrium is finally reached when $D = E$ at the sediment-water interface. At any elevation of the boundary layer, upward turbulent diffusion is balanced with sediment settling $w_0 C(z) + K_t \partial C(z)/\partial z = 0$, where K_t is the sediment diffusivity. Then the bed is

dynamically stable as the amount of the sediment in suspension and the sediment deposited are equal.

The bed control is when the bed characteristics are also key factors in the bed erosion aside from the sediment settling. Sediment erosion is affected by the variation of bed erodibility, and usually, the typical bed erodibility decreases over time. For muddy cohesive sediment, little change in erodibility is showed with depth into the bed with laboratory remolded sediment (*Roberts et al.*, 1998), but erodibility of deposited fine sediments often decreases significantly with depth due to bed consolidation, especially near the sediment surface (*Mehta*, 1988; *Sanford and Maa*, 2001). For mixed sand-mud beds, bed armoring due to the surface coarsening limits the bed from further erosion (e.g. *Wiberg et al.*, 1994; *Sanford*, 2008). So for this control, D increases over time while E generally decreases over time, and finally the bed is dynamically stable when $D = E$ at the surface of the bed.

For the stratification control, the influence of stratification increases over time as more sediment gets suspended. *Han et al.* (2021) determined stratification only plays a significant role at the top of the wave boundary layer and stratification is weak inside the wave boundary layer. However, strong stratification at the top of the boundary layer prevents sediment from being transported out of the boundary layer. So although the Rouse Profile can be used to estimate the concentration profile inside the wave boundary layer (*Chen and Chen*, 2018; *Han et al.*, 2021), the concentration profile for the boundary layer and above is divided into two sections. So with the addition of stratification, concentration inside the wave boundary layer increases faster which leads to the faster increase of D over time compared to the pure settling. So even though E does not decrease over time, the total net erosion deviates from the pure settling.

4.4.2 Net bed erosion and bed erodibility

The net bed erosion rate $\mathrm{d}z_b/\mathrm{d}t$, or bed elevation change rate, directly reflects the bed adjustment. In natural environments, the net bed erosion rate is usually not a constant value as both flow and bed conditions vary over time. Similarly, the erosion of the bed is

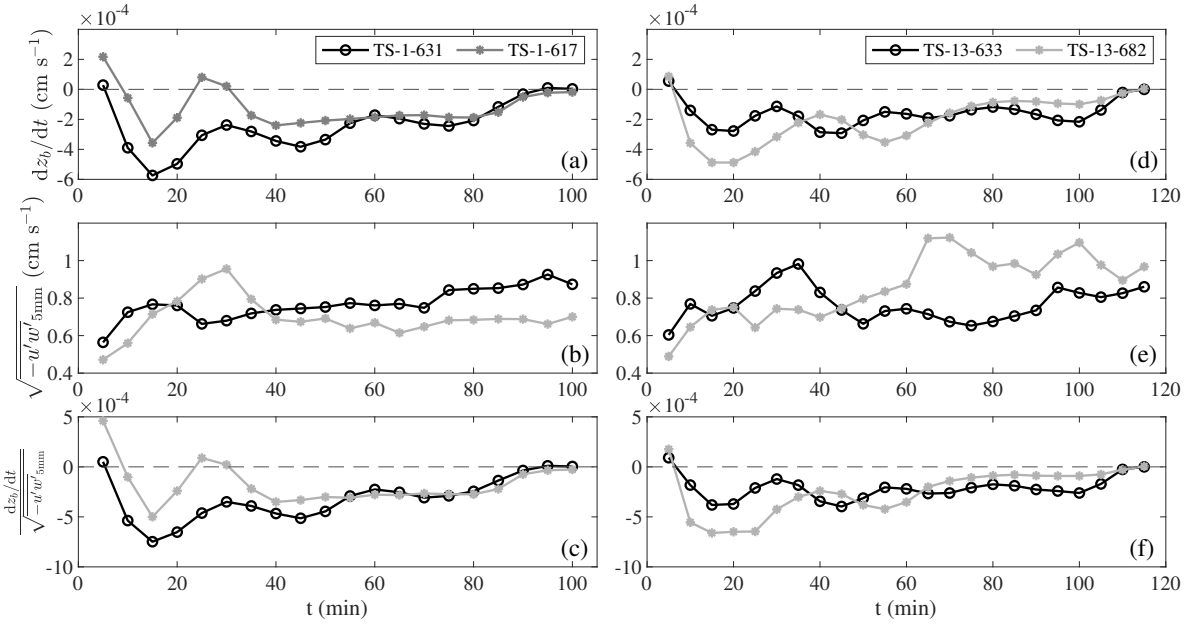

Figure 4.6: Variations of (a, d) bed erosion rate $\mathrm{d}z_b/\mathrm{d}t$, (b, e) square root of near-bed 5 mm averaged Reynolds shear stress $\sqrt{-\overline{u'w'}_{5\mathrm{mm}}}$, and (c, f) dimensionless bed erosion rate $(\mathrm{d}z_b/\mathrm{d}t)/\sqrt{-\overline{u'w'}_{5\mathrm{mm}}}$.

not linear with time in our experiments.

In the 1% sand experiments, $\mathrm{d}z_b/\mathrm{d}t$ can be either positive or negative when $t < 40$ min. As mentioned in Section 4.3.1, the bed is reworking from the initial condition in Stage I, when $t < 30$ min for 1% sand experiment and $t < 40$ min for 13% sand experiment (Figure 4.2), and transient ripples start to form shortly after the start of the run. Several reasons can be accounted for $\mathrm{d}z_b/\mathrm{d}t > 0$. Before the start of each run, we raked the sediment bed, making it as level as possible to initialize a plane bed. However, the bed was not completely planar, and the bed roughness might still exceed the particle size roughness. Initial bed distribution and residual sediment from the end tanks may also result in short term adjustments to the bed in the first stage of the experiments, resulting in $\mathrm{d}z_b/\mathrm{d}t > 0$. Another possible reason is the formation of transient ripples. We set the Vectrino Profiler in a fixed position, so the increase of the bed elevation might be the formation or migration of transient ripples. In the decreasing erosion rate stage, Stage II, $\mathrm{d}z_b/\mathrm{d}t$ slightly decreases over time except for the case TS-13-633 where $\mathrm{d}z_b/\mathrm{d}t$ remains a relatively constant value. In our parameter space, $\mathrm{d}z_b/\mathrm{d}t = -1.5 \sim -3 \ \times 10^{-4}$ cm s^{-1}. For 1% sand experiment, Stage II is between 30 min $< \mathrm{d}z_b/\mathrm{d}t <$ 80 min, while Stage II for 13% sand is 40 min $< \mathrm{d}z_b/\mathrm{d}t <$ 100 min. In the near-equilibrium stage, the absolute value of $\mathrm{d}z_b/\mathrm{d}t$ decreases and finally reaches zero.

In general, the net bed erosion rate decreases after the initial adjustment stage. In the absence of other competing factors, a decrease in bed erosion could result from a decrease in the near-bed shear stress. However, we observe that the near-bed shear stress does not decrease over time (Figure 4.6b and 4.6e). For 1% sand experiment, $\sqrt{-\overline{u'w'}_{5\mathrm{mm}}}$ slightly increases after 22 min; for 13% sand experiment, $\sqrt{-\overline{u'w'}_{5\mathrm{mm}}}$ slightly increases after 44 min. Therefore, we define a dimensionless net bed erosion rate $(\mathrm{d}z_b/\mathrm{d}t)/\sqrt{-\overline{u'w'}_{5\mathrm{mm}}}$ and we find that the trend is similar to the bed erosion rate. So after the initial adjustment stage, the net bed erosion rate decreases and finally drops to zero. Therefore, the decrease of net bed erosion is not the result of the decrease of near-bed stress, which slightly increases over time (Figure 4.6b).

Bed erodibility limits the mass of fine sediment suspended from the seabed into the wave

boundary layer and is a very sensitive parameter that needs to be carefully estimated in models (*Harris et al.*, 2005). In natural coastal environments, bed erodibility varies in time and space and is affected by grain size distribution, sediment consolidation and biological processes (*Friedrichs et al.*, 2008). In our experiments, there are no biological or cohesive processes as our sediment is artificial crushed silicious sediment. As discussed in Section 4.3.3, the bed surface collects more sand particles which armor the bed from further erosion. *Liang et al.* (2007) reported fine sediment suspended from the bed as plumes that escape from the gap of coarse sediment at the surface, and finally, when the bed surface has enough coarse sediment (sand), the bed stops eroding. Therefore, bed armoring due to surface coarsening effects influences and may be a dominant factor in the decrease of bed erodibility. Meanwhile, an active layer is defined within the bed where only sediment in the active layer can be eroded (e.g. *Wiberg et al.*, 1994; *Harris and Wiberg*, 2001, 2002; *Traykovski et al.*, 2007). The bottom of the active layer is where $\tau = \tau_{cr}$, and here it is suggested that the increase of τ_{cr} from the surface of the bed to the bottom of the active layer controls the active layer depth. In our experiments, bed consolidation might increase with depth in the bed, although it is not likely with the non-cohesive sediment in the experiments. However, due to the limitation of our measurements, we did not capture the vertical variance of the bed consolidation. In our experiments, the bulk bed porosity ϕ is 0.35 and 0.37 for 1% sand and 13% sand experiment, respectively. In general, we can infer that the bed erodibility generally decreases over time mainly due to surface coarsening effects, and this process may be a key factor in controlling the bed erosion.

4.4.3 Transient ripple effects

As previously presented in Section 4.3.2, transient ripples are ripples that are unstable for their wavelengths and heights when the flow condition changes (*Smith and Sleath*, 2005). Transient ripples have unstable ripple wavelength and ripple height. Therefore, the ripple steepness is also varying over time (Figure 4.4). The ripple steepness is observed to be in the same range for both the 1% and 13% sand experiments, varying from 0.01 to 0.06. However,

the timing of the highest steepness defers between the two; in the 1% experiments, the peak steepness occurs during the reworking stage ($\sim$ 20 min), whereas in the 13% experiments the peak steepness occurs when the ripples have stabilized in the equilibrium stage ($\sim$ 100 min). The transient ripple steepness affects the near-bed turbulence. In Figure 4.7, transient ripple steepness and near-bed shear stress have a linear relationship. Therefore, although there is no obvious trend for ripple steepness over time, the increase of near-bed shear stress, which is presented in Figure 4.2, is highly related to the formation of transient ripples. The increase in transient ripple steepness will increase the near-bed stress, so we hypothesize that the formation of transient ripples might slightly compromise the decrease of bed erodibility since higher instantaneous stress has the potential to erode more sediment.

HHowever, the shape of transient ripples is more complex than what has been shown just in ripple wavelength, ripple height, and ripple steepness, as the transient ripple is not periodic compared to stable ripples (Figure 4.8). For example, a solitary ripple forms in Figure 4.8a and 4.8e. Some tiny transient ripples form in Figure 4.8b and 4.8f, however, those small ripples have comparable ripple steepness compared to the larger ripples. In addition, new ripples form inside old ripples (e.g., Figure 4.8f and 4.8g). *Testik et al.* (2005) studied the adjustment of sand ripples under variable wave conditions and reported three main ripple adjustment processes: ripple splitting, ripple regrowth, and ripple flattening. In our experiments, new ripples form inside old ripples (e.g., Figure 4.8f and 4.8g), which correspond to ripple splitting and ripple regrowth. Sometimes transient ripples also disappeared, which corresponds to Testik's ripple flattening. However, unlike sand ripples reported by *Testik et al.* (2005), our ripple structure is less periodic, and the various shapes imply the potential of a more complex three-dimensional ripple structure inside the flume than the two-dimensional structure measured from the sidewall. As transient ripples affect the near-bed turbulence and bed erosion, we define a new parameter called bed activity (a_b) to quantify how active the bed is. a_b is calculated through image processing and is estimated based on the root mean square of fluctuations of the local bed elevation from the mean bed elevation change at the Vectrino Profiler measured point. Figure 4.4d and 4.4h show the 5-min-average a_b.

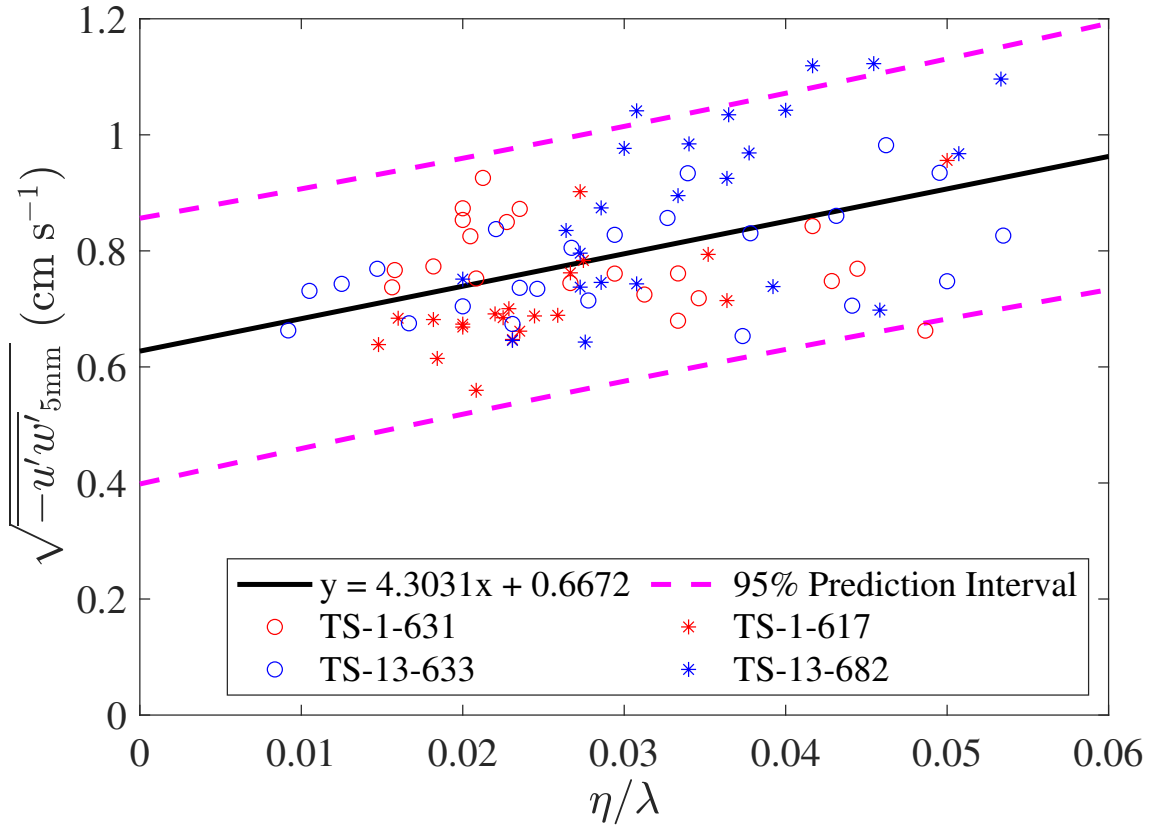

Figure 4.7: Relationship between transient ripple steepness η/λ and the square root of averaged Reynolds stress $\sqrt{-\overline{u'w'}_{5\mathrm{mm}}}$ in the near-bed 5 mm. $R^2 = 0.2354$.

From this figure, we find that a_b is high in the first 20 min for both TS-1-631 and TS-13-633, which reflects the rapid bed change in the bed reworking stage and formation of stable ripples. In the near-constant erosion stage, a_b for 13% sand experiment is higher than 1% sand experiment, which explains that the dimensionless bed erosion rate of TS-13-633 in 40 - 100 min is nearly constant, while the dimensionless bed erosion rate of TS-1-631 in 30 - 90 min slightly decreases. We hypothesize the greater bed activity not only enhances the near-bed turbulence, which increases the potential of sediment suspension but can also rework the bed to reduce the bed armoring effect from the coarser sediment as well since we have observed some transient ripple migration during the experiments.

The total bed adjustment time to achieve the equilibrium for TS-1-631 is around 105 min, while the time for TS-13-633 is around 120 min. *Testik et al.* (2005) studied the adjustment of sand ripples under changing wave intensity and reported the time scale for ripples to reach an equilibrium state can be expressed as

$$\tau = C/\omega\Psi^{1/2} \tag{4.6}$$

where $C = 2500$ is an empirical constant, ω is the radian frequency of the oscillatory flow, $\Psi = U^2/g(s-1)d$, U is the maximum horizontal water velocity, $s = \rho_s/\rho$, ρ and ρ_s are the density of clear water and sediment, g is the gravitational acceleration, and d is the grain size. They mentioned that after $t^* = 3\tau$ the ripple is close to the stable ripples. This expression implies higher sediment grain size leads to longer bed adjustment time before an equilibrium state is reached. However, this expression is mainly for orbital ripples consisting mainly of sand. For fine sediment, it is possible that much smaller ripple steepness of anorbital ripples leads to a shorter ripple deformation time than orbital ripples. Based on our estimation, $C = 6.8 - 22.6$ if we use $t^* = 3\tau$ as the total adjustment time and $d = D_{50}$. *Han et al.* (2021) suggested the importance of the sand fraction in the dynamics of WSGF, and Han et al. (In prep) reported the sand control in sediment suspension, that using D_{sand} is the median grain size of only the sand fraction of sediment to calculate the suspension criterion can predict when the high-concentration layer forms. Here if we use $d = D_{sand}$, we get $C = 6.8 - 22.6$.

Though the estimate of the constant C is different than that found by *Testik et al.* (2005) in sandy ripples, the relationship between ripple adjustment time and the bed grain size can still be used to explain the difference in the bed adjustment time for 1% sand and 13% sand experiments: that higher grain size corresponds to the longer bed adjustment time.

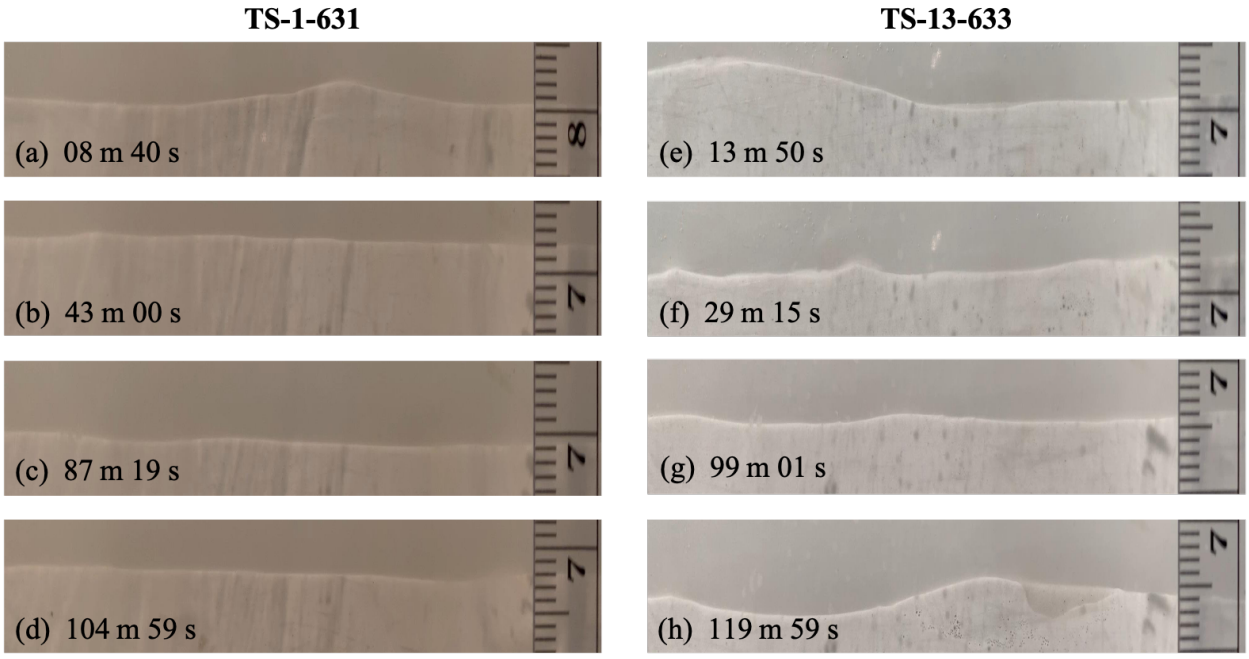

Figure 4.8: Various shapes of transient ripples in different times.

4.4.4 Stratification

Sediment-induced stratification can play an important role in controlling the suspended sediment concentration within the boundary layer when the system is in an equilibrium state (*Hooshmand et al.*, 2015; *Han et al.*, 2021). However, during the present experiments, we find that stratification does not provide a strong control until Stage III. During the total bed adjustment period, the eddy viscosity in the middtle of the boundary layer at $z = 0.5\delta_m$ maintains a relatively constant value of $\nu_e = 1 - 1.2$ m^2 s^{-1} (Figure 4.9a and 4.9d). ν_e at $z = 0.5\delta_m$ slightly decreases after 90 min for TS-1-631 and after 105 min TS-13-633 but not

significantly. *Han et al.* (2021) determined that stratification plays different roles vertically and that strong stratification appears at the top of the wave boundary layer under the equilibrium state. During the adjustment time, Ri_g keeps a relatively low constant value of 0.04 for both 1% sand and 13% sand experiment at $z = 0.5\delta_m$. Ri_g increases from 0.09 to 0.18 after 40 min for TS-1-631, and Ri_g increases from 0.07 to 0.11 after 80 min for TS-13-633 (Figure 4.9d and 4.9e). From Figure 4.9c and 4.9f, a strong stratification zone at the top of the boundary layer gradually forms for both TS-1-631 and TS-13-633, which implies stratification within the wave boundary layer plays a limited role in the near-bed sediment system during the initial bed adjustment process, but eventually plays an important role as the bed becomes stable. Comparing the stratification between 1% sand and 13% sand experiments, stratification plays a relatively more important role in 1% sand experiments, as Ri_g for TS-1-631 at $z = 1.0\delta_m$ is greater than Ri_g for TS-13-633. As discussed in Section 2.3.1, the formation of more significant stable ripples after 105 min for TS-13-633 might account for the reduction of stratification.

4.4.5 Sediment flux budget in the near-bed system

To better understand the roles of the key factors discussed above under the different stages in setting the spatial scale within the wave boundary layer, a simple vertically one-dimension near-bed box model can be used. Based on the equation 4.3, the detailed mass balance inside this box ban be expressed as:

$$\frac{\mathrm{d}}{\mathrm{d}t}\int_{z_0}^{\delta_{CV}} C(z,t)dz = -\rho_s c_b \frac{\mathrm{d}z_b}{\mathrm{d}t} - K_t \frac{\partial C}{\partial z}\bigg|_{z=\delta_{CV}} + w_0 C|_{z=\delta_{CV}} \tag{4.7}$$

Here δ_w is the wave boundary layer thickness, z_0 is the reference height of the bottom. $c(z,t)$ is the concentration at the top of the control volume. $c_b = 1-\phi$ is the bed volumetric concentration, and ϕ is the porosity. z_b is the bed elevation. $K_t = \nu_e/Sc_t$ is the eddy diffusivity, which equals the ratio of eddy viscosity ν_e to the turbulent Schumidt number Sc_t, which for simplicity is set as one. In this equation, $\frac{\mathrm{d}}{\mathrm{d}t}\int_{z_0}^{\delta_{CV}} C(z,t)dz$ represents the local

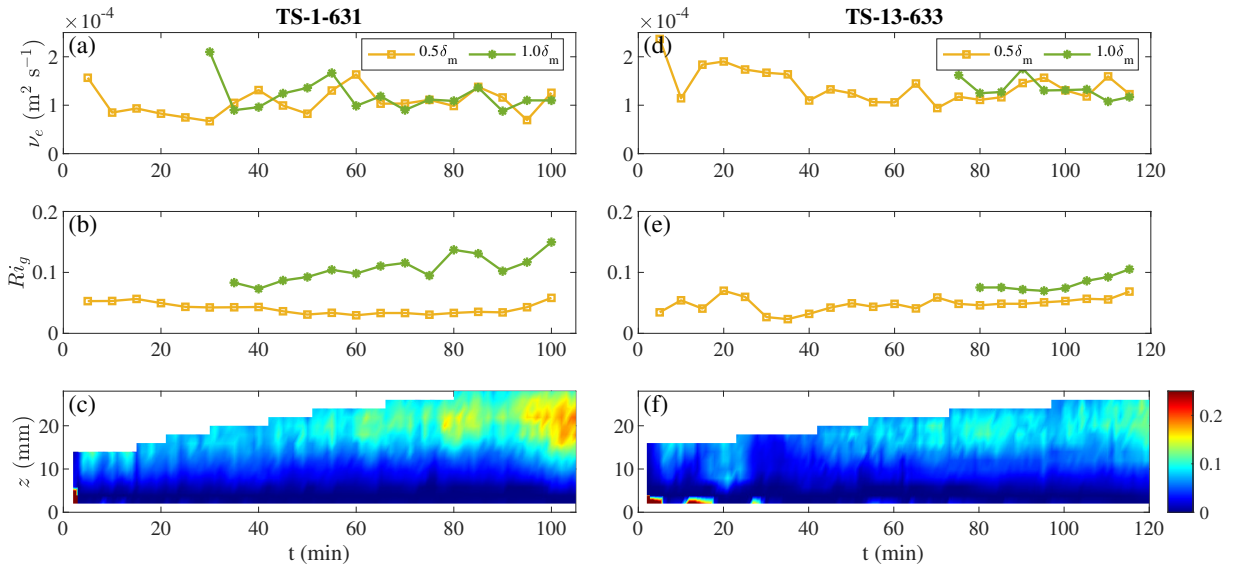

Figure 4.9: Variation of (a, d) five-minute-average eddy viscosity ν_e, (b, e) five-minute-average gradient Richardson number Ri_g at $z = 0.5\delta_m$ and $z = 1.0\delta_m$, where δ_m is the maximum wave boundary layer thickness, and (c, f) one-minute-average pseudocolor plot of near-bed Ri_g.

collection of sediment inside the control volume, $-\rho_s c_b \frac{\mathrm{d}z_b}{\mathrm{d}t}$ represents the input from the bed erosion, $K_t \frac{\partial C}{\partial z}\big|_{z=\delta_{CV}}$ represents the upward transport term out of the control volume, and $w_0 C|_{z=\delta_{CV}}$ represents the settling term into the control volume.

Figure 4.10 shows the comparison of each flux term in the equation 4.7 when setting the top of control volume at $CV = 0.5\delta_m$ and at $CV = 1.0\delta_m$. Here δ_m is the maximum wave boundary layer thickness. For $CV = 0.5\delta_m$ of the case TS-1-631, when $t < 80$ min (Stage I & II), the bed erosion flux $-\rho_s c_b \frac{\mathrm{d}z_b}{\mathrm{d}t}$ is almost balanced with upward transport flux $K_t \frac{\partial C}{\partial z}$, while settling flux $w_0 C$ is less important compared to the other two fluxes, which means most of sediment from the bed will be diffused vertically out of this control volume. Figure 4.3 has shown that near-bed concentration will reach a near-equilibrium state rapidly and then continued bed erosion will be balanced by filling more of the boundary layer upward. For $CV = 0.5\delta_m$, the upward transport flux is always greater than the settling flux. After 80 min (Stage III), $-\rho_s c_b \frac{\mathrm{d}z_b}{\mathrm{d}t} < w_0 C$, the net erosion of the bed drops to zero, and the

system is controlled by the upward transport flux and settling flux. The upward transport flux reaches its maximum value in the first 30 min which is in the initial adjustment stage, and then $K_t \frac{\partial C}{\partial z}$ remains a near-constant value of 0.004 kg m^{-2} s^{-1}. For the case TS-13-633, likewise, three flux terms are well balanced and most of the sediment eroded from the bed will be transported outside the control volume after 5 min. When we set $CV = 1.0\delta_m$, upward transport flux is $\sim$ 0.003 kg m^{-2} s^{-1} during 35 - 55 min (Figure 4.10b), which is much less than the net bed erosion flux. This implies the extra sediment collects inside the wave boundary layer. After 60 min, stratification gradually becomes important, as shown in Figure 4.9c, and $K_t \frac{\partial C}{\partial z} \approx w_0 C$. For the case TS-13-633, as the wave boundary layer thickness is greater than the case TS-1-631, we only get data after 80 min, due to the measurement setting of the Vectrino Profiler. Similarly, $K_t \frac{\partial C}{\partial z} \approx w_0 C$ as stratification increases.

In our estimation, the term $\frac{\mathrm{d}}{\mathrm{d}t} \int_{z_0}^{\delta_{CV}} C(z,t)dz$ is always a order of magnitude smaller than the rest of the terms. One possible reason is how we define the bed $z = 0$. We tried to make the concentration measurement as near the bed as possible. However, there is still a very high concentration near-bed zone that might exceed 200 g L^{-1}, which may trigger the underestimation of $\frac{\mathrm{d}}{\mathrm{d}t} \int_{z_0}^{\delta_{CV}} C(z,t)dz$. The second possible reason is that we did not include the bedload transport flux term. In Exner's equation, bedload transport is taken as a flux term (*Exner*, 1920, 1925). However, for our fine-grained sediment experiments, this term should be minimal compared to other terms. The most probable reason is that we set the mass balance only in one-dimension, considering only the vertical balance. However, extra sediment flux that is unbalanced in Figure 4.10b might be the net horizontal flux that is transported into the end tank and then transported back to the upper water column due to the asymmetry of the oscillatory motion, which is a limitation of our tunnel design. Based on our estimate, the net horizontal flux is $0 - 0.002$ kg m^{-2} s^{-1} , which is in a similar order of magnitude as the imbalance of sediment continuity terms.

The sediment flux budget suggests that the erosion from the bed, the upward transport due to turbulence, and sediment settling controls the suspended sediment concentration simultaneously as the bed erosion continues with time. The upward transport flux does not

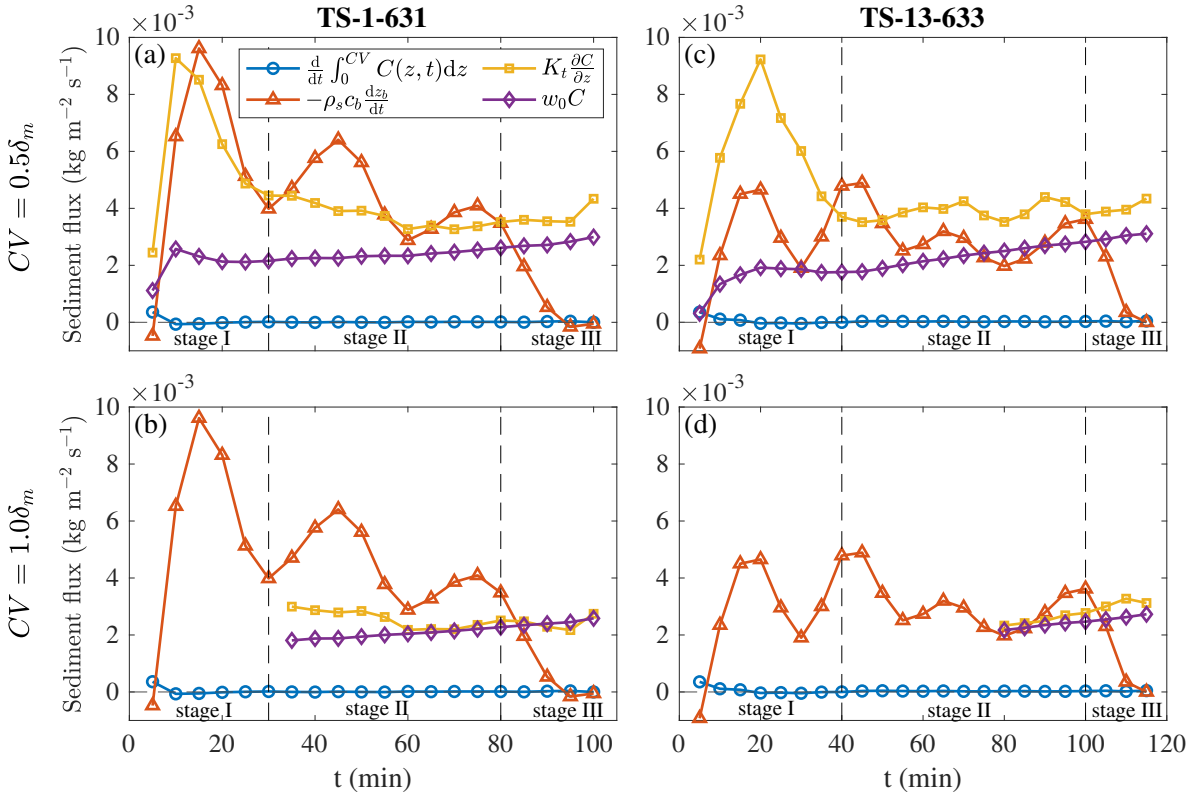

Figure 4.10: Flux budgets of sediment with control volume (a, c) $CV = 0.5\delta_m$ and (b, d) $CV = 1.0\delta_m$. The dashed lines represent the classification of three different stages.

decrease significantly over time after the initial adjustment stage, which means stratification does not increase significantly over time. This implies stratification plays a limited role under the total bed adjustment period. The decrease of the net bed erosion term is a result from the combination of the increase of sediment settling and the decrease of bed erodibility, however it is hard to quantify which factor is more important. When the near-bed system reaches an equilibrium state, the upward transport flux and the settling flux are balanced at the top of the boundary layer.

As mentioned in Section 4.3.1, three different stages can be classified based on the net bed erosion rate. Stage I, the initial adjustment stage, appeared in the first 30 - 40 min after the run started. The non-uniformity of the bed induces rapid sediment redistribution of the bed so that the bed elevation might increase or decrease, and transient ripples start to form. Bed activity is high, which elevates the turbulence so that the upward transport flux is also elevated. Ri_g at the top of the boundary layer is low so that stratification does not reduce the upward transport. In Stage II, the decreasing erosion stage, the net bed erosion rate slightly decreasing over time. Transient ripples are also observed, where the ripple wavelength and ripple height vary over time. However, bed activity is lower than Stage I, and upward transport flux slightly decreases. Ri_g slightly increases over time, which suggests that stratification starts to matter. In Stage III, the near-equilibrium stage, the bed elevation is near-constant, Ri_g at the top of the boundary layer is close to Ri_{cr} (*Han et al.*, 2021), stratification at the top of the boundary layer is strong where the upward transport flux is balanced with the settling flux.

For the fine-grained sediment-laden wave boundary layer in a sand-mud mixed system, the total bed adjustment period is controlled by the combination of different mechanisms discussed in Section 4.4.1. The contributions of these controlling processes vary in time; overall, stratification increases as the near-bed concentration increases, and erodibility decreases as fine sediments are winnowed from the bed surface. During Stage I bed erosion and boundary layer sediment concentration increase rapidly, and neither erodibility nor stratification control the erosion rate. During Stage II, the erosion rate decreases, and we suggest

that erodibility decreases as the collections of sand particles on the bed surface leads to the armoring of the bed from erosion. Finally, in Stage III, stratification at the top of the boundary layer increases, limiting the flux of sediment into the overlying fluid and net erosion stops. This equilibrium state is likely limited by the influence of both bed erodibility and stratification. These processes, which control the formation of a high concentration layer, are also likely to be important in the initiation of a WSGF event.

4.5 Conclusions

We performed four sets of time-series laboratory experiments using two different bed sediment mixtures: 1% sand and 13% sand fraction to investigate the temporal development of near-bed sediment suspension under oscillatory flow. Several conclusions can be made here.

The total bed adjustment before equilibrium can be divided into three stages: in the first 30 - 40 min, the non-uniform of the bed introduces sediment redistribution and transient ripples start to form, where bed elevation might increase or decrease; during 30 - 90 min for 1% sand experiments or 40 - 105 min for 13% sand experiments, the bed erosion rate is near a constant value, stratification at the top of the boundary layer becomes important; in the final 15 min, the bed erosion rate drops to near zero, upward transport flux is balanced with the settling flux, and the system reaches an equilibrium state.

Different controlling mechanisms are presented that control the bed erosion (E) and deposition (D). In the absence of stratification and variation of bed erodibility, the increase of the sediment settling due to the increase of sediment concentration balances the erosion which leads to the equilibrium. (1) Bed control: the decrease of bed erodibility decrease E which limits the bed from further erosion and finally $D = E$ with both the decrease of E and the increase of D; (2) Stratification control: stratification at the top of the wave boundary layer prevents the sediment transport of out of the wave boundary layer, which leads to the faster increase of D than pure settling and reduced the total amount of erosion of the bed.

Bed conditions, including bed erodibility and bedforms, affect bed erosion. Bed erodibility limits the bed from further erosion. Bed armoring due to the surface coarsening of the bed is

observed, and decreases the bed erodibility. Transient ripples form during the bed adjustment period before the equilibrium state, where the wavelength and height of transient ripples are unstable. However, the steepness of transient ripples is highly related to the near-bed shear stress. High ripple steepness elevates the near-bed shear stress and reworks the bed, potentially reducing surface bed coarsening. Therefore, the formation of transient ripples might slightly increase bed erosion.

Stratification plays a limited role in the near-bed sediment system during the bed adjustment period. Stratification starts to matter after the initial bed adjustment period, when the gradient Richardson number Ri_g at the top of the boundary layer increases and limits the sediment from further transport out of the boundary layer.

The different initial sand-mud mixtures of the bed affects the total bed adjustment time. Greater sand content in the bed grain size distribution increases the total bed adjustment time, where for 1% sand experiment the bed adjustment time is $\sim$ 105 min, and for 13% sand experiment the time is $\sim$ 120 min. The higher sand fraction also increases the transient ripple activity, increases the turbulent diffusion, and thus, reduces the effect of stratification.

Chapter 5

CONCLUSIONS

5.1 Summary

In this dissertation, we investigated the dynamics of Wave-Supported Gravity Flow (WSGF), which is an important mechanism for cross-shore fine sediment transport on the continental shelve. The experiments of temporal adjustments of the bed before the equilibrium state been reached were also investigated using the same two kinds of sediment with different sand-mud mixtures. High-resolution measurements of velocity, turbulence, suspended sediment concentration, bedforms, and bed elevation changes were made in an oscillating water tunnel. There were three principal goals in this program. The first was to investigate the grain size effects, especially sand fraction effects, on the dynamics of WSGF over primarily muddy seabeds. we conducted experiments with a wide range of wave orbital velocity and wave period using both 1% sand fraction and 13% sand fraction siliceous sediment, respectively. These experiments were conducted under equilibrium states. Comparing 1% sand fraction and 13% sand fraction experiment helps us unveil the sand fraction influence of near-bed turbulence, suspended sediment concentration, and role of stratification near the seabed. With the understanding of the first goal which addresses the importance of sand components over primarily muddy seabeds, the second goal was set to investigate how the sand controls sediment suspension. We presented experimental results focusing on the bed response, and propose a modified sediment suspension criterion reflecting the role of sand in mud-dominant environments. The third goal was to investigate the temporal adjustment of the seabed before the equilibrium state was reached. We conducted four sets of bed adjustment experiments from the start of the run to the end of bed erosion, i.e., the equilibrium state. The bed adjustment experiments enable us to tease out how the bed erodibility and the near-bed

stratification change over time when the bed is eroding, what are the dominant factors that affect the sediment suspension, which different erosion stages will the system encounter before the equilibrium state been reached. This dissertation makes several key contributions to our understanding of Wave-Supported Gravity Flows.

Our equilibrium state experimental results show that influence of sand content on the dynamics of wave-supported gravity flows in mud-dominant environments is mainly through the formation of ripples. Low and high energy regimes are differentiated based on a Stokes Reynolds number $Re_\Delta \approx 500$. In the low energy regime, the sand fraction influences flow dynamics primarily through ripple formation; no ripples form in the 1% sand experiments, whereas ripples form in the 13% experiments that increase turbulence and the wave boundary layer thickness, δ_m. In the high energy regime, small ripples form in both the 1% and 13% sand experiments and we observe high near-bed suspended sediment concentrations. The influence of stratification on the boundary layer flow is characterized in terms of the gradient Richardson number Ri_g. The flow is weakly stratified inside the boundary layer for all runs and critically stratified at or above the top of the boundary layer. In the lower energy regime, the sand content reduces the relative influence of stratification in the boundary layer, shifting the elevation of critical stratification, L_B, from approximately $1.3\delta_m$ to $2.5\delta_m$ in the 1% and 13% experiments, respectively. In both sets of experiments $L_B \approx \delta_m$ at the strongest wave energy, indicating a transition to strongly stratified dynamics.

We presented equilibrium state experimental results for sand control in sediment suspension over mud-dominant environments. High near-bed concentration and concentration gradient happen when the sand fractions suspend from the bed. The suspension of sand fraction in bed sediment mixture leads to the formation of a high suspended-sediment concentration layer. A modified sediment suspension criterion is created based on *Van Rijn* (1984) and using the median particle size of only sand fraction in the bed and is successful in predicting the necessary suspension that contributes to wave-supported gravity flow formation. This criterion is verified by two field measurement data sets. This modifies sediment suspension criterion provides a limited condition for the formation of wave-supported gravity

flows.

The temporal adjustment experimental results of the bed are presented. The total bed adjustment before the equilibrium can be divided into three stages. Stage I appears in the first 30 - 40 min, where the non-uniformity of the bed introduces sediment redistribution and transient ripples start to form, and the bed elevation might increase or decrease. Stage II appears during 30 - 90 min for 1% sand experiments or 40 - 105 min for 13% sand experiments, where the bed erosion rate is near a constant value. Stage III appears in the final 15 min, where the bed erosion rate drops to near zero, upward transport flux is balanced with the settling flux, stratification is induced at the top of the wave boundary layer, and the system reaches an equilibrium state. Different controlling mechanisms of the bed erosion and deposition are discussed: bed control, and stratification control. In our experiments, bed armoring due to the surface coarsening of the bed is observed, which decreases the bed erodibility. Transient ripples are observed in the total bed adjustment period, which elevates near-bed shear stress. The formation of transient ripples might slightly increase bed erosion. Stratification plays a limited role in the near-bed sediment system during the bed adjustment period but becomes important when the equilibrium state is reached.

5.2 Open questions

While much was learned from our measurement and analyses presented in this thesis, a number of questions remain unanswered. Many of these questions arose over the course of this Ph.D. work and in response to the findings exposed in previous chapters. Open questions are listed below:

- Is the sand control still available in a muddier (i.e. more cohesive) environment, or sediment cohesion dominates the sediment suspension?

- What are the temporal characteristics for a whole storm event, which introduced a WSGF event?

- When should we add WSGF module into the sediment model? Is there a statistical frequency of occurrence of WSGF events?

- How to quantify which is the dominant scenario (pure settling control, bed control, and stratification control) for the near-bed erosion-deposition system? Is it related to the amount of sand fraction?

- What is the spatial difference of dynamics under difference locations of ripples?

- Is there a way of measuring the detailed suspended sediment concentration inside the wave boundary layer? Can the hypothesis Rouse profile inside the WBL be verified?

5.3 Suggestions for future work

In this dissertation, we used silicious sediment that is crushed silica. While the grain size distribution is consistent with muddy sediments, our mixture is not as cohesive as natural mud. The sediment we used should be considered weakly cohesive silicious mud. We have also attempted to use natural sediment sampled from several different places on the shelf out of the Elwha River mouth. As many biological effects appear in these sediments, such as shells, we have to filter the sediment first and remove the significant shells which might alter the characteristic grain size. We then put sediment in the mixer to create a uniform sediment condition. However, after the processing of shells, sediment is super-highly cohesive when we put those sediment into the water tunnel, that no significant sediment into suspension even under our highest wave orbital velocity. The design of our tank limits the wave orbital velocity to be around 55 cm s^{-1}. Higher forcing will induce the whole tank shaking as well as the choke of the piston. So future work might include a redesign of natural sediments that in a water tunnel with higher wave intensity, and caring concern of process of biological effects of the natural sediment. This also implies the sediment cohesiveness controls the sediment suspension under high-cohesion environments.

Both the equilibrium state and the temporal adjustment experiments were performed under fixed wave intensity for each case. For a WSGF event, the wave intensity will always increase and then decrease, where high WSGF flux happens during the high wave intensity. We have attempted to address those varying wave orbital velocity by trying to increase the wave intensity to a fixed value of every one hour and then decrease to simulate a WSGF event. However, as the settling velocity is so small that a sediment particle usually needs around one to two days to be fully settled, no obvious bed deposition can be measured. A WSGF event usually accompanies by a storm event, which lasts for one to two days, which provides enough sediment settling after the high wave intensity is passed. Future experiments might include a new design of the tank that supports both the continuous increase/decrease of the wave orbital velocity and wave period during the run, as well as a longer run time to fully simulate a WSGF event.

Both stable ripples and transient ripples elevated the near-bed turbulence and affect the sediment suspension from the bed. These ripple effects are taken as a bulk effect through characterizing ripple wavelength, ripple height, and ripple steepness. Some numerical studies have addressed the horizontal dynamical difference in different places of ripples, such as ripple crest and ripple trough. Our experiments have shown that transient ripples change their shapes over time, such as ripple flattening, ripple regrowth, and ripple migration, etc. Future experiments might focus on dynamical differences under different positions of ripples, which will reveal a more detailed structure of WSGF under ripples. Some new model results might be helpful for understanding those processes (e.g. *Salimi-Tarazouj et al.*, 2021).

BIBLIOGRAPHY

Ardhuin, F., T. Drake, and T. Herbers (2002), Observations of wave-generated vortex ripples on the North Carolina continental shelf, *Journal of Geophysical Research: Oceans*, *107*(C10), 7–1.

Bagnold, R. A. (1946), Motion of waves in shallow water. interaction between waves and sand bottoms, *Proceedings of the Royal Society of London. Series A. Mathematical and Physical Sciences*, *187*(1008), 1–18.

Bagnold, R. A. (1954), Experiments on a gravity-free dispersion of large solid spheres in a newtonian fluid under shear, *Proceedings of the Royal Society of London. Series A. Mathematical and Physical Sciences*, *225*(1160), 49–63.

Boreczky, J. S., and L. A. Rowe (1996), Comparison of video shot boundary detection techniques, *Journal of Electronic Imaging*, *5*(2), 122–128.

Celik, I., and W. Rodi (1991), Suspended sediment-transport capacity for open channel flow, *Journal of Hydraulic Engineering*, *117*(2), 191–204.

Chen, S.-N., and C.-J. Chen (2018), An analytical model with a critical Richardson number closure for sediment-stratified open channel flow, *Journal of Geophysical Research: Oceans*, *123*(9), 6922–6944.

Cheng, Z., X. Yu, T.-J. Hsu, C. E. Ozdemir, and S. Balachandar (2015), On the transport modes of fine sediment in the wave boundary layer due to resuspension/deposition: A turbulence-resolving numerical investigation, *Journal of Geophysical Research: Oceans*, *120*(3), 1918–1936.

Egan, G., A. J. Manning, G. Chang, O. Fringer, and S. Monismith (2020), Sediment-induced stratification in an estuarine bottom boundary layer, *Journal of Geophysical Research: Oceans*, *125*(8), e2019JC016,022.

Engelund, F. (1965), A criterion for the occurrence of suspended load, *La Houille Blanche*, *8*(7).

Engelund, F., and E. Hansen (1967), A monograph on sediment transport in alluvial streams, *Technical University of Denmark 0stervoldgade 10, Copenhagen K.*

Exner, F. (1920), Zur physik der dunen, akad, *Wiss. Wien Math. Naturwiss. Klasse*, *129*(2a), 929–952.

Exner, F. M. (1925), Uber die wechselwirkung zwischen wasser und geschiebe in flussen, *Akad. Wiss. Wien Math. Naturwiss. Klasse*, *134*(2a), 165–204.

Flores, R. P. (2018), The dynamics of cross-shore sediment transport in the Rhine region of freshwater influence, Ph.D. thesis, University of Washington.

Flores, R. P., S. Rijnsburger, S. Meirelles, A. R. Horner-Devine, A. J. Souza, J. D. Pietrzak, M. Henriquez, and A. Reniers (2018), Wave generation of gravity-driven sediment flows on a predominantly sandy seabed, *Geophysical Research Letters*, *45*(15), 7634–7645.

Foster, D. L., R. A. Beach, and R. A. Holman (2000), Field observations of the wave bottom boundary layer, *Journal of Geophysical Research: Oceans*, *105*(C8), 19,631–19,647.

Friedrichs, C., and L. Wright (2004), Gravity-driven sediment transport on the continental shelf: implications for equilibrium profiles near river mouths, *Coastal Engineering*, *51*(8-9), 795–811.

Friedrichs, C., L. Wright, D. Hepworth, and S. Kim (2000), Bottom-boundary-layer processes associated with fine sediment accumulation in coastal seas and bays, *Continental Shelf Research*, *20*(7), 807–841.

Friedrichs, C. T., G. M. Cartwright, and P. J. Dickhudt (2008), Quantifying benthic exchange of fine sediment via continuous, noninvasive measurements of settling velocity and bed erodibility, *Oceanography*, *21*(4), 168–172.

Gao, S., D. Wang, Y. Yang, L. Zhou, Y. Zhao, W. Gao, Z. Han, Q. Yu, and G. Li (2016), Holocene sedimentary systems on a broad continental shelf with abundant river input: process–product relationships, *Geological Society, London, Special Publications*, *429*(1), 223–259.

Goring, D. G., and V. I. Nikora (2002), Despiking acoustic doppler velocimeter data, *Journal of Hydraulic Engineering*, *128*(1), 117–126.

Grabowski, R. C., I. G. Droppo, and G. Wharton (2011), Erodibility of cohesive sediment: The importance of sediment properties, *Earth-Science Reviews*, *105*(3-4), 101–120.

Grant, W. D., and O. S. Madsen (1982), Movable bed roughness in unsteady oscillatory flow, *Journal of Geophysical Research: Oceans*, *87*(C1), 469–481.

Grant, W. D., and O. S. Madsen (1986), The continental-shelf bottom boundary layer, *Annual Review of Fluid Mechanics*, *18*(1), 265–305.

Gregg, M. (1987), Diapycnal mixing in the thermocline: A review, *Journal of Geophysical Research: Oceans*, *92*(C5), 5249–5286.

Gross, T., A. Williams, and E. Terray (1994), Bottom boundary layer spectral dissipation estimates in the presence of wave motions, *Continental Shelf Research*, *14*(10-11), 1239–1256.

Hale, R. P., and A. S. Ogston (2015), In situ observations of wave-supported fluid-mud generation and deposition on an active continental margin, *Journal of Geophysical Research: Earth Surface*, *120*(11), 2357–2373.

Han, Z., A. R. Horner-Devine, A. S. Ogston, and T.-J. Hsu (2021), The role of sand in wave boundary layers over primarily muddy seabeds: Implications for wave-supported gravity flows, *Journal of Geophysical Research: Oceans*, *126*(5), e2020JC016,621.

Hanson, G., and A. Simon (2001), Erodibility of cohesive streambeds in the loess area of the midwestern USA, *Hydrological Processes*, *15*(1), 23–38.

Harris, C. K., and P. Wiberg (2002), Across-shelf sediment transport: Interactions between suspended sediment and bed sediment, *Journal of Geophysical Research: Oceans*, *107*(C1), 8–1.

Harris, C. K., and P. L. Wiberg (2001), A two-dimensional, time-dependent model of suspended sediment transport and bed reworking for continental shelves, *Computers & Geosciences*, *27*(6), 675–690.

Harris, C. K., P. Traykovski, and W. R. Geyer (2004), Including a near-bed turbid layer in a three dimensional sediment transport model with application to the Eel River shelf, northern California, in *Estuarine and Coastal Modeling (2003)*, pp. 784–803.

Harris, C. K., P. A. Traykovski, and W. R. Geyer (2005), Flood dispersal and deposition by near-bed gravitational sediment flows and oceanographic transport: A numerical modeling study of the Eel River shelf, northern California, *Journal of Geophysical Research: Oceans*, *110*(C9).

Harris, C. K., C. R. Sherwood, R. P. Signell, A. J. Bever, and J. C. Warner (2008), Sediment dispersal in the northwestern Adriatic Sea, *Journal of Geophysical Research: Oceans*, *113*(C11).

Hino, M., M. Kashiwayanagi, A. Nakayama, and T. Hara (1983), Experiments on the turbulence statistics and the structure of a reciprocating oscillatory flow, *Journal of Fluid Mechanics*, *131*, 363–400.

Hooshmand, A. (2016), Wave-supported gravity currents in continental shelves, Ph.D. thesis, University of Washington.

Hooshmand, A., A. R. Horner-Devine, and M. P. Lamb (2015), Structure of turbulence and sediment stratification in wave-supported mud layers, *Journal of Geophysical Research: Oceans*, *120*(4), 2430–2448.

Hsu, T.-J., P. A. Traykovski, and G. C. Kineke (2007), On modeling boundary layer and gravity-driven fluid mud transport, *Journal of Geophysical Research: Oceans*, *112*(C4).

Hsu, T.-J., C. E. Ozdemir, and P. A. Traykovski (2009), High-resolution numerical modeling of wave-supported gravity-driven mudflows, *Journal of Geophysical Research: Oceans*, *114*(C5).

Hurther, D., and U. Lemmin (2001), A correction method for turbulence measurements with a 3d acoustic doppler velocity profiler, *Journal of Atmospheric and Oceanic Technology*, *18*(3), 446–458.

Kineke, G., and R. Sternberg (1995), Distribution of fluid muds on the Amazon continental shelf, *Marine Geology*, *125*(3-4), 193–233.

Kineke, G., R. Sternberg, J. Trowbridge, and W. Geyer (1996), Fluid-mud processes on the Amazon continental shelf, *Continental Shelf Research*, *16*(5-6), 667–696.

Kineke, G., E. Higgins, K. Hart, and D. Velasco (2006), Fine-sediment transport associated with cold-front passages on the shallow shelf, Gulf of Mexico, *Continental Shelf Research*, *26*(17-18), 2073–2091.

Konert, M., and J. Vandenberghe (1997), Comparison of laser grain size analysis with pipette and sieve analysis: a solution for the underestimation of the clay fraction, *Sedimentology*, *44*(3), 523–535.

Kundu, P. K., I. M. Cohen, and D. Dowling (2015), Fluid mechanics 6th edition.

Lamb, M. P., and J. D. Parsons (2005), High-density suspensions formed under waves, *Journal of Sedimentary Research*, *75*(3), 386–397.

Lamb, M. P., E. D'Asaro, and J. D. Parsons (2004), Turbulent structure of high-density suspensions formed under waves, *Journal of Geophysical Research: Oceans*, *109*(C12), n/a–n/a.

Liang, H., M. P. Lamb, and J. D. Parsons (2007), Formation of a sandy near-bed transport layer from a fine-grained bed under oscillatory flow, *Journal of Geophysical Research: Oceans*, *112*(C2).

Lumley, J., and E. Terray (1983), Kinematics of turbulence convected by a random wave field, *Journal of Physical Oceanography*, *13*(11), 2000–2007.

Ma, Y., L. D. Wright, and C. T. Friedrichs (2008), Observations of sediment transport on the continental shelf off the mouth of the Waiapu River, New Zealand: evidence for current-supported gravity flows, *Continental Shelf Research*, *28*(4-5), 516–532.

MacDonald, D. G., and F. Chen (2012), Enhancement of turbulence through lateral spreading in a stratified-shear flow: Development and assessment of a conceptual model, *Journal of Geophysical Research: Oceans*, *117*(C5).

Mahoney, J. B. (2005), Nd and Sr isotopic signatures of fine-grained clastic sediments: A case study of western Pacific marginal basins, *Sedimentary Geology*, *182*(1-4), 183–199.

Mehta, A. (1988), Laboratory studies on cohesive sediment deposition and erosion, in *Physical processes in estuaries*, pp. 427–445, Springer.

Mehta, A. J. (1989), On estuarine cohesive sediment suspension behavior, *Journal of Geophysical Research: Oceans*, *94*(C10), 14,303–14,314.

Mori, N., T. Suzuki, and S. Kakuno (2007), Noise of acoustic doppler velocimeter data in bubbly flows, *Journal of Engineering Mechanics*, *133*(1), 122–125.

Moriarty, J. M., C. K. Harris, and M. G. Hadfield (2015), Event-to-seasonal sediment dispersal on the Waipaoa River shelf, New Zealand: A numerical modeling study, *Continental Shelf Research*, *110*, 108–123.

Nelson, T. R., G. Voulgaris, and P. Traykovski (2013), Predicting wave-induced ripple equilibrium geometry, *Journal of Geophysical Research: Oceans*, *118*(6), 3202–3220.

Nielsen, P. (1981), Dynamics and geometry of wave-generated ripples, *Journal of Geophysical Research: Oceans*, *86*(C7), 6467–6472.

Nikuradse, J. (1933), Stromungsgesetze in rauhen rohren, *VDI-Forschungsheft*, *361*, 1.

Nittrouer, C. A., and L. D. Wright (1994), Transport of particles across continental shelves, *Reviews of Geophysics*, *32*(1), 85–113.

Ogston, A., D. Cacchione, R. Sternberg, and G. Kineke (2000), Observations of storm and river flood-driven sediment transport on the northern California continental shelf, *Continental Shelf Research*, *20*(16), 2141 – 2162.

Ozdemir, C. E., T.-j. Hsu, and S. Balachander (2010), A numerical investigation of fine particle laden flow in an oscillatory channel: the role of particle-induced density stratification, *Journal of Fluid Mechanics*, *665*, 1–45.

Ozdemir, C. E., T.-J. Hsu, and S. Balachandar (2014), Direct numerical simulations of transition and turbulence in smooth-walled Stokes boundary layer, *Physics of Fluids*, *26*(4), 045,108.

Parker, G., Y. Fukushima, and H. M. Pantin (1986), Self-accelerating turbidity currents, *Journal of Fluid Mechanics*, *171*, 145–181.

Partheniades, E. (1988), Engineering properties and hydraulic behavior of cohesive sediments, *Coastal Engineering*, *12*, 157–174.

Pedocchi, F., and M. H. García (2009a), Friction coefficient for oscillatory flow: the rough–smooth turbulent transition, *Journal of hydraulic research*, *47*(4), 438–444.

Pedocchi, F., and M. H. García (2009b), Ripple morphology under oscillatory flow: 1. prediction, *Journal of Geophysical Research: Oceans*, *114*(C12).

Puig, P., A. Ogston, B. Mullenbach, C. Nittrouer, and R. Sternberg (2003), Shelf-to-canyon sediment-transport processes on the Eel continental margin (northern California), *Marine Geology*, *193*(1-2), 129–149.

Roberts, J., R. Jepsen, D. Gotthard, and W. Lick (1998), Effects of particle size and bulk density on erosion of quartz particles, *Journal of Hydraulic Engineering*, *124*(12), 1261–1267.

Rouse, H. (1937), Modern conceptions of the mechanics of fluid turbulence, *Transactions of the American Society of Civil Engineers*, *102*(1), 463–505.

Salimi-Tarazouj, A., T.-J. Hsu, P. Traykovski, Z. Cheng, and J. Chauchat (2021), A numerical study of onshore ripple migration using a Eulerian two-phase model, *Journal of Geophysical Research: Oceans*, *126*(2), e2020JC016,773.

Sanford, L. P. (2008), Modeling a dynamically varying mixed sediment bed with erosion, deposition, bioturbation, consolidation, and armoring, *Computers & Geosciences*, *34*(10), 1263–1283.

Sanford, L. P., and J. P.-Y. Maa (2001), A unified erosion formulation for fine sediments, *Marine Geology*, *179*(1-2), 9–23.

Schlichting, H., and K. Gersten (2016), *Boundary-layer theory*, Springer.

Scully, M., C. Friedrichs, and L. Wright (2002), Application of an analytical model of critically stratified gravity-driven sediment transport and deposition to observations from the

Eel River continental shelf, Northern California, *Continental Shelf Research*, *22*(14), 1951 – 1974.

Smith, D., and J. F. Sleath (2005), Transient ripples in oscillatory flows, *Continental Shelf Research*, *25*(4), 485–501.

Smyth, C., A. E. Hay, and L. Zedel (2002), Coherent doppler profiler measurements of near-bed suspended sediment fluxes and the influence of bed forms, *Journal of Geophysical Research: Oceans*, *107*(C8), 19–1.

Son, M., and T.-J. Hsu (2011), The effects of flocculation and bed erodibility on modeling cohesive sediment resuspension, *Journal of Geophysical Research: Oceans*, *116*(C3).

Sternberg, R., D. Cacchione, B. Paulso, G. Kineke, and D. Drakez (1996), Observations of sediment transport on the Amazon subaqueous delta, *Continental Shelf Research*, *16*(5-6), 697–715.

Sumer, B. (1986), Recent developments on the mechanics of sediment suspension, *Proc., Euromech 192: Transport of Suspended Solids in Open Channels*, pp. 3–13.

Swart, D. H. (1974), Offshore sediment transport and equilibrium beach profiles.

Tennekes, H., and J. L. Lumley (1972), *A first course in turbulence*, MIT Press.

Testik, F., S. Voropayev, and H. Fernando (2005), Adjustment of sand ripples under changing water waves, *Physics of Fluids*, *17*(7), 072,104.

Thorpe, S. A. (2005), *The turbulent ocean*, Cambridge University Press.

Traykovski, P., W. Geyer, J. Irish, and J. Lynch (2000), The role of wave-induced density-driven fluid mud flows for cross-shelf transport on the Eel River continental shelf, *Continental Shelf Research*, *20*(16), 2113 – 2140.

Traykovski, P., P. Wiberg, and W. Geyer (2007), Observations and modeling of wave-supported sediment gravity flows on the po prodelta and comparison to prior observations from the Eel shelf, *Continental Shelf Research*, *27*(3), 375 – 399.

Traykovski, P., J. Trowbridge, and G. Kineke (2015), Mechanisms of surface wave energy dissipation over a high-concentration sediment suspension, *Journal of Geophysical Research: Oceans*, *120*(3), 1638–1681.

Trowbridge, J. H., and G. C. Kineke (1994), Structure and dynamics of fluid muds on the Amazon Continental Shelf, *Journal of Geophysical Research: Oceans*, *99*(C1), 865–874.

Troy, C. D., and J. R. Koseff (2005), The instability and breaking of long internal waves, *Journal of Fluid Mechanics*, *543*, 107–136.

Van Rijn, L. C. (1984), Sediment transport, part ii: suspended load transport, *Journal of hydraulic engineering*, *110*(11), 1613–1641.

Walsh, J., and C. Nittrouer (2009), Understanding fine-grained river-sediment dispersal on continental margins, *Marine Geology*, *263*(1-4), 34–45.

Wentworth, C. K. (1922), A scale of grade and class terms for clastic sediments, *The Journal of Geology*, *30*(5), 377–392.

Wiberg, P., and C. K. Harris (1994), Ripple geometry in wave-dominated environments, *Journal of Geophysical Research: Oceans*, *99*(C1), 775–789.

Wiberg, P., and J. D. Smith (1983), A comparison of field data and theoretical models for wave-current interactions at the bed on the continental shelf, *Continental Shelf Research*, *2*(2-3), 147–162.

Wiberg, P. L., D. E. Drake, and D. A. Cacchione (1994), Sediment resuspension and bed armoring during high bottom stress events on the northern california inner continental shelf: measurements and predictions, *Continental Shelf Research*, *14*(10-11), 1191–1219.

Winterwerp, J. (2006), Stratification effects by fine suspended sediment at low, medium, and very high concentrations, *Journal of Geophysical Research: Oceans*, *111*(C5).

Wright, L., and C. Friedrichs (2006), Gravity-driven sediment transport on continental shelves: a status report, *Continental Shelf Research*, *26*(17-18), 2092–2107.

Wright, L., and C. Nittrouer (1995), Dispersal of river sediments in coastal seas: six contrasting cases, *Estuaries*, *18*(3), 494–508.

Wright, L., W. Wiseman Jr, Z.-S. Yang, B. Bornhold, G. Keller, D. B. Prior, and J. Suhayda (1990), Processes of marine dispersal and deposition of suspended silts off the modern mouth of the Huanghe (Yellow River), *Continental Shelf Research*, *10*(1), 1–40.

Wright, L., C. Friedrichs, S. Kim, and M. Scully (2001), Effects of ambient currents and waves on gravity-driven sediment transport on continental shelves, *Marine Geology*, *175*(1), 25–45.

Yue, L., Z. Cheng, and T.-J. Hsu (2020), A turbulence-resolving numerical investigation of wave-supported gravity flows, *Journal of Geophysical Research: Oceans*, *125*(2), e2019JC015,220.

Zang, Z., Z. G. Xue, K. Xu, C. E. Ozdemir, Q. Chen, S. J. Bentley, and C. Sahin (2020), A numerical investigation of wave-supported gravity flow during cold fronts over the Atchafalaya shelf, *Journal of Geophysical Research: Oceans*, *125*(9), e2019JC015,269.

Appendix A

INSTABILITY TIME SCALES

The role of stratification in WSGFs has often been understood in terms of a critical value of the gradient Richardson number (Ri_{gc}). This interpretation borrows from other studies of stratified turbulence (*Kundu et al.*, 2015), in which the critical value of Ri_g is considered to be a necessary condition for the development of shear instability and the transition to turbulence. In a periodically shear flow such as a wave boundary layer, as opposed to a steady shear flow, it is necessary to ensure that instabilities at the density interface have enough time to grow. This appendix evaluates whether this condition is met in order to ensure that the imposed wave timescales do not invalidate the interpretation based on Ri_g.

A commonly discussed instability in the ocean is the shear-induced Kelvin-Helmholtz (KH) instability. Theoretically, the instability growth rate can be solved using the Tayler-Goldstein (TG) Equation and for unidirectional flow, the TG equation can be solved analytically. Currently, there are limited studies on instabilities in sediment stratified flows, but two recent studies provide some clues for the onset of instabilities under a wave or just oscillatory conditions (*Ozdemir et al.*, 2010; *Traykovski et al.*, 2015). *Ozdemir et al.* (2010) used an Eulerian-Eulerian two-phase flow model and found that coherent KH billows formed in high Re_Δ and high near-bed concentration conditions. *Traykovski et al.* (2015) observed internal wave motions near the lutocline on the Louisiana shelf. For our experiments, to fulfill the condition of full growth of the instability, the temporal scale of the flow oscillation (wave period) should be long compared to this instability evolution time scale. For this analysis, we assume that the predominant instabilities are KH instabilities and that the sediment settling timescale is not important. The latter assumption is appropriate for the fine-grained sediment used in our experiments since the settling time scale is long compared

with the wave timescale.

Researchers estimate the KH instability evolution time scale T_{KH} base on either the Brunt-Väisälä buoyancy frequency (N) or the shear ($\partial U/\partial z$) at the interface. *Gregg* (1987) suggests that the onset of KH billows and turbulent diffusion occurs when $T_{\mathrm{KH}} \cdot N \geq 0.1$. The evolution timescale has been estimated in terms of the shear in separate studies as $T_{\mathrm{KH}} \geq 140\partial U/\partial z$ (*MacDonald and Chen*, 2012) and $80\partial U/\partial z \leq T_{\mathrm{KH}} \leq 250\partial U/\partial z$ (*Thorpe*, 2005). The lower limit represents the disappearance of visually coherent billows and the upper limit represents the full collapse of turbulence. For unidirectional flow, the visually coherent billows do not necessarily suggest full turbulence formation from the instability. Bur for progressive monochromatic internal waves, billows always appear at the crest or trough of the internal waves, and the inner parts of the billows are often well-mixed and turbulent (*Troy and Koseff*, 2005).

In Figure A.1 we compare both timescales with the wave periods in our experiments. When using N as the non-dimensional parameter, $T \cdot N > 1$ for the highest Re_{Δ}, but it exceeds the 0.1 threshold from *Gregg* (1987) in all of our experiments (Figure A.1). Similarly, while the wave period is similar to the shear timescales discussed in *MacDonald and Chen* (2012), it is longer than the lower limit of $80\partial U/\partial z$ cited by *Thorpe* (2005). Thus the wave periods in our experiments are similar to or longer than estimates of the instability evolution time, suggesting that instabilities have time to grow and develop into the turbulent flow within a wave period and that this possible constraint on the use of Ri_g.

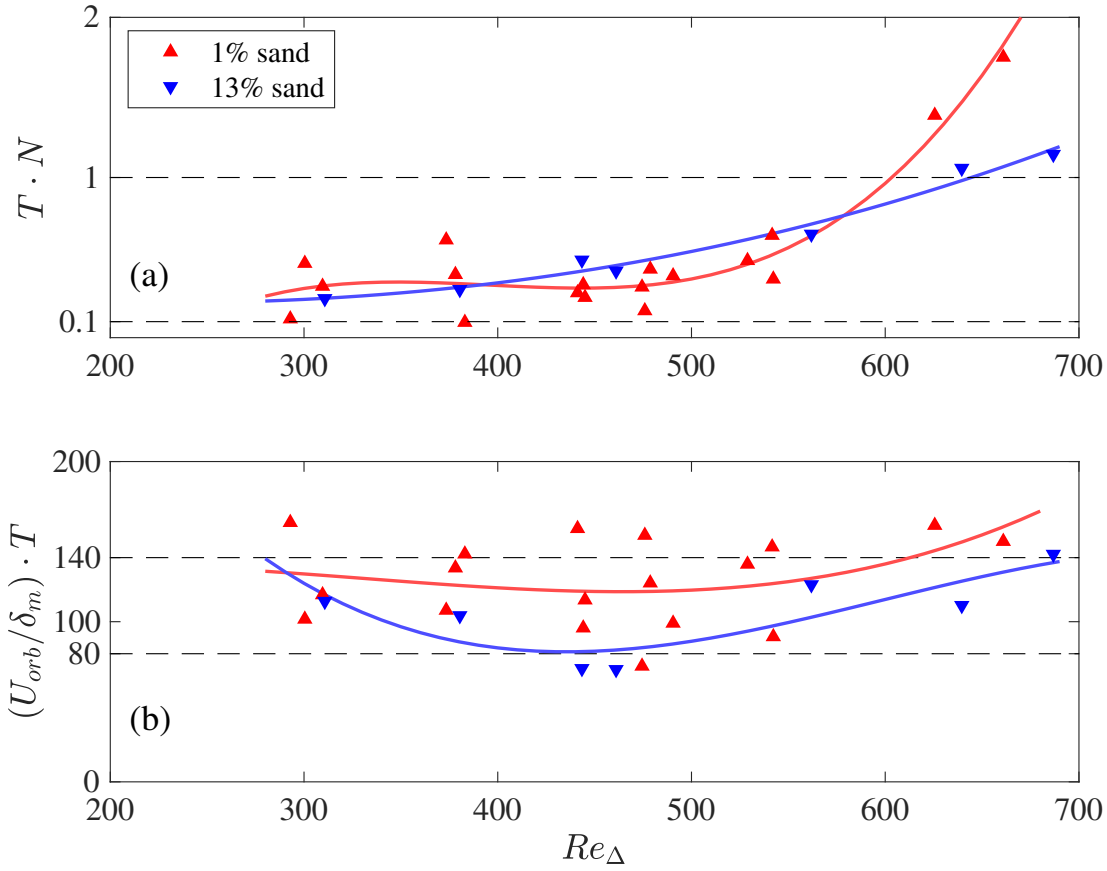

Figure A.1: (a) Variations of the product of wave period and Brunt-Väisälä frequency, (b) the product of wave period and characteristic shear inside the wave boundary layer. In (a) the dash line of $T \cdot N = 0.1$ represents the onset of KH billows and turbulence diffusion scales from *Gregg* (1987). In (b) the dash line of $(U_{orb}/\delta_m) \cdot T = 140$ represents the non-dimensional timescale of KH evolution using shear to non-dimensionalize the time scale from *MacDonald and Chen* (2012); the dash line of $(U_{orb}/\delta_m) \cdot T = 80$ represents the lower bound of the non-dimensional timescale of KH evolution from *Thorpe* (2005).

Appendix B

MODIFIED SUSPENSION CRITERION UNDER EROSIONAL AND DEPOSITIONAL PERIODS

Unlike the flume data, the field data is often more scattering, as the flow condition is more complex. For the field data we used, the data from *Hale and Ogston* (2015) is especially scattering. In addition, sediment suspension is totally different in erosion and deposition periods, separately (Figure B.1). During erosional periods, the modified sediment suspension criterion predicts the occurrence of a high-concentration layer. During deposition periods, however, the data do not satisfy this criterion; many high suspension events occur when $E^* < 1$. This is presumably due to the advection by multiple shelf processes. During depositional periods, low shear velocity cannot suspend a huge amount of sediment, but the bed elevation is still increasing. Therefore, the sediment in suspension is mainly transported from the ambient areas to the measured location. Figure B.1 also shows the data scattering of *Hale and Ogston* (2015), since there are a lot of points with high E^* but low sediment suspension, which does not appear in our flume experiments. The WSGF event is usually characterized during slack tide periods, since the near-bed cross-shelf velocity is mainly due to the gravitational velocity (e.g. *Flores et al.*, 2018).

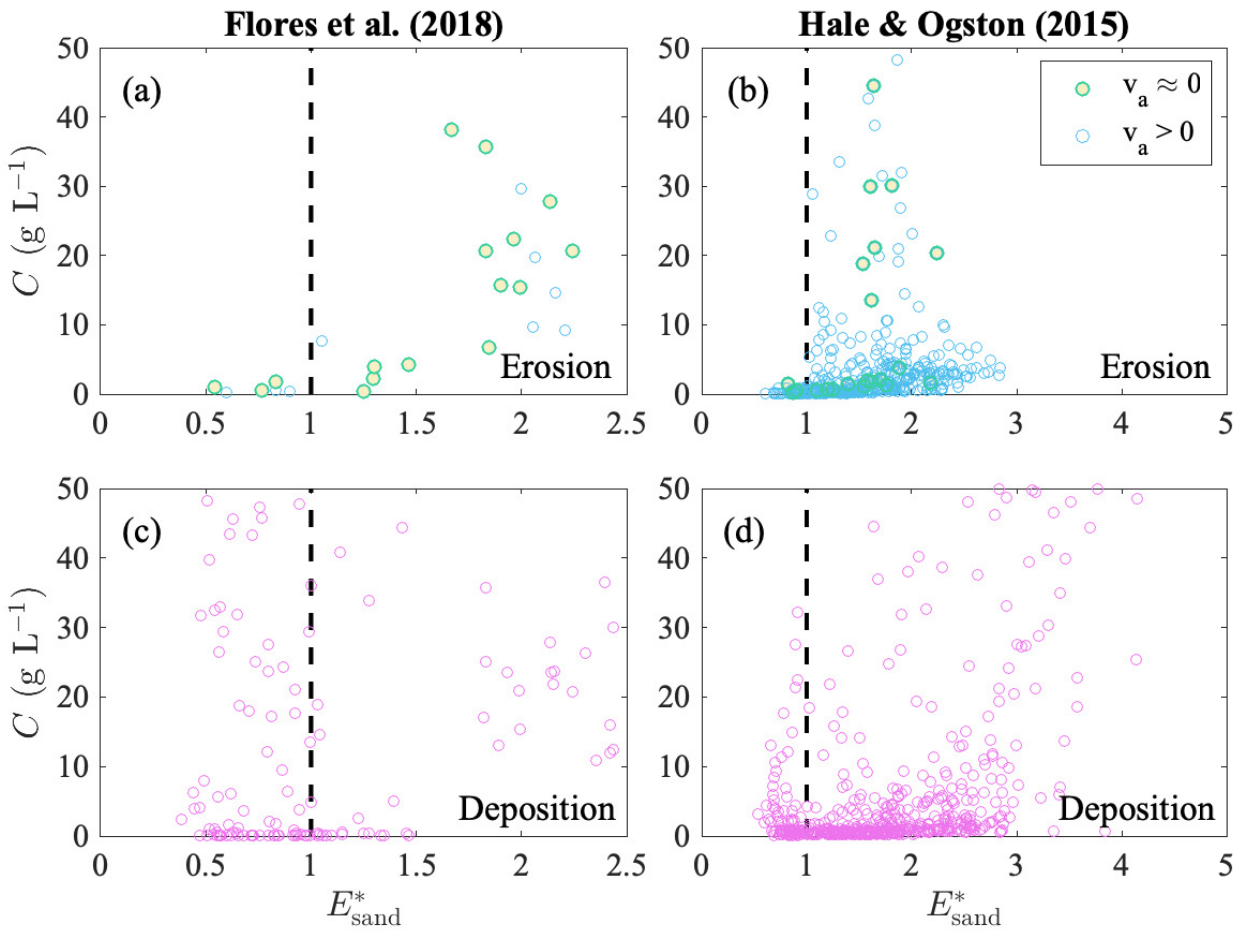

Figure B.1: Sediment suspension criterion during erosion and deposition periods. (a) and (c) are erosion and deposition periods from *Flores et al.* (2018); (b) and (d) are erosion and deposition periods from *Hale and Ogston* (2015). The dashed line represents the modified sediment suspension criterion $E^* = 1$. In (a) and (b), $v_a \approx 0$ represents the data during the ambient velocity is near zero (slack), which is used in Figure 3.6; $v_a > 0$ represents the data during the ambient velocity is significant.